

UNIVERSIDADE FEDERAL DE JUIZ DE FORA
INSTITUTO DE CIÊNCIAS EXATAS / FACULDADE DE ENGENHARIA
PROGRAMA DE PÓS-GRADUAÇÃO EM MODELAGEM
COMPUTACIONAL

Joventino de Oliveira Campos

Impact of uncertainties in cardiac mechanics simulations

Juiz de Fora

2019

Joentino de Oliveira Campos

Impact of uncertainties in cardiac mechanics simulations

Tese apresentada ao Programa de Pós-graduação em Modelagem Computacional, da Universidade Federal de Juiz de Fora como requisito parcial à obtenção do grau de Doutor em Modelagem Computacional.

Orientador: Prof. D.Sc. Bernardo Martins Rocha

Coorientador: Prof. D.Sc. Rodrigo Weber dos Santos

Coorientador: Prof. Ph.D Joakim Sundnes

Juiz de Fora

2019

Ficha catalográfica elaborada através do programa de geração automática da Biblioteca Universitária da UFJF, com os dados fornecidos pelo(a) autor(a)

Campos, Joventino de Oliveira.

Impact of uncertainties in cardiac mechanics simulations / Joventino de Oliveira Campos. -- 2019.
143 p. : il.

Orientador: Bernardo Martins Rocha

Coorientadores: Rodrigo Weber dos Santos, Joakim Sundnes
Tese (doutorado) - Universidade Federal de Juiz de Fora, ICE/Engenharia. Programa de Pós-Graduação em Modelagem Computacional, 2019.

1. Cardiac mechanics. 2. Uncertainty quantification. 3. Augmented lagrangian formulation. 4. Preconditioners. I. Rocha, Bernardo Martins, orient. II. dos Santos, Rodrigo Weber, coorient. III. Sundnes, Joakim, coorient. IV. Título.

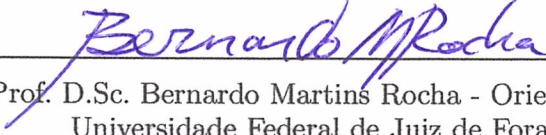
Joventino de Oliveira Campos

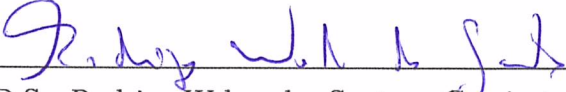
Impact of uncertainties in cardiac mechanics simulations

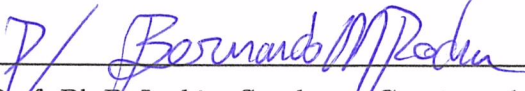
Tese apresentada ao Programa de Pós-graduação em Modelagem Computacional, da Universidade Federal de Juiz de Fora como requisito parcial à obtenção do grau de Doutor em Modelagem Computacional.

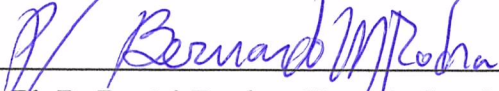
Aprovada em 25 de novembro de 2019.

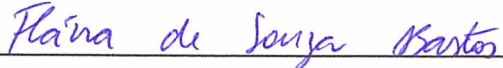
BANCA EXAMINADORA

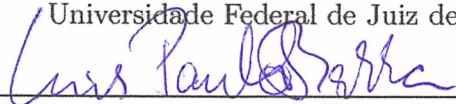

Prof. D.Sc. Bernardo Martins Rocha - Orientador
Universidade Federal de Juiz de Fora

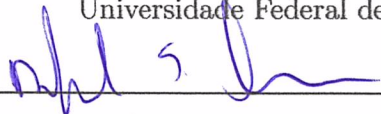

Prof. D.Sc. Rodrigo Weber dos Santos - Coorientador
Universidade Federal de Juiz de Fora


Prof. Ph.D Joakim Sundnes - Coorientador
Simula School of Research and Innovation


Prof. Ph.D. Daniel Esteban Hurtado Sepúlveda
Pontificia Universidad Católica de Chile


Prof^ª. D.Sc. Flávia de Souza Bastos
Universidade Federal de Juiz de Fora


Prof. D.Sc. Luis Paulo da Silva Barra
Universidade Federal de Juiz de Fora


Prof^ª. D.Sc. Rafael Sachetto Oliveira
Universidade Federal de São João del-Rei

ACKNOWLEDGMENTS

First of all, I would like to thank God that provides me the life and forces to keep working every day to achieve my dreams. I would like to thank my family and especially my fiancée for all support during the last years. Thank you to my friends, lab coworkers and to the Computational Modeling Graduate program from the Universidade Federal de Juiz de Fora. Thank you to my supervisors Bernardo, Rodrigo, and Joakim for all support and opportunities during this Ph.D.

Finally, I would like to thank all grant institutions that contribute to this research: CEFET-MG, FAPEMIG, CAPES, CNPq, Simula e UFJF.

*The only certainty is
uncertainty.*

RESUMO

A modelagem da mecânica cardíaca tem levado a descobertas interessantes, porém este continua sendo um problema complexo e de alta demanda computacional, especialmente em modelos eletromecânicos fortemente acoplados. O tecido cardíaco é geralmente considerado como um material hiperelástico, quase incompressível e ortotrópico, fatores que dificultam a solução numérica do modelo. Neste trabalho, melhorias foram realizadas em um simulador da mecânica cardíaca para tratar tais problemas numéricos de forma mais eficiente. Com este simulador mais eficiente foi possível tratar problemas que demandam de um maior esforço computacional, como as análises de sensibilidade e quantificação de incertezas, onde várias simulações precisam ser realizadas. Este tipo de análise tem sido tópico de interesse científico para avaliar a possibilidade de usar simulações personalizadas por paciente em aplicações clínicas. Porém, estas simulações ainda são problemas desafiadores, por causa da grande variabilidade biológica entre pacientes e das incertezas em medidas experimentais e em representações geométricas do coração. Devido a estas incertezas em entradas do modelo, é difícil definir um modelo confiável que possa ser usado em aplicações clínicas. Estudos recentes têm se voltado à investigação de como estas incertezas podem influenciar no resultado de simulações e, conseqüentemente, descobrir como tornar os modelos mais confiáveis. Então, o presente trabalho quantifica incertezas nas geometrias usadas nas simulações para investigar como quantidades de interesse da mecânica cardíaca podem ser afetadas. A abordagem do polinômio caos é utilizada para a quantificação de incertezas em geometrias do ventrículo esquerdo submetidas a simulações da mecânica cardíaca. Inicialmente, as análises foram realizadas usando geometrias simplificadas em simulações da fase de preenchimento ventricular e, posteriormente, análises de quantificação de incertezas em geometrias mais realísticas submetidas a simulações do ciclo cardíaco completo são realizadas.

Palavras-chave: Modelagem mecânica do coração. Quantificação de incertezas. Formulação do Lagrangiano Aumentado. Precondicionadores.

ABSTRACT

Modeling the mechanics of the heart have led to considerable insights, but it still represents a complex and demanding computational problem, especially in a strongly coupled electromechanical setting. Passive cardiac tissue is commonly modeled as a hyperelastic, near-incompressible and orthotropic material, which are properties very challenging for the numerical solution of the model. In particular, near-incompressibility is known to cause numerical issues. In this work, some improvements were done in a cardiac mechanics simulator in order to be more efficient in the treatment of these numerical issues. With the improved solver for cardiac mechanics, it was possible to run problems with higher computational cost, such as sensitivity and uncertainty quantification analyses. This type of analysis has been a topic of scientific interest to assess the possibility of translating patient-specific simulations to clinical applications. However, personalized simulations are still challenging problems, because of the wide biological variability among patients, the uncertainties in experimental measurements and in the geometric representation of the heart. Due to these uncertainties in model inputs, it is difficult to define a reliable model that can be translated to clinical applications. Recent studies have focused on quantifying uncertainties for cardiac models in order to investigate how they can influence simulation results and, consequently, how we can make the models more reliable. Then, the present work also quantifies how uncertainties in the geometry can impact in quantities of interest from cardiac mechanics. The polynomial chaos approach was used to quantify uncertainties in geometries of the left ventricle during cardiac mechanics simulations. Initially, we performed some studies using simplified geometries during ventricular filling phase simulations and, after, we quantify uncertainties in more realistic geometries during the full cardiac cycle.

Keywords: Cardiac mechanics. Uncertainty quantification. Augmented lagrangian formulation. Preconditioners.

TABLE OF CONTENTS

1	Introduction	21
1.1	Motivation	21
1.2	Basic physiological concepts	22
1.2.1	<i>Heart function</i>	22
1.2.2	<i>Electrical activity and contraction</i>	23
1.2.3	<i>Cardiac tissue microstructure</i>	26
1.2.4	<i>Cardiac cycle</i>	27
1.3	Computational simulations	29
1.4	Uncertainty quantification and sensitivity analysis	30
1.5	Objectives	31
1.5.1	<i>Main objective</i>	31
1.5.2	<i>Specific objectives</i>	31
1.6	Outline of the thesis	32
1.6.1	<i>Contributions</i>	33
2	Models and methods	35
2.1	Continuum mechanics concepts	35
2.2	Mechanical problem	37
2.3	Constitutive equations	37
2.3.1	<i>Cardiac tissue constitutive model</i>	38
2.3.2	<i>Incompressibility</i>	39
2.3.3	<i>Nearly incompressibility</i>	39
2.4	Geometrical models	40
2.4.1	<i>Simplified geometry of the left ventricle</i>	40
2.4.2	<i>Patient specific geometry of the left ventricle</i>	42
2.5	Active stress	45
2.5.1	<i>Kerckhoffs et al. (2003) active stress model</i>	46
2.6	Circulatory model	47
2.6.1	<i>LV pressure estimation</i>	51

2.7	Numerical solution of the mechanical problem	53
2.7.1	<i>Variational formulation</i>	54
2.7.2	<i>Penalty method</i>	55
2.7.3	<i>Simo-Taylor-Pister formulation</i>	57
2.7.4	<i>Augmented Lagrangian formulation</i>	57
2.7.5	<i>Finite element method</i>	59
2.7.6	<i>Newton's method</i>	59
2.7.7	<i>Preconditioners</i>	60
2.7.8	<i>Multigrid method</i>	60
2.7.9	<i>Algebraic multigrid preconditioners for elasticity problems</i>	63
2.8	Simulations	65
2.9	Uncertainty quantification and Sensitivity analysis	66
2.9.1	<i>An introductory example</i>	67
2.9.2	<i>Uncertainty quantification techniques</i>	67
2.9.3	<i>Generalized polynomial chaos</i>	69
2.9.3.1	<i>Stochastic collocation method</i>	71
2.9.4	<i>Sensitivity Analysis</i>	73
2.9.4.1	<i>Sobol sensitivity indices</i>	73
2.9.5	<i>Surrogate model calibration</i>	74
2.9.6	<i>ChaosPy</i>	75
2.9.7	<i>Uncertainty quantification in cardiac mechanics</i>	77
3	Cardiac mechanics solver performance	79
3.1	Benchmark problems	79
3.1.1	<i>Benchmark metrics</i>	81
3.1.2	<i>Metric to compare Cardiax with the benchmark participants</i>	82
3.1.3	<i>Experiments</i>	83
3.2	Performance of the preconditioners	89
3.3	Augmented Lagrangian formulation	91
3.4	Effect of tolerance on ALG	95
3.5	Discussions	96

4	Uncertainty quantification in passive filling simulations	98
4.1	Settings	98
4.2	Quantities of interest	99
4.3	Uncertain inputs and experiments	100
4.4	Surrogate model calibration	104
4.5	Preliminary experiment	106
4.6	Experiment 1: Constant wall thickness	107
4.7	Experiment 2: Uncertainty in medial-lateral and apical-lateral regions	109
4.8	Experiment 3: Including uncertainty in apex and basal-lateral region	110
4.9	Global effects on stress and strain	112
4.10	Discussions	113
5	Uncertainty quantification of left ventricle simulations during the cardiac cycle	116
5.1	Settings	116
5.2	Experiments	117
5.2.1	<i>Quantities of interest</i>	118
5.3	Results	120
5.3.1	<i>Surrogate model calibration</i>	120
5.3.2	<i>Uncertainty propagation</i>	120
5.3.3	<i>Sensitivity analysis</i>	122
5.3.4	<i>Stress and strain time series</i>	125
5.4	Discussions	126
6	Conclusion	129
6.1	Future works	130

LIST OF FIGURES

1.1	Heart structure (adapted from Commons (2019)). SVC: superior vena cava, IVC: inferior vena cava, RA: right atrium, LA: left atrium, RV: right ventricle e LV: left ventricle. The red arrow represents the blood pathway in both sides of the heart.	23
1.2	Action potential curve.	24
1.3	Myocyte structure (adapted from Klabunde (2011)).	25
1.4	Action potential propagation through the cardiac tissue (adapted from Commons (2018)).	26
1.5	Myocyte organization in fibers and sheets.	27
1.6	Pressure-volume diagram representing the phases during the cardiac cycle: ventricular filling (1); isovolumetric contraction (2); ejection (3); isovolumetric relaxation (4).	28
1.7	Left ventricle geometry segmentation from magnetic resonance images. Endocardium and epicardium contours marked by different expert raters. (Adapted from Suinesiaputra et al. (2014))	30
1.8	Outline of the uncertainty and sensitivity analysis performed in this thesis. . .	32
2.1	Layered organization of the cardiac tissue.	38
2.2	Simplified geometry of the left ventricle generated from a family of truncated ellipsoids, where r_s is the short axis, r_l the long axis u and v represent rotation angles used in the parametrization. The epicardium surface is denoted by epi and the endocardium by endo.	41
2.3	Fiber orientation for the simplified LV geometry, varying in the transmural direction from -90° at the epicardium surface to $+90^\circ$ at the endocardium.	42
2.4	(a) 17 AHA segments diagram used in the mesh generator. (b) Example of LV geometry created with the presented mesh generator. Higher values of wall thickness in the basal-lateral segments were chosen, while the short axis was 4.0 cm and the long axis was 6.0 cm.	43
2.5	Parameterized LV finite element mesh generation.	44

2.6	Fiber orientation for the personalized LV geometry, with helix angles $\alpha_{endo} = 60^\circ$, $\alpha_{epi} = -60^\circ$, $\beta_{endo} = -65^\circ$ and $\beta_{epi} = 25^\circ$	45
2.7	Active stress curve used to represent the ventricle contraction.	47
2.8	Circuit scheme for the lumped parameter model adopted in this work, in order to reproduce the time varying pressure in the left ventricle cavity.	48
2.9	V-cycle scheme for the multigrid method.	62
2.10	Types of cardiac mechanics simulations performed in the present work. (a) Benchmark problems. (b) Simulation of LV function during the full cardiac cycle.	66
2.11	Stochastic solutions for the decaying process. The solid line represents the mean solution, whereas the dashed lines represent the deviation of random solutions.	68
2.12	Mean and standard deviation errors for Monte Carlo (MC) and generalized polynomial chaos (gPC) methods.	70
3.1	Undeformed and deformed configurations of the benchmark problems 1-3. The arrows in the undeformed configuration for problem 3 indicates the fiber orientation.	80
3.2	Problem 1 geometry, where observed measures are: the deformed z position in the green point; the deformed configuration of the red line; and the strains computed in axial directions using the blue points. (extracted from Land et al. (2015))	81
3.3	Undeformed geometry used in problems 2 and 3, with green points indicating location to measure apex displacement at endocardium and epicardium; middle wall apex-base line in red and blue points to compute strains. (a) Blue points used to compute longitudinal and radial strains ($v_i = 0$) at the points p1-p9 under the red line. (b) Blue points used to compute circumferential strains ($v_i = \pi/10$) at points p1-p9. (extracted from Land et al. (2015))	82
3.4	Benchmark results, where the labels in this graph refer to all the codes tested in the benchmark paper, except our results which were added here under the label Cardiax.	85

3.5	Problem 1: (a) deformation of the line $(x, 0.5, 0.5)$; (b) strain along the lines in direction of x -, y - and z -axes.	86
3.6	Problem 2: (a) deformation of a line in the middle of ventricular wall and (b) strain measures in the circumferential (CIRC), longitudinal (LONG) and transmural (TRANS) directions at different positions.	87
3.7	Problem 3: (a) deformation of a line in the middle of ventricular wall; (b) twisting motion of the same line; and (c) strain measures in the circumferential (CIRC), longitudinal (LONG) and transmural (TRANS) directions at different positions.	88
3.8	Twisting motion of the middle wall line for problem 3.	88
3.9	Comparison of GMRES iterations for each loading parameter (λ) for different mesh discretizations of the geometry in the benchmark problems.	90
4.1	Quantities of interest. (a) Left ventricular torsion sketch adapted from Shavik et al. (2017) with circles representing the basal and apical slices. (b) Measured positions for W_D at the apex and base, mean fiber stress and strain at segment 12 (highlighted in blue).	100
4.2	17 AHA segments diagrams representing the three experiments performed, with the colored segments indicating where the wall thickness was considered as uncertain. (a) Experiment 1: uncertain constant wall thickness. (b) Experiment 2: uncertainty in medial-lateral and apical-lateral regions. (c) Experiment 3: adding uncertainty in basal-lateral and apical-lateral segments.	101
4.3	Long axis section of geometrical samples used in the third experiment. Color maps represents the endocardial to epicardial distance.	103
4.4	Main (S_m) and Total (S_t) Sobol sensitivity indices for the preliminary experiment.	106
4.5	Experiment 1: Main (S_m) and Total (S_t) Sobol sensitivity indices for each quantity of interest considering 15% and 30% of uncertainty for wall thickness and 15% of uncertainty for the other parameters.	108
4.6	Experiment 2: Main (S_m) and Total (S_t) Sobol sensitivity indices for each quantity of interest considering 15% and 30% of uncertainty for wall thickness and 15% of uncertainty for the other parameters.	110

4.7	Experiment 3: Main (S_m) and Total (S_t) Sobol sensitivity indices for torsion, W_D base and apex considering 15% and 30% of uncertainty for wall thickness and 15% of uncertainty for the other parameters.	111
4.8	Bull's eye plot of the uncertainty propagation in mean fiber (a) stress and (b) strain for all segments. The uncertainty range was 30% for wall thickness and 15% for the other parameters.	112
5.1	Mean value and variations in the 95% confidence interval for volume and pressure profiles as a function of time and PV-loop, respectively, for Experiment 2.	122
5.2	Probability densities of QoIs for experiments 2 and 4.	122
5.3	Experiment 1: sensitivity analysis with main and total Sobol indices (top) and time-averaged indices (bottom). Striped bars represent the total Sobol indices while the solid bars show the main indices.	123
5.4	Experiment 3: sensitivity analysis with main and total Sobol indices (top) and time-averaged indices (bottom).	124
5.5	Experiment 2: uncertainty propagation for (a) stress and (b) fiber strain time series in each AHA segment s_i , for $i = 1, \dots, 17$. The figures also show the mean stress and fiber strain over the whole ventricle (top left).	125

LIST OF TABLES

2.1	Parameter values for the active stress model.	47
2.2	Parameters for the circulatory model.	51
3.1	Average solutions and standard deviation computed at the key points from the results of the cardiac mechanics benchmark (Land et al., 2015).	84
3.2	Block (B) and nodal (N) AMG preconditioners performance study: number of Newton iterations and average of GMRES iterations at some selected loading parameters (λ)	89
3.3	Block AMG preconditioner: average of GMRES iterations at different loading parameters (λ) and total solution time in seconds for the benchmark problems using different mesh refinements.	91
3.4	Nodal AMG preconditioner: average of GMRES iterations at different loading parameters (λ), and total solution time in seconds for the benchmark problems using different mesh refinements.	91
3.5	Comparison of STP and ALG: bulk modulus κ , global volume change (VC), volumetric changes measured as $\max \tilde{J} - 1 $ within all finite elements, <i>error</i> and time spent by the linear solver using the block (B-AMG) and nodal (N-AMG) preconditioners.	94
3.6	Newton iterations and average of GMRES iterations (its) at different loading levels (λ) for the benchmark problems. For ALG results, the Uzawa iterations (Uz) are also presented. (Problem 2 with STP formulation used $\kappa = 300$ kPa and with ALG used $\kappa = 40$ kPa; Problem 3 with STP formulation used $\kappa = 1000$ kPa and with ALG used $\kappa = 100$ kPa).	95
3.7	Effect of the tolerance (<i>tol</i>) on the error and on the linear solver time using ALG using the block (B-AMG) and nodal (N-AMG) preconditioners.	96
4.1	Baseline values of the left ventricle wall thickness for each AHA segment reported by Bai et al. (2015).	102
4.2	Model inputs considered as uncertain.	104

4.3	Maximum relative error (reported as %) between all quantities of interest for variance and total Sobol sensitivity indices when the polynomial order and the number of samples are varied.	105
4.4	Leave-one-out error and Q^2 coefficient for each QoI.	105
4.5	Experiment 1: uncertainty propagation for each quantity of interest, considering 15% and 30% of uncertainty for wall thickness and 15% for the other model inputs.	107
4.6	Experiment 2: uncertainty propagation for each quantity of interest, considering 15% and 30% of uncertainty for wall thickness and 15% for the other model inputs.	109
5.1	Uncertain model inputs, described through Normal distribution with 5% for the coefficient of variation.	117
5.2	Q^2 coefficient obtained by the leave-one-out cross validation test for the QoIs in each experiment.	120
5.3	Mean value, standard deviation (STD) and the corresponding coefficient of variation (COV) of the quantities of interest for all experiments.	121

List of Abbreviations

AHA	American heart association
ALG	Augmented lagragian approach
AMG	Algebraic multigrid
AP	Action potential
B-AMG	Block algebraic multigrid preconditioner
CG	Conjugate gradient
CIRC	Circumferential direction
COV	Coefficient of variation
EDV	End diastolic volume
EF	Ejection fraction
EDPVR	End diastolic pressure volume relationship
ESPVR	End systolic pressure volume relationship
ESV	End systolic volume
FEM	Finite element method
GMRES	Generalized minimal residual method
gPC	Generalized polynomial chaos
its	Iterations
IVC	Inferior vena cava
LA	Left atrium
LBBB	Left bundle branch block
LONG	Longitudinal direction
LOO	Leave one out
LV	Left ventricle
MC	Monte Carlo
N-AMG	Nodal algebraic multigrid preconditioner

QoI	Quantity of interest
RA	Right atrium
RV	Right ventricle
SA	Sensitivity analysis
SOR	Successive over-relaxation
STD	Standard deviation
STP	Simo-Taylor-Pister variational formulation
SV	Stroke volume
SVC	Superior vena cava
TRANS	Transmural direction
UQ	Uncertainty quantification
Uz	Uzawa iterations
VC	Volumetric change
WT	Wall thickness

List of Symbols

\mathbf{u}	Displacement field
\mathbf{F}	Deformation gradient tensor
Ω_0	Undeformed configuration
Ω	Deformed configuration
t	time
\mathbf{C}	Right Cauchy-Green strain tensor
\mathbf{E}	Green-Lagrange strain tensor
$\boldsymbol{\sigma}$	Cauchy stress tensor
\mathbf{P}	First Piola-Kirchhoff stress tensor
\mathbf{S}	Second Piola-Kirchhoff stress tensor
Ψ	Strain energy function
\mathbf{f}	Longitudinal fiber direction
\mathbf{s}	Sheet direction
\mathbf{n}	Direction orthogonal to fiber and sheet direction
p	Hydrostatic pressure
J	Volume change caused due to deformation
r_s	Short axis diameter, for the benchmark ventricular geometry
r_l	Long axis length, for the benchmark ventricular geometry
u	Angle in the circumferential direction, for the benchmark ventricular geometry
v	Angle in the apex-base direction, for the benchmark ventricular geometry
α_{endo}	Angle of longitudinal fiber direction on endocardial surface
α_{epi}	Angle of longitudinal fiber direction on epicardial surface
β_{endo}	Angle of sheet direction on endocardial surface
β_{epi}	Angle of sheet direction on epicardial surface
T_{ref}	Magnitude of active stress curve

T_a	Normalized active stress curve
κ	Bulk modulus
Π	Energy functional
\tilde{J}	Dilatation variable from Simo-Taylor-Pister formulation
μ	Lagrange multiplier from Augmented Lagrangian approach
ξ^c	Constant weight for Uzawa iteration
tol	Tolerance value
λ	load parameter
\mathbf{K}	Stiffness matrix
ξ	Vector of uncertain model inputs
P	Number of samples required to construct the polynomial chaos expansion
S_m^i	Main Sobol sensitivity index
S_t^i	Total Sobol sensitivity index
TAS_m^i	Time-averaged main Sobol sensitivity index
TAS_t^i	Time-averaged total Sobol sensitivity index
\mathbb{V}	Variance
\mathbb{E}	Expected value
ϵ_r	Maxium relative error between polynomial chaos of different degrees
ϵ_a	Maxium absolute error between polynomial chaos of different degrees
Err_{LOO}	Leave-one-out error
Q^2	Coefficient that measures the surrogate model quality
$error$	Relative error to compare codes for the benchmark
S_i	Strain measures for the benchmark
W_D	Ratio of deformed to undeformed wall thickness
T	Normalized left ventricle torsion
σ_f	Fiber stress
e_f	Fiber strain
N_s	Number of samples
d	Polynomial chaos degree

1 Introduction

In this chapter we present a brief introduction, with the motivation and some concepts about cardiac physiology which are necessary to study the mechanical activity of the heart. The thesis goals and text organization are presented next.

1.1 Motivation

Every year 17.9 million people die from cardiovascular diseases (CVD), corresponding to approximately 31% of all deaths worldwide and three quarters of them occur in low-income and middle-income countries (World Health Organization, 2019). The majority of deaths associated with cardiovascular diseases are due to myocardium infarction and stroke. United States spent \$351.2 billion between 2014 and 2015 with CVDs, where coronary heart disease is the leading cause of CVD death, followed by stroke, high blood pressure, heart failure and diseases of the arteries (Benjamin et al., 2019).

Myocardium infarction occurs due to alterations in blood perfusion of the cardiac tissue, which changes the oxygen and nutrients supply. Consequently, the cardiac tissue is damaged and ventricular pumping is limited due to mechanical dysfunction. Heart failure usually affects the heart's left side, where the muscle is unable to pump enough blood to the body. It stretches in order to contract more strongly and become enlarged, while the cardiac mass increases because the cells get bigger.

Therefore, the need of improvements in the understanding and treatments of cardiac diseases is very important, which is the motivation for several researches where the focus is the heart function, as the present work.

The electrical and mechanical activities of the heart, both at the cellular level and on organ scale, have received considerable efforts from the scientific community with focus in understanding its complex, multiscale and multiphysics nature. However, there are still fundamental mechanisms that are not fully understood, for instance related to cardiac arrhythmias (Arevalo et al., 2016), heart failure (Tomaselli and Marbán, 1999), and other significant clinical problems. Within this context, mathematical modeling and computer simulations have been useful tools to assess physiological and pathophysiological

conditions of the heart. More specifically, with cardiac mechanics it is possible to reproduce the tissue deformation and, for instance, perform simulations to verify the heart pumping in different scenarios. Naturally, the complex physiology of the heart translates into complex computational models, which require the use of efficient and robust methods for numerical simulations.

Due to the development of efficient and robust simulators which are also able to provide a better representation of the heart function, the interest of leading this tool to clinical applications has been increased. Consequently, it is necessary to consider patient-specific models which can help in diagnostics and in the development of individual treatments. However, the construction of personalized models is a challenge, because of the uncertainty associated to the experiments used to measure patient properties and the wide biologic variability found among patients. Then, it is necessary to assess how these models behave when the model inputs have a large variability and how the uncertainties in measurements propagates to the results. In this context, recent studies have focused on uncertainty quantification of models describing the electrical and mechanical activity of the heart (Osnes and Sundnes, 2012; Hurtado et al., 2017).

1.2 Basic physiological concepts

This chapter presents some physiological concepts mentioned throughout the text. A comprehensive description can be found in the book of Klabunde (2011).

1.2.1 *Heart function*

The heart works as a double pump with four chambers, comprising two atria in the superior region and two ventricles in the inferior part, as shown in Figure 1.1. Atria and ventricles are separated by the atrioventricular septum, which contains the tricuspid valve in the right side and the mitral valve in the left side. The right ventricle (RV) is connected to the pulmonary artery through the pulmonary valve, while the left ventricle (LV) is connected to the aorta via the aortic valve. The ventricular walls are externally involved by a thin layer named epicardium and internally by the endocardium layer, with the cardiac muscle between them. The left ventricular wall is about three times thicker than the right ventricular wall, due to the left ventricle function of pumping blood to the

body, while the atria walls are considerably thinner.

The right side of the heart pumps blood to the lungs, where it receives oxygen and returns to the left side, which then pumps the oxygenated blood to the body. The right atrium (RA) receives the blood from the superior (SVC) and inferior (IVC) vena cava, which carries blood from the circulatory system. This venous returning passes by the right atrium and fill the right ventricle, due to the atrial contraction. When the right ventricle contracts, the blood is ejected to the pulmonary artery. Whereas, the left atrium (LA) is filled with blood coming from the lungs, then the blood flows to the left ventricle passively when mitral valve opens and, finally, the atrium contracts to complete the ventricular filling. With the valves closed, the left ventricle contracts, consequently the pressure increases and when a certain value is achieved, the aortic valve opens and the blood is ejected to the arterial system.

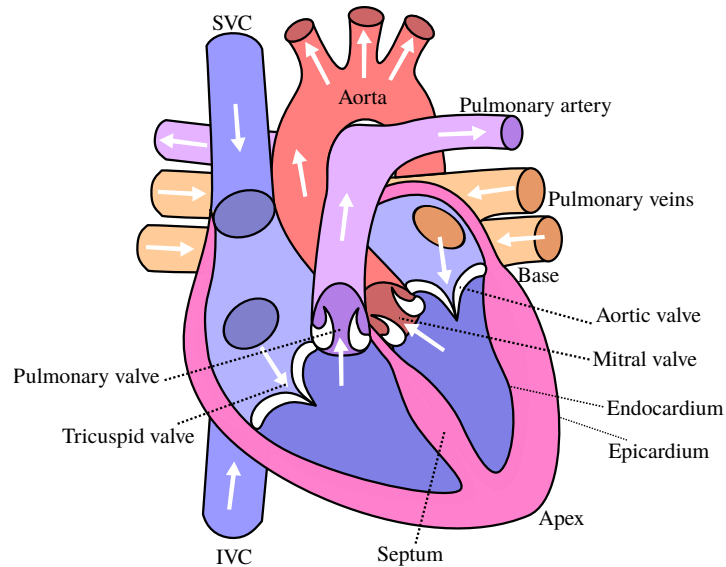


Figure 1.1: Heart structure (adapted from Commons (2019)). SVC: superior vena cava, IVC: inferior vena cava, RA: right atrium, LA: left atrium, RV: right ventricle e LV: left ventricle. The red arrow represents the blood pathway in both sides of the heart.

1.2.2 *Electrical activity and contraction*

The cardiac cells or myocytes are excitable cells, that have the ability of actively responding to an electrical stimulus. They are connected in a certain manner that a cell can pass an electrical signal to neighboring cells. This ability allows an electrical stimulation in some part of the heart to propagate through the cardiac tissue.

When cardiac cells are at rest, there is a potential difference through the cell membrane, due to the difference of ions concentration in intracellular and extracellular media. When these cells are electrically stimulated, the transmembrane potential changes from a negative value to a positive one, a process which is named depolarization. This process is very fast and it is followed by a slow process, the repolarization, which recovers the potential difference to its resting value. The full cycle of depolarization and repolarization, as shown in Figure 1.2, is called action potential (AP).

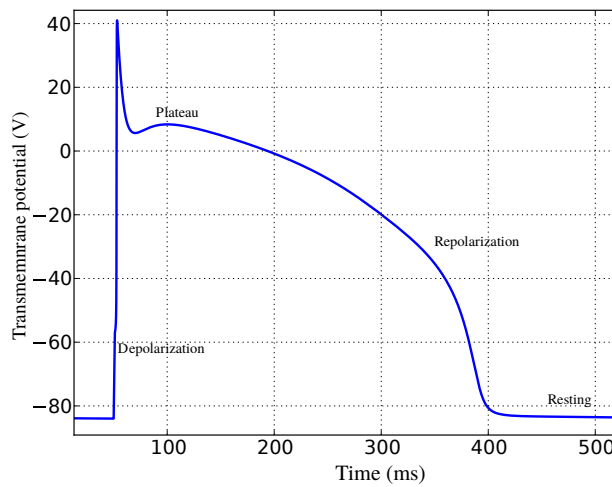


Figure 1.2: Action potential curve.

The myocytes have generally one nucleus with a diameter of $25\mu\text{m}$ and a length of $100\mu\text{m}$, approximately. They have a striated structure due to the organization of myofibrils arrangement, which have several myofilaments, as shown in Figure 1.3. The segment between two Z lines represents the basic contractile unit of the myocyte, named as sarcomere. The sarcomere length is an important feature in the generated force to the contraction, which under normal conditions varies between 1.6 and $2.2\mu\text{m}$ in human hearts (Klabunde, 2011).

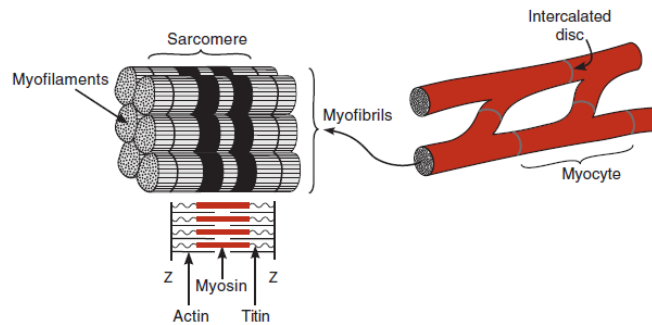


Figure 1.3: Myocyte structure (adapted from Klabunde (2011)).

The sarcomere has thin and thick filaments that represent about 50% of the cell volume. Thick filaments have a protein called myosin, while thin filaments have actin and other proteins. Chemical interactions among the filaments of actin and myosin during the excitation-contraction coupling make the sarcomere to shorten as the actin and myosin slide past each other. This sliding happens due to the increasing in calcium concentration during the action potential depolarization. With repolarization, calcium concentration decreases and the filaments slide back to the initial position. When several sarcomeres in series have shortened, the result is the myocyte contraction, where the active force responsible by contraction is related to the dynamic of the proteins involved in the sarcomere shortening.

The electrical activity of the heart is directly related to the organ function, which is to pump blood to the whole body, carrying nutrients and oxygen to the cells. The action potential triggers the cell contraction, causing the contraction of the whole organ, which is fundamental for blood pumping. AP is generated spontaneously in the right atrium, as shown in Figure 1.4, in a region named sinoatrial node, responsible by the heart rhythm. All the cells must work in a synchronous manner during the contraction in order to pump blood effectively, and to this end the action potential must propagate through the cardiac tissue properly. After its generation in the sinoatrial node, the AP propagates to the right and left atria before passing to the ventricles through left and right bundle branches. Therefore, the atria contract first in order to fill the ventricles before their contraction.

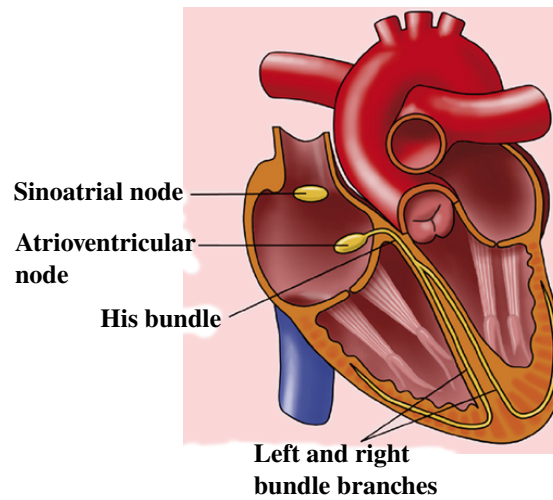


Figure 1.4: Action potential propagation through the cardiac tissue (adapted from Commons (2018)).

1.2.3 Cardiac tissue microstructure

Anatomical studies performed by Streeter et al. (1969) and LeGrice et al. (1995) showed that cardiac tissue is a material strongly anisotropic, due to its cells organization. The myocytes are organized in muscular fibers and they are aligned preferably with the macroscopic fiber direction, as shown in Figure 1.5. The fiber direction varies smoothly between endocardium and epicardium. Furthermore, these fibers are also organized in discrete layers (sheets) coupled to collagen. They are coupled to each other and can slide among them. The orientation of the sheets is usually normal to the ventricular surface, except in the subendocardial and subepicardial regions, where the sheets are aligned with the ventricular wall.

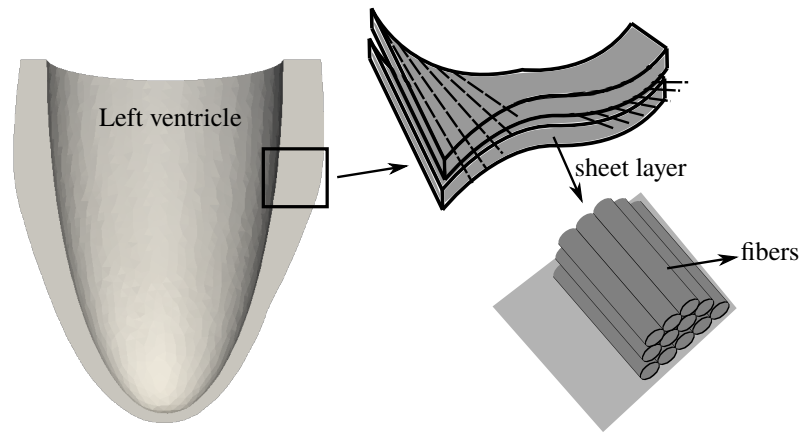


Figure 1.5: Myocyte organization in fibers and sheets.

This complex fiber organization strongly influences the electrical conduction and also the mechanical response of the cardiac tissue. For instance, the stiffness and conductivity are higher in the fiber direction. Therefore, mathematical models usually must consider the microstructure of the tissue to reproduce the heart function.

1.2.4 *Cardiac cycle*

The cardiac cycle can be divided in two parts: systole and diastole. The systole comprises the events associated to contraction and ventricular ejection, while diastole refers to the rest of the cycle, including ventricular filling and relaxation. The sequence of these events during the cardiac cycle causes changes in volume and pressure in the chambers such as in the left ventricle, which can be measured and analyzed over time to assess the heart function. Another valuable tool used to analyze ventricular function is the pressure-volume loop, where the ventricular pressure is related to volume during the entire cardiac cycle.

The pressure-volume loop for the left ventricle is presented in Figure 1.6, which summarizes the four phases of the cycle: filling, isovolumetric contraction, ejection and isovolumetric relaxation. The vertical segments represent the isovolumetric phases where the LV cavity volume remains constant. The inferior curve shows the ventricular filling, whereas the superior curve represents the ejection phase.

Some important clinical measurements can be directly extracted from this diagram, such as the cavity volume in the end diastole (EDV) and systole (ESV), besides the stroke

volume (SV) that is the difference between EDV and ESV and represents the blood volume pumped. Another important quantity that can be extracted is the ejection fraction (EF), which is the ratio between SV and EDV, representing the percentage of blood that is pumped each time the ventricle contracts. The diagram shape changes significantly when the patient has some pathology such as valve disease and heart failure.

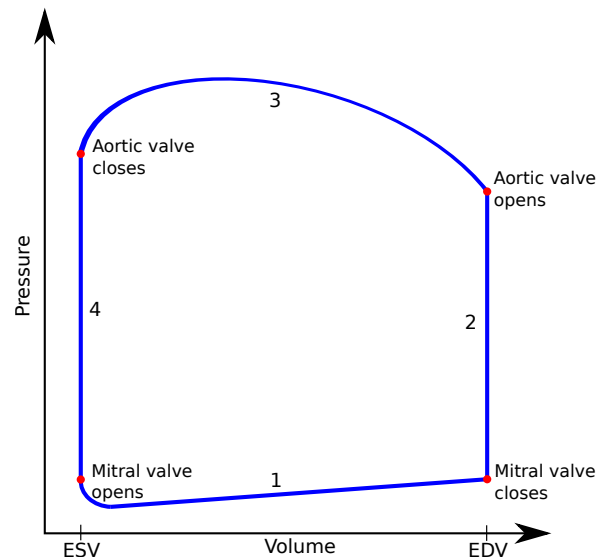


Figure 1.6: Pressure-volume diagram representing the phases during the cardiac cycle: ventricular filling (1); isovolumetric contraction (2); ejection (3); isovolumetric relaxation (4).

The ventricular filling phase is initiated by the mitral valve opening. At this point, the atrium is totally filled and the blood flows rapidly to the ventricle, which causes increase of pressure in the ventricle.

When the electrical signal arrives at the ventricle apex, the myocytes are stimulated and intracellular calcium concentration increases, due to depolarization, which in turn increases the active stress in the muscular fibers that starts the contraction. The increasing of active stress makes the pressure to rise rapidly, which results in the closing of the valves. With all valves closed, the cavity volume remains constant, therefore the contraction is called isovolumetric. Although the cavity volume is constant, the ventricle has a significant change in its geometry, due to the contraction. As the contraction continues without ejection, the pressure remains increasing rapidly until the aortic valve opens, indicating the end of the isovolumetric contraction phase.

In the moment that cavity pressure becomes higher than aortic pressure, the

aortic valve opens and blood is ejected from the ventricle to the circulatory system, characterizing the ejection phase. With repolarization, the active tension decreases and ejection rate falls, then ventricular pressure also decreases and the muscle start relaxing, however ejection continues due to the kinetic energy of the blood.

The ventricle continues to relax and when the total energy in the ventricle is less than the energy in the outflow tracts, occurs a reversal in the energy gradient and the aortic valve closes. This point is the beginning of the isovolumetric relaxation phase, where the volume remains constant because the valves are closed. The cavity volume remains constant during this phase until the ventricular pressure becomes lower than atrial pressure, when the cycle starts again.

1.3 Computational simulations

The electrical and mechanical activity of the heart, both at the cellular level and on organ scale, have received considerable efforts from the scientific community with focus in understanding its complex, multiscale and multiphysics nature. However, there are still fundamental mechanisms that are not completely understood. Within this context, mathematical modeling and computer simulations have been useful tools to assess physiological and pathophysiological conditions of the heart. Naturally, the complex physiology of the heart translates into complex computational models, which require the use of efficient and robust methods for numerical simulations.

Cardiac electrophysiology has been studied extensively in the last years (Sundnes et al., 2007; Vigmond et al., 2008), and there are also numerous studies of cardiac mechanics and coupled electro-mechanical activity. Some studies of cardiac mechanics have focused on the impact of deformation on the electrical activity (Oliveira et al., 2013; Franzone et al., 2016). Others have addressed specific pathological conditions, such as cardiac alternans and arrhythmia (Hazim et al., 2015), heart failure (Mann and Bristow, 2005), and growth and remodeling resulting from a heart infarction and therapeutical interventions (Lee et al., 2016). An important effort to verify existing mechanics codes and create an unified set of benchmark problems in cardiac mechanics was presented by Land et al. (2015).

In spite of the increasing number of studies in cardiac mechanics, there are relatively few works focusing on the efficient solution of the model equations (Land et al., 2012;

Sundnes et al., 2014; Hadjicharalambous et al., 2014). The numerical performance of the simulations is an important feature for research, and in particular for clinical applications of the models. Coupled electro-mechanics simulations typically requires high spatial and temporal resolution, and the resulting computational problem is challenging to solve within the time constraints posed by clinical applications.

1.4 Uncertainty quantification and sensitivity analysis

Computational models of cardiac electro-mechanics have become valuable tools in medical research, and the development of patient specific simulations targeted for clinical is a research topic of substantial interest in recent years (Lee et al., 2014; Trayanova and Winslow, 2011; Oliveira et al., 2018). Fitting a model to an individual patient typically includes constructing a patient-specific geometry from medical images, and fitting a number of model parameters to match relevant measurements from the patient (Balaban et al., 2018). Both the geometrical reconstruction and the parameter fitting may give rise to significant uncertainty in the resulting model, and it is of interest to quantify the impact of this uncertainty on the model predictions. Figure 1.7 shows an example for the process of left ventricle segmentation, where different experts marked the endocardium and epicardium contours in a resonance magnetic image. The differences among experts are visible and it impacts directly in the reconstructed geometry of the organ.

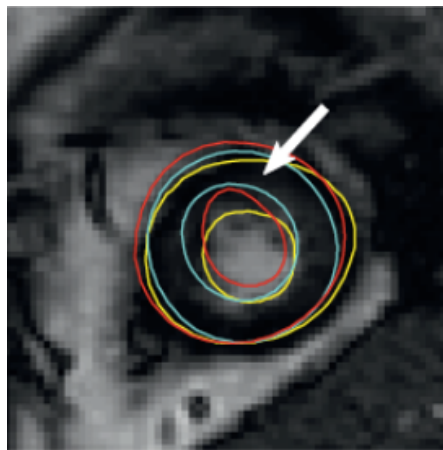


Figure 1.7: Left ventricle geometry segmentation from magnetic resonance images. Endocardium and epicardium contours marked by different expert raters. (Adapted from Suinesiaputra et al. (2014))

Previous studies of uncertainty in cardiac models include Hurtado et al. (2017), which presented uncertainty quantification of a cardiac electro-mechanics model. An UQ analysis in cardiac electrophysiology was also presented by Quaglino et al. (2018), which studied the impact of fiber orientation and conductivities on activation dynamics. In the context of cardiac mechanics, uncertainties in material properties of the cardiac tissue were studied by Osnes and Sundnes (2012), and more recently by Rodríguez-Cantano et al. (2019). UQ and sensitivity analysis (SA) have also been performed for other parts of the cardiovascular system, including uncertainties in flow simulations within arteriovenous fistulae (Huberts et al., 2014), uncertainty in arterial model constitutive parameters (Holzapfel et al., 2000), and in geometry and wall thickness of abdominal aortic aneurysms (Biehler and Wall, 2018).

1.5 Objectives

The present work has focus on the uncertainty quantification and sensitivity analysis of cardiac mechanics simulations in order to understand the relation between the uncertainties in model inputs and the simulations results, contributing to the translation of computational simulations to clinical applications.

1.5.1 *Main objective*

This thesis has the goal of showing how uncertainties in geometrical models can impact in model predictions.

1.5.2 *Specific objectives*

An initial step in the work was to make some modifications in the cardiac mechanics solver proposed by Rocha (2014), in order to improve its performance by modifying the variational formulation and the preconditioner used in the iterative solver for linear systems. Its performance was assessed and the solver results were compared with respect to a benchmark for cardiac mechanics simulations.

Then, a parameterized approach to generate left ventricle meshes was developed, as proposed by Rodrigues et al. (2015). It is based on wall thickness measures, which were used to introduce uncertainties in the geometrical models.

Using the improved solver and the approach to generate LV geometries, analyses are performed considering uncertainties in different inputs of cardiac mechanics models, as shown in Figure 1.8.

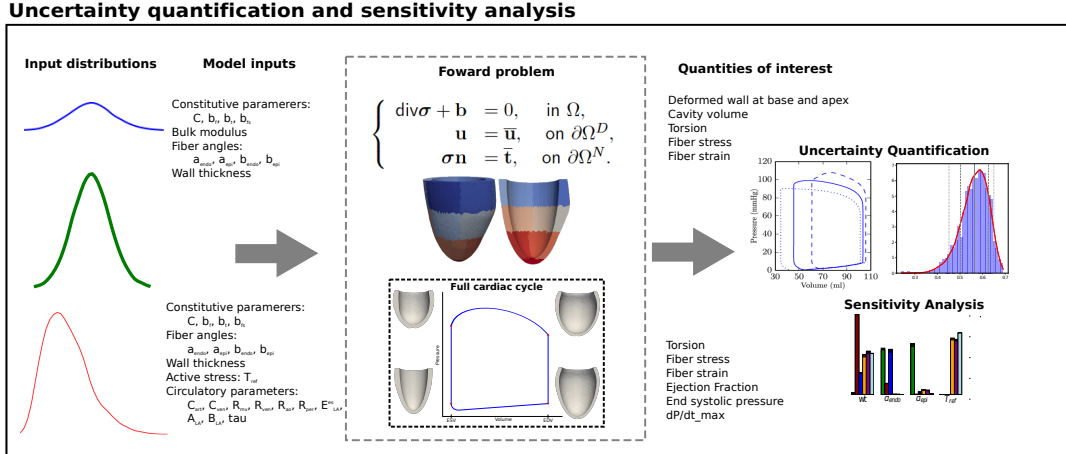


Figure 1.8: Outline of the uncertainty and sensitivity analysis performed in this thesis.

The simulations consider the left ventricle function in different moments, where the first analyses are focused on the passive filling phase and after simulations considering all phases of the cardiac cycle are performed. We hypothesize that uncertainty in geometrical models are at least as important as uncertainty in material properties, and test this hypothesis by performing UQ and sensitivity analysis for the left ventricle simulations. Then, we identify quantities of interest that can be influenced significantly by this type of uncertainty, such as stress and strain in the ventricle wall, cavity volumes and ejection fraction.

1.6 Outline of the thesis

The text is organized in six chapters, where all concepts necessary to understand the work are presented, followed by the results for the chosen experiments.

The second chapter presents the equations to model the cardiac mechanics, including passive and active deformation, geometrical models, besides boundary conditions in order to consider the circulatory system. Then, the numerical solution of the mechanical problem is presented, describing the variational formulation adopted which includes the mixed three field and Augmented Lagrangian formulations, besides the preconditioning

strategy used to improve the simulations performance. Finally, this chapter presents the techniques used to perform uncertainty quantification and sensitivity analyses.

Next, results for different experiments are presented, where in chapter 3 the cardiac mechanics solver is compared with respect to a benchmark and then experiments are performed to assess the performance of the Augmented Lagrangian approach combined to a multigrid preconditioner. Whereas in chapter 4, experiments are performed in order to quantify how uncertainties in model inputs of cardiac mechanics can impact in predictions of left ventricle passive filling simulations. Finally, chapter 5 presents results for the same type of analysis, but considering simulations of the left ventricle function during the entire cardiac cycle.

In the end, conclusions are presented and possibilities of future works are listed.

1.6.1 Contributions

The presented results have been disseminated through the following publications:

- Papers published in journals
 - Joventino Oliveira Campos, Rodrigo Weber dos Santos, Joakim Sundnes, and Bernardo Martins Rocha. Preconditioned augmented lagrangian formulation for nearly incompressible cardiac mechanics. *International Journal for Numerical Methods in Biomedical Engineering*, 34(4):e2948, 2018
 - Joventino Olivera Campos, Joakim Sundnes, Rodrigo Weber dos Santos, and Bernardo Martins Rocha. Effects of left ventricle wall thickness uncertainties on cardiac mechanics. *Biomechanics and modeling in mechanobiology*, 2019.
 - Joventino Olivera Campos, Joakim Sundnes, Rodrigo Weber dos Santos, and Bernardo Martins Rocha, 2019. Uncertainty quantification and sensitivity analysis of left ventricular function during the full cardiac cycle. *Philosophical Transactions of the Royal Society A: Mathematical, Physical and Engineering Sciences*. (submitted)
- Conference papers
 - J. O. Campos, R. Weber dos Santos, J. Sundnes, and B. M. Rocha. Augmented lagrangian approach for quasi-incompressible cardiac mechanics. *Mecánica*

Computacional, XXXIV:1101–1114, 2016.

- Gilmar Ferreira da Silva Filho, Joventino Oliveira Campos, and Bernardo Martins. Unit test framework for finite element based computational biomechanics software. *Revista Mundi Engenharia, Tecnologia e Gestão*, 4(3):153–1–153–14, 2019. ISSN 2525-4782.
- Gustavo Montes Novaes, Joventino Oliveira Campos, Enrique Alvarez-Lacalle, Sergio Alonso Muñoz, Bernardo Martins Rocha, and Rodrigo Weber dos Santos. Combining polynomial chaos expansions and genetic algorithm for the coupling of electrophysiological models. In *Computational Science – ICCS 2019*, pages 116–129, Cham, 2019. Springer International Publishing. ISBN 978-3-030-22744-9.
- Joventino Oliveira Campos, Rodrigo Weber dos Santos, Joakim Sundnes, and Bernardo Martins Rocha. Impact on cardiac cycle due to uncertainties in left ventricle simulations. In *Proceedings of the XXII Encontro Nacional de Modelagem Computacional e X Encontro de Ciência e Tecnologia de Materiais*, pages 1–11, Juiz de Fora, 2019

2 Models and methods

Some continuum mechanics concepts indispensable to present the equations used to reproduce the deformation of the cardiac tissue are presented here, where the concepts of strain and stress are detailed as well as the equilibrium and constitutive equations. More details in continuum mechanics can be found in the specialized literature (Holzapfel, 2000; Javier Bonet, 2008). The other models and their coupling used in the left ventricle simulations are also presented, such as the geometrical, active stress and circulatory models. Then, numerical methods used to solve the mechanical model are presented, describing the variational formulation used and the preconditioners applied to the iterative linear solver. Finally, the techniques used to perform uncertainty quantification and sensitivity analysis are presented.

2.1 Continuum mechanics concepts

The motion of a continuum body can be described by

$$\mathbf{x} = \chi(\mathbf{X}, t), \quad (2.1)$$

where \mathbf{x} are the body particles coordinates at time t , \mathbf{X} are the particles coordinates when the body is in the undeformed configuration Ω_0 , and χ is a function that describes the motion. The displacement field that assigns a new position for all particles in the deformed configuration Ω is:

$$\mathbf{U}(\mathbf{X}, t) = \mathbf{x} - \mathbf{X}, \quad (2.2)$$

A material element $d\mathbf{X}$ in the undeformed configuration is transformed in $d\mathbf{x}$ at time t through the motion χ . Then, the relation between $d\mathbf{X}$ and $d\mathbf{x}$ is given by

$$d\mathbf{x} = \chi(\mathbf{X} + d\mathbf{X}, t) - \chi(\mathbf{X}, t) = (\nabla\chi)d\mathbf{X}. \quad (2.3)$$

Defining $\mathbf{F} = \nabla\chi$, results in

$$d\mathbf{x} = \mathbf{F}d\mathbf{X}, \quad (2.4)$$

where \mathbf{F} is known as the deformation gradient tensor, which represents the gradient of $\chi(\mathbf{X}, t)$ with respect to the undeformed configuration. The determinant of the deformation gradient

$$J = \det(\mathbf{F}) \quad (2.5)$$

measures the volume change caused due to deformation.

The relation between ds and dS , the lengths of $d\mathbf{x}$ and $d\mathbf{X}$, respectively, is given by

$$ds^2 = d\mathbf{x} \cdot d\mathbf{x} = \mathbf{F}d\mathbf{X} \cdot \mathbf{F}d\mathbf{X} = d\mathbf{X} \cdot (\mathbf{F}^T\mathbf{F})d\mathbf{X}, \quad (2.6)$$

where $\mathbf{C} = \mathbf{F}^T\mathbf{F}$ is the right Cauchy-Green tensor.

If we instead consider the change in the squared length of an element, we obtain

$$\begin{aligned} d\mathbf{x}^2 - d\mathbf{X}^2 &= d\mathbf{X} \cdot \mathbf{C}d\mathbf{X} - d\mathbf{X}^2 \\ &= d\mathbf{X} \cdot (\mathbf{C} - \mathbf{I})d\mathbf{X} \\ &= d\mathbf{X} \cdot 2\mathbf{E}d\mathbf{X}, \end{aligned} \quad (2.7)$$

where $\mathbf{E} = \frac{1}{2}(\mathbf{C} - \mathbf{I})$ is the Green-Lagrange strain tensor.

The Cauchy stress tensor relates the unit vector \mathbf{n} to the current surface traction \mathbf{t}

$$\mathbf{t} = \boldsymbol{\sigma}\mathbf{n}, \quad (2.8)$$

where the components σ_{ij} define the stress state in a point inside the material in the deformed configuration.

The first Piola-Kirchhoff stress tensor

$$\mathbf{P} = J\boldsymbol{\sigma}\mathbf{F}^{-T} \quad (2.9)$$

is asymmetric and describes the stress in the deformed configuration with respect to the unit area of undeformed configuration. The second Piola-Kirchhoff stress tensor

$$\mathbf{S} = J\mathbf{F}^{-1}\boldsymbol{\sigma}\mathbf{F}^{-T} = \mathbf{F}^{-1}\mathbf{P}, \quad (2.10)$$

is symmetric and describes the stress in the undeformed configuration with respect to the

unit area also in undeformed configuration.

2.2 Mechanical problem

After presenting the continuum mechanics concepts, it is possible to describe the mechanical problem of the present study.

From the linear conservation of momentum, we have that the total force acting in some part of a material is equal to the rate of the linear momentum of this part. Particularly, for static cases, the linear conservation of momentum provides the Cauchy equilibrium equation.

Then the mechanical problem is focused on finding the displacement field \mathbf{u} , considering that Ω is the volume of a body in the deformed configuration, $\partial\Omega$ is its boundary, \mathbf{b} represents the body forces per volume unit and \mathbf{t} are the surface forces per unit area acting on $\partial\Omega$,

$$\left\{ \begin{array}{ll} \operatorname{div}\boldsymbol{\sigma} + \mathbf{b} = 0, & \text{in } \Omega, \\ \mathbf{u} = \bar{\mathbf{u}}, & \text{on } \partial\Omega^D, \\ \boldsymbol{\sigma}\mathbf{n} = \bar{\mathbf{t}}, & \text{on } \partial\Omega^N. \end{array} \right. \quad (2.11)$$

Here $\bar{\mathbf{u}}$ are the prescribed displacements on the boundary $\partial\Omega^D$ and $\bar{\mathbf{t}}$ is the traction applied on the boundary $\partial\Omega^N$, which has normal vector \mathbf{n} . In order to complete the system of equations, it is need to define the relation between stress and strain through a constitutive model.

2.3 Constitutive equations

The use of constitutive equations is necessary to relate stress and strain. In the continuum mechanics, these equations are models created to describe the physical behavior of materials. These constitutive models represent the stress-strain relationship and are postulated in terms of strain energy functions.

The strain energy function Ψ describes the stored energy in the material due to deformation and it is defined per volume unit in the undeformed configuration. To obtain the stress-strain relationship we differentiate the strain energy function with respect to

the Green-Lagrange strain tensor

$$\mathbf{S} = \frac{\partial \Psi}{\partial \mathbf{E}}. \quad (2.12)$$

A typical example is the St. Venant-Kirchhoff strain energy function which is based on the Green-Lagrange strain tensor and is given by

$$\Psi = \frac{\lambda_l}{2} [\text{tr}(\mathbf{E})]^2 + \mu_l \text{tr}(\mathbf{E}^2), \quad (2.13)$$

which describes a simple hyperelastic material, where μ_l and λ_l are the Lamé coefficients, while $\text{tr}(\cdot)$ represents the trace of a tensor. The strain energy function for the constitutive model that represents the passive behavior of the cardiac tissue is presented below.

2.3.1 Cardiac tissue constitutive model

The cardiac cells are organized in muscle fibers, which are grouped in layers (sheets) of parallel fibers surrounded by collagen. This layered organization of the tissue, presented in Figure 2.1, is characterized by three orthogonal directions: fiber direction \mathbf{f} , sheet direction and orthogonal to the fibers \mathbf{s} and orthogonal to the other two directions \mathbf{n} .

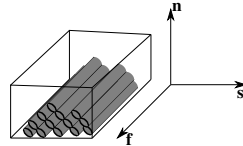


Figure 2.1: Layered organization of the cardiac tissue.

There are different models to describe the cardiac tissue behavior, which can be transversely isotropic (Costa et al., 1996; Humphrey and Yin, 1987; Guccione et al., 1991) or orthotropic (Costa et al., 2001; Holzapfel and Ogden, 2009).

The constitutive model used in the present work was the model proposed by Guccione et al. (1991), which is widely used in the cardiac research community (Wall et al., 2006; Gurev et al., 2010; Wang et al., 2013; Land et al., 2015). The Guccione et al. (1991) strain energy function is defined as

$$\Psi = \frac{C}{2} (e^Q - 1), \quad (2.14)$$

with

$$Q = b_f E_{11}^2 + b_t (E_{22}^2 + E_{33}^2 + E_{23}^2 + E_{32}^2) + b_{fs} (E_{12}^2 + E_{21}^2 + E_{13}^2 + E_{31}^2), \quad (2.15)$$

where C is a stress scale, while b_f , b_t and b_{fs} are related to the stiffness in each direction; E_{ij} denote the Green-Lagrange strain tensor components in the local coordinate system presented in Figure 2.1.

2.3.2 Incompressibility

Incompressible materials are able to be subjected to high loading without presenting volume changes. Many biological tissues, including the cardiac tissue, has an incompressible or nearly incompressible behavior (Humphrey, 2013). In the context of continuum mechanics, incompressibility is mathematically characterized through the constraint

$$J = \det(\mathbf{F}) = 1, \quad (2.16)$$

where \mathbf{F} is the deformation gradient tensor. The strain energy function Ψ can be described (Javier Bonet, 2008) considering the hydrostatic pressure p as

$$\Psi = \Psi_m - p(J - 1), \quad (2.17)$$

where Ψ_m represents the strain energy function for a specific material, as the one presented in (2.14)-(2.15); and p works as a Lagrange multiplier, which can be computed from the equilibrium equation and boundary conditions.

2.3.3 Nearly incompressibility

The mechanical problem solution through the finite element method has a high computational cost when the material is considered incompressible. Therefore, an approach nearly incompressible is more attractive in the numerical point of view, where a material incompressible is treated as compressible allowing only small volume changes. To this end, the strain energy function is divided in an volume-preserved component, named isochoric part, and another component related to the volume change, named volumetric part.

To introduce this approach, it is necessary to introduce a multiplicative decomposition of the deformation gradient tensor:

$$\mathbf{F} = (J^{1/3}\mathbf{I})\bar{\mathbf{F}}, \quad (2.18)$$

where $\bar{\mathbf{F}}$ is associated to the isochoric deformation while $J^{1/3}\mathbf{I}$ is related to the volumetric deformation. Thus, using $\bar{\mathbf{F}}$, we can define the isochoric version of the right Cauchy-Green strain tensor:

$$\bar{\mathbf{C}} = \bar{\mathbf{F}}^T\bar{\mathbf{F}} = J^{-2/3}\mathbf{C}. \quad (2.19)$$

And the isochoric part of the Green-Lagrange strain tensor can be written as

$$\bar{\mathbf{E}} = \frac{1}{2}(\bar{\mathbf{C}} - \mathbf{I}). \quad (2.20)$$

Then we have the following decomposition for the strain energy function

$$\Psi(\bar{\mathbf{E}}) = \Psi_{iso}(\bar{\mathbf{E}}) + \Psi_{vol}(J), \quad (2.21)$$

where its isochoric part is the strain energy function of the material, using the isochoric version of the strain tensor $\Psi_{iso} = \Psi_m(\bar{\mathbf{E}})$. And the volumetric part takes into account the volume change constraint.

2.4 Geometrical models

Several cardiac mechanics studies are focused on left ventricle simulations. It is responsible to pump oxygenated blood from lungs to body and its function can be altered in several cardiac pathologies, such as myocardial infarction, cardiomyopathy and valve diseases. Furthermore, LV simulations can be performed faster than whole organ simulations and several important clinical measures can be extracted from them.

2.4.1 *Simplified geometry of the left ventricle*

The cardiac mechanics benchmark proposed by Land et al. (2015) performed two

experiments considering simplified geometries of the left ventricle, that can be defined using a truncate ellipsoid parametrization, which is shown in Figure 2.2. The endocardium

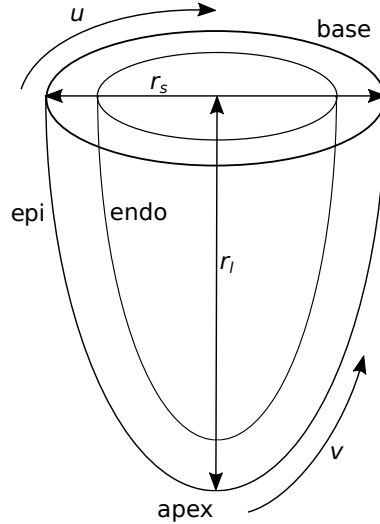


Figure 2.2: Simplified geometry of the left ventricle generated from a family of truncated ellipsoids, where r_s is the short axis, r_l the long axis u and v represent rotation angles used in the parametrization. The epicardium surface is denoted by epi and the endocardium by endo.

and epicardium surfaces are described by the following parametrization

$$\begin{pmatrix} x \\ y \\ z \end{pmatrix} = \begin{pmatrix} r_s \sin u \cos v \\ r_s \sin u \sin v \\ r_l \cos u \end{pmatrix}, \quad (2.22)$$

where r_s is the short axis diameter, r_l the long axis length, u and v represent rotation angles in the circumferential and apex-base directions, respectively. In the benchmark problems, values were defined to construct a LV geometry with base plane in $z = 5$ mm and wall thickness with 3 mm throughout the ventricle. Then, for endocardial surface the parameter values are $r_s = 7$ mm, $r_l = 17$ mm, $u \in [-\pi, -\arccos \frac{5}{17}]$ and $v \in [-\pi, \pi]$. While the epicardial surface has the values $r_s = 10$ mm, $r_l = 20$ mm, $u \in [-\pi, -\arccos \frac{5}{20}]$ and $v \in [-\pi, \pi]$.

The fiber orientation assigned was based on the direction of the derivative computed from the parametrization (2.22), as described in Land et al. (2015). The fiber angles varies from -90° at the epicardium surface to $+90^\circ$ at the endocardium, resulting in the orientation shown in Figure 2.3.

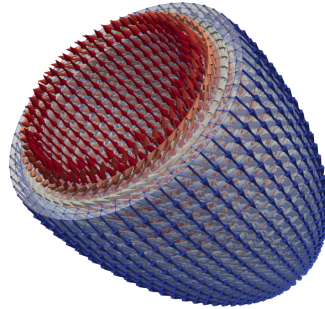


Figure 2.3: Fiber orientation for the simplified LV geometry, varying in the transmural direction from -90° at the epicardium surface to $+90^\circ$ at the endocardium.

2.4.2 Patient specific geometry of the left ventricle

The use of geometries such as that presented before makes the treatment simpler, but it is a severe simplification of the real geometry. Ventricular wall thickness, for instance, is considered constant throughout the domain which is not true in real ventricular shapes. Personalized LV geometries were created using a mesh generator, initially presented by Rodrigues et al. (2015) and that has been recently improved, which is based on wall thickness measurements in LV segments defined by the American Heart Association (AHA) (Cerqueira et al., 2002), as shown in Figure 2.4(a).

The 17 AHA diagram is widely used for visualization of quantitative information, which divides the left ventricle in 17 segments. Different information of the ventricle can be represented in these segments, where the segments 1-6 represents the basal region, while the segments 7-12 are middle sections of the ventricle and the segments 13-16 represents sections close to the apex, aside from the segment 17 for the apex.

These wall thickness measurements are usually extracted via software by a magnetic resonance imaging specialist. From these information 17 blocks are created that represent the geometry, starting from the base blocks until the apex. Blocks are created initially using the respective segment value and then interpolations are done in the longitudinal and circumferential directions, considering neighboring blocks, in order to obtain a continuous and smooth geometry as that presented in Figure 2.4(b).

The inputs for the mesh generator are the 17 wall thickness values together with the short and long axis lengths of the LV. From these potentially patient specific input

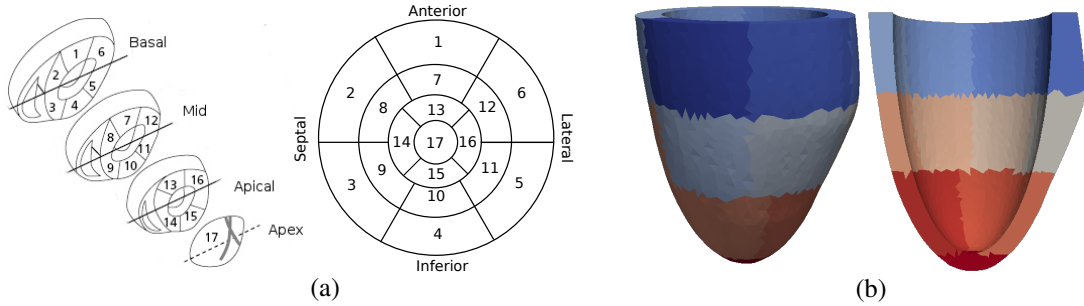


Figure 2.4: (a) 17 AHA segments diagram used in the mesh generator. (b) Example of LV geometry created with the presented mesh generator. Higher values of wall thickness in the basal-lateral segments were chosen, while the short axis was 4.0 cm and the long axis was 6.0 cm.

parameters, an LV geometry is constructed, as illustrated in Figure 2.4(b).

The LV geometry is also modeled using the ellipsoid parametrization (2.22) with some modifications, where the basal plane is $z = 0$ and the component z of all points are positive:

$$\begin{pmatrix} x \\ y \\ z \end{pmatrix} = \begin{pmatrix} a(r) \cos \theta \cos \varphi \\ a(r) \cos \theta \sin \varphi \\ c(r) \sin \theta \end{pmatrix}. \quad (2.23)$$

The values of a and c are computed using $a(r) = a_1 + r(a_2 - a_1)$ and $c(r) = c_1 + r(c_2 - c_1)$ with $0 \leq r \leq 1$. And a_i and c_i ($i = 1, 2$) are coefficients that determine the short and long axis of the ellipsoid, respectively, depending on the block. Each block is limited circumferentially through $\theta_1 \leq \theta \leq \theta_2$ and longitudinally by $\varphi_1 \leq \varphi \leq \varphi_2$, defining a slice of the ventricle that corresponds to an AHA segment.

Figure 2.5 shows the steps of the procedure used for the the generation of the LV geometry. To describe the algorithm, consider the following two parameters n_{circ} and n_{long} which represent the number of points to be created in the circular and in the longitudinal directions, respectively. The algorithm proceeds as follows:

1. Initially, the variables representing the angles θ ranging 0 to 2π and φ ranging from 0 to $\frac{\pi}{2}$ are discretized in n_{circ} and n_{long} points along the circular and longitudinal directions, respectively.
2. For each pair of angles (θ_i, φ_j) the corresponding AHA segment of that point is determined considering the angles. Then, given the segment number, the table of wall thickness measurements is accessed and the appropriate a_1 , a_2 , c_1 and c_2

parameters are computed to create the points which will result in the desired wall thickness property (see Fig. 2.5 (a)).

3. The previous step does not consider the apex, where specific points have to be created for the endocardium and epicardium surfaces.
4. A spline is created for each longitudinal line, from the point at the apex to the point at the base. These splines are added to a list of splines.
5. A smooth surface is created from the list of splines to represent the epicardium surface (see Fig. 2.5 (b)).
6. The steps 1-5 are repeated to create the endocardium surface.
7. Splines are created from the points located at the base (for both endocardium and epicardium). Then a surface is created to represent the basal region (see Fig. 2.5 (c)).
8. Finally, a closed volume is defined with the basal, epicardial and endocardial surfaces which defines the computational geometry of a personalized left ventricle.
9. A finite element mesh is created from the geometry using appropriate algorithms available at the backend software (see Fig. 2.5 (d)).

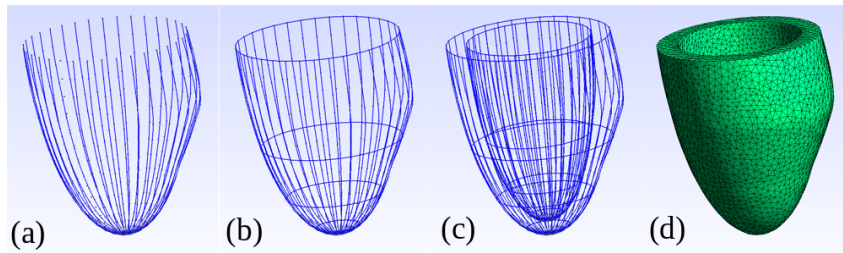


Figure 2.5: Parameterized LV finite element mesh generation.

In this work we considered the computational geometry facilities of Gmsh (Geuzaine and Remacle, 2009) to generate the LV geometries and then its algorithms for the finite element mesh generation.

The Laplace-Dirichlet Rule-Based algorithm proposed in Bayer et al. (2012) was applied to assign fiber orientation in the left ventricular mesh. In this approach the longitudinal fiber direction rotates clockwise by an angle from endocardium (α_{endo}) to

epicardium (α_{epi}) with respect to the circumferential direction. The transverse fiber direction is perpendicular to the longitudinal direction and varies transmurally from endocardium (β_{endo}) to epicardium (β_{epi}), and the sheet normal is orthonormal to the longitudinal and transverse directions.

Figure 2.6 presents an example of fiber orientation assigned to the personalized LV geometry where the values for the helix angles considered were: $\alpha_{endo} = 60^\circ$, $\alpha_{epi} = -60^\circ$, $\beta_{endo} = -65^\circ$ and $\beta_{epi} = 25^\circ$.

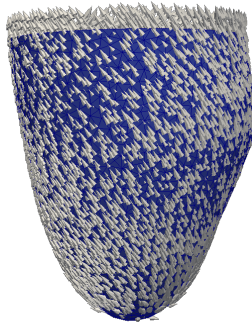


Figure 2.6: Fiber orientation for the personalized LV geometry, with helix angles $\alpha_{endo} = 60^\circ$, $\alpha_{epi} = -60^\circ$, $\beta_{endo} = -65^\circ$ and $\beta_{epi} = 25^\circ$.

2.5 Active stress

The cardiac contraction is developed due to the active force generated in the cellular level. To consider the tissue contraction, this active force must be provided to the mechanical problem. In this work, the active stress approach (Ambrosi and Pezzuto, 2012) was adopted to perform this coupling, which additively splits the stress tensor in two parts: passive and active. The passive part is intrinsically related to the constitutive model for the material, while the active part take into account the contribution of the active force generated by cardiac myocytes.

The second Piola-Kirchhoff tensor can be defined as a sum of the passive stress and the active stress:

$$\mathbf{S} = \mathbf{S}_p + \mathbf{S}_a, \quad (2.24)$$

where the passive stress \mathbf{S}_p is derived from the Guccione strain energy function presented in equation (2.14), and the active stress \mathbf{S}_a describes the kinetics for the cellular contraction. The active stress is considered anisotropic and it is applied in fiber direction

of the cardiac tissue, that is

$$\mathbf{S}_a = T_{ref} T_a \mathbf{f}_0 \otimes \mathbf{f}_0, \quad (2.25)$$

where T_a is the normalized active stress generated by a cellular electro-mechanical model (Rice et al., 2008), T_{ref} is reference value for stress and \mathbf{f}_0 is the unit vector that defines the fiber direction in the undeformed configuration.

2.5.1 Kerckhoffs et al. (2003) active stress model

The active stress was described through an arrangement of a contractile element in series with an elastic element, as presented in Kerckhoffs et al. (2003). It is written in terms of the elapsed time since depolarization (t_a), the sarcomere length (l_s) and a contractile element length (l_c):

$$T_a = \frac{l_s}{l_{s0}} f_{iso}(l_c) f_{twitch}(t_a, l_s) E_a (l_s - l_c), \quad (2.26)$$

where l_{s0} is the reference length of the sarcomere and E_a is the elastic element stiffness.

The function f_{iso} describes the isometric stress in terms of l_c :

$$f_{iso}(l_c) = \begin{cases} T_0 \tanh^2[a_l(l_c - l_{c0})] & l_c \geq l_{c0} \\ 0 & l_c < l_{c0} \end{cases} \quad (2.27)$$

where T_0 is the reference active stress, a_l controls the steepness of the stress-length curve, and l_{c0} is the contractile element length when active stress is zero.

The function f_{twitch} describes the myofiber stress dependence on t_a and l_s :

$$f_{twitch}(t_a, l_s) = \begin{cases} 0 & t_a < 0 \\ \tanh^2\left(\frac{t_a}{\tau_r}\right) \tanh^2\left(\frac{t_{max} - t_a}{\tau_d}\right) & 0 \leq t_a \leq t_{max} \\ 0 & t_a > t_{max} \end{cases} \quad (2.28)$$

where $t_{max} = b(l_s - l_d)$ is the twitch duration, with b describing the increase in twitch duration, l_d is the sarcomere length when twitch duration is zero, while τ_r and τ_d are the twitch rise and decay time constants, respectively.

Finally, the contractile element length varies with time following a first order differential equation:

$$\frac{dl_c}{dt} = v_0 (E_a (l_s - l_c) - 1), \quad (2.29)$$

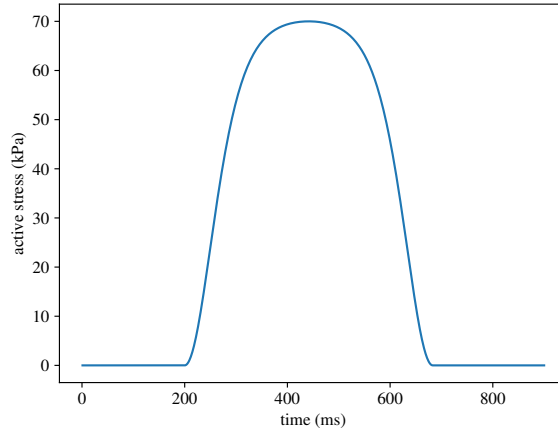


Figure 2.7: Active stress curve used to represent the ventricle contraction.

where v_0 is the unloaded shortening velocity. Table 2.1 shows the parameters values used to generate a typical active stress as the one in Figure 2.7.

Table 2.1: Parameter values for the active stress model.

a_l	l_{c0}	T_0	E_a	v_0	l_{s0}	τ_r	τ_d	b	l_d
μm^{-1}	μm	kPa	μm^{-1}	$\mu m s^{-1}$	μm	s	s	$s \mu m^{-1}$	μm
2.0	1.5	180	20	7.5	1.9	0.075	0.075	0.21	-0.4

2.6 Circulatory model

The endocardium surface is subjected to the blood pressure which flows in and out of the ventricular cavity. To represent the ventricle function during the cardiac cycle, a time varying pressure boundary condition is applied to the endocardium surface. This pressure is described by a lumped parameter model, which represents the circulatory system through an electric circuit scheme. The electrical charge represents the blood volume, potential difference correspond to pressure and currents to flow rates. A blood vessel or group of vessels can be represented by a combination of resistors, capacitors and inductors. The blood vessel resistance is modeled by resistors, which depends on the blood viscosity and the vessel diameter. Capacitors are used to model compliance, describing the ability of blood accumulation and release due to elastic deformation. The blood inertia

is represented by coils and valves can be modeled using diodes. For instance, Figure 2.8 presents the circuit for the circulatory model used in this work, which was presented by Shavik et al. (2017).

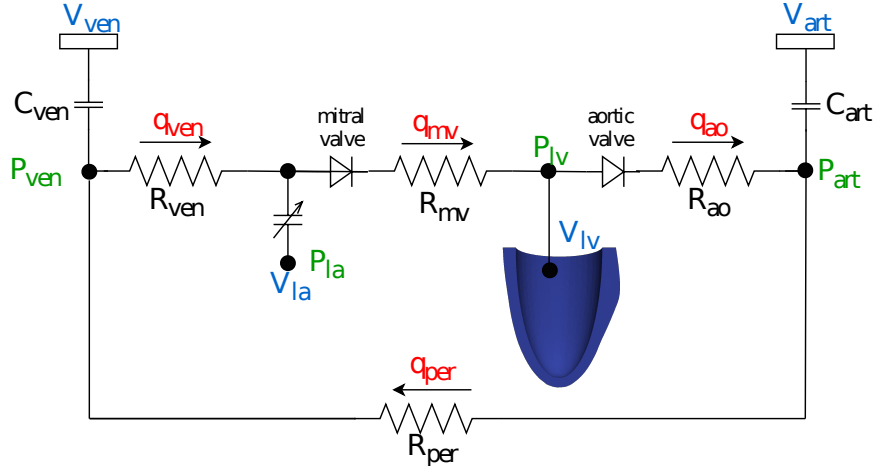


Figure 2.8: Circuit scheme for the lumped parameter model adopted in this work, in order to reproduce the time varying pressure in the left ventricle cavity.

The flow through a compartment (e.g. venous system and mitral valve) is proportional to the following pressure difference

$$q = \frac{P_{in} - P_{out}}{R}, \quad (2.30)$$

where R is the resistance encountered by the blood. The pressure in a vessel is related to the volume difference via the compliance

$$P_i = \frac{V_i - V_{i,0}}{C_i}, \quad (2.31)$$

where V_i is the volume in the compartment, $V_{i,0}$ the resting volume and C_i the vessel compliance constant.

An ideal valve stops the flow in one direction and allows the blood to flow in the other direction, opposing a resistance R to the flow, once the pressure difference is higher than a certain critical pressure P^* . Thus, the flow rate in the valves can be modeled as follows:

$$q_{valve} = \begin{cases} 0 & \text{if } P < P^* \\ P/R & \text{if } P \geq P^* \end{cases}. \quad (2.32)$$

The Kirchhoff's law for currents and potential difference can also be applied here, where the sum of flow rates entering any junction is equal to the sum of flow rates leaving that junction. The sum of all pressure difference around a loop is equal to zero. Using these assumptions, the circuit can be described by a system of ordinary differential equations of the following type

$$\frac{dV_i}{dt} = q_{in} - q_{out}. \quad (2.33)$$

The lumped model used in the present work was described in Shavik et al. (2017) and its circuit scheme is presented in Figure 2.8. The model considers the blood volumes in left atrium (V_{LA}), left ventricle (V_{LV}), venous (V_{ven}) and arterial (V_{art}) systems. Besides, the mitral and aortic valves are considered as diodes, while the peripheral system is modeled using a resistor.

The arterial and venous pressure are obtained using the compliance relation (2.31):

$$P_{art} = \frac{V_{art} - V_{art,0}}{C_{art}}, \quad (2.34)$$

$$P_{ven} = \frac{V_{ven} - V_{ven,0}}{C_{ven}}, \quad (2.35)$$

while the pressure in the left atrium is given by a time varying elastance function and the pressure in the left ventricle is estimated through the coupling with the FEM solver described by van Nierop (2007).

The flow rate through the aortic and mitral valves are found using equation (2.32):

$$q_{ao} = \begin{cases} 0 & \text{if } P_{LV} < P_{art} \\ \frac{P_{LV} - P_{art}}{R_{ao}} & \text{if } P_{LV} \geq P_{art} \end{cases}, \quad (2.36)$$

$$q_{mv} = \begin{cases} 0 & \text{if } P_{LA} < P_{LV} \\ \frac{P_{LA} - P_{LV}}{R_{mv}} & \text{if } P_{LA} \geq P_{LV} \end{cases}. \quad (2.37)$$

And the flow rates for peripheral and venous systems were described by the relation (2.30):

$$q_{per} = \frac{P_{art} - P_{ven}}{R_{per}}, \quad (2.38)$$

$$q_{ven} = \frac{P_{ven} - P_{LA}}{R_{ven}}. \quad (2.39)$$

Finally, using equation (2.33), the circuit can be described by

$$\frac{dV_{LA}}{dt} = q_{ven} - q_{mv}, \quad (2.40)$$

$$\frac{dV_{LV}}{dt} = q_{mv} - q_{ao}, \quad (2.41)$$

$$\frac{dV_{art}}{dt} = q_{ao} - q_{per}, \quad (2.42)$$

$$\frac{dV_{ven}}{dt} = q_{per} - q_{ven}. \quad (2.43)$$

The left atrium contraction was described by a time varying elastance, which relates the atrial pressure P_{LA} to its volume V_{LA} using the equation (Shavik et al., 2017)

$$P_{LA}(t) = e(t)P_{es,LA}(V_{LA}) + (1 - e(t))P_{ed,LA}(V_{LA}), \quad (2.44)$$

with

$$P_{es,LA}(V_{LA}) = E_{es,LA}(V_{LA} - V_{0,LA}), \quad (2.45)$$

$$P_{ed,LA}(V_{LA}) = A_{LA}(e^{B_{LA}(V_{LA} - V_{0,LA})} - 1), \quad (2.46)$$

where $E_{es,LA}$ is the end-systolic elastance, $V_{0,LA}$ is the volume axis intercept of the end-systolic pressure volume relation (ESPVR), while A_{LA} and B_{LA} are parameters of the end-diastolic pressure volume relation (EDPVR). The driving function $e(t)$ is written in terms of the point of maximal chamber elastance T_{max} , the time constant of relaxation τ and the time t during the cardiac cycle:

$$e(t) = \begin{cases} \frac{1}{2}(\sin[(\frac{\pi}{T_{max}})t - \frac{\pi}{2}] + 1) & \text{if } 0 < t \leq \frac{3}{2}T_{max} \\ \frac{1}{2}e^{-(t - \frac{3}{2}T_{max})/\tau} & \text{if } t > \frac{3}{2}T_{max} \end{cases}. \quad (2.47)$$

Table 2.2 presents the parameters unit and value used for the circulatory model.

Table 2.2: Parameters for the circulatory model.

Symbol	Model input	Unit	Value
R_{ao}	Aortic valve resistance	$Pa \cdot ms \cdot ml^{-1}$	3850
R_{per}	Peripheral resistance	$Pa \cdot ms \cdot ml^{-1}$	140000
R_{ven}	Venous resistance	$Pa \cdot ms \cdot ml^{-1}$	1400
R_{mv}	Mitral valve resistance	$Pa \cdot ms \cdot ml^{-1}$	1750
C_{art}	Aortic compliance	$ml \cdot Pa^{-1}$	0.014
C_{ven}	Venous compliance	$ml \cdot Pa^{-1}$	0.3
$V_{art,0}$	Resting volume for artery	ml	580
$V_{ven,0}$	Resting volume for vein	ml	3300
$E_{es,LA}$	End-systolic elastance	$Pa \cdot ml^{-1}$	60
$V_{0,LA}$	Volume axis intercept	ml	10
A_{LA}	Scaling factor for EDPVR	Pa	58.67
B_{LA}	Exponent for EDPVR	ml^{-1}	0.049
T_{max}	Time to end-systole	ms	200
τ	Time constant of relaxation	ms	25

2.6.1 LV pressure estimation

The solution of the lumped parameter model provides the blood volume in the ventricular cavity, but this volume can not be prescribed as a boundary condition in the cardiac mechanics solver. Therefore, given a volume V_{LV} obtained from the lumped parameter model, a pressure value is estimated in order to be applied in the endocardium surface as an external loading and obtain a ventricular volume close to V_{LV} via cardiac mechanics solver. The approach presented by van Nierop (2007) was used in the present work to estimate the pressure, which is based on a method that minimizes the difference between the cavity volumes found through the FEM simulation of the cardiac mechanics and the lumped parameter model.

Algorithm 1 presents the approach performed to obtain the pressure boundary condition for each time step that results in a ventricular cavity volume close to the value given by the lumped parameter model.

Algorithm 1: Algorithm to couple circulatory model to cardiac mechanics.

```

1 foreach time step t do
2    $i = 0$ 
3   Compute the first estimation for pressure  $P_{LV,t}^i$ , using Adams-Bashforth scheme
4   do
5     Solve cardiac mechanics model and determine  $V_{LV,t,FEM}^i$ , using  $P_{LV,t}^i$ 
6     Solve lumped parameter model and determine  $V_{LV,t,LP}^i$ 
7     Compute new pressure estimation:
8     
$$C = \frac{P_{LV,n+1}^i - P_{LV,n+1}^{i-1}}{V_{LV,n+1,FEM}^i - V_{LV,n+1,FEM}^{i-1}}$$

9      $r_{est} = V_{LV,n+1,FEM}^i - V_{LV,n+1,LP}^i$ 
10     $P_{LV,n+1}^{i+1} = P_{LV,n+1}^i - C \cdot r_{est}$ 
11    
$$\delta = \left| \frac{V_{LV,t,FEM}^i - V_{LV,t,LP}^i}{V_{LV,t,LP}^i} \right|$$

12     $i = i + 1$ 
13    while  $\delta > V_{tol}$ 
14 end foreach

```

First, a value for pressure is estimated using a fourth order Adams-Bashforth (Holmes, 2011) scheme:

$$P_{n+1} = P_n + \frac{\Delta t}{24}(55f_n - 59f_{n-1} + 37f_{n-2} - 9f_{n-3}), \quad (2.48)$$

with $f_n = \frac{P_n - P_{n-1}}{\Delta t}$ is the temporal derivative of the pressure for time step n (Kerckhoffs et al., 2007). In the first steps it is not possible to use this scheme, then the pressure was estimated using

$$P_{n+1} = P_n + \frac{\Delta P}{\Delta V} \cdot q \Delta t, \quad (2.49)$$

with $P_0 = 0$, $\Delta P = 1.6$ kPa, $\Delta V = 50$ ml, $q = 0.25$ ml/ms.

The estimated pressure is used in the FEM solver as boundary condition for the cardiac mechanics problem $P_{LV,t}^i$, resulting in ventricular cavity volume $V_{LV,t,FEM}^i$. Then, a volume $V_{LV,t,LP}^i$ is computed solving the lumped parameter model using the mid-point

method. The following equations shows this method applied to (2.43):

$$\begin{aligned}
 q_{per,n+\frac{1}{2}}^i &= \frac{1}{2R_{per}}(P_{art,n+1}^{i-1} + P_{art,n} - P_{ven,n+1}^{i-1} - P_{ven,n}), \\
 q_{ven,n+\frac{1}{2}}^i &= \frac{1}{2R_{ven}}(P_{ven,n+1}^{i-1} + P_{ven,n} - P_{LA,n+1}^{i-1} - P_{LA,n}), \\
 V_{ven,n+1}^i &= V_{ven,n} + \Delta t \cdot (q_{per,n+\frac{1}{2}}^i - q_{ven,n+\frac{1}{2}}^i).
 \end{aligned} \tag{2.50}$$

The volumes $V_{LV,t,LP}^i$ and $V_{LV,t,FEM}^i$ are then used to compute a new estimation for pressure, where the last estimation is corrected using the compliance C and the residual r_{est} , which should become smaller every new estimation. The algorithm stops when the relative error between the volumes is lower than a specified tolerance V_{tol} .

2.7 Numerical solution of the mechanical problem

The heart tissue is considered anisotropic, nonlinear and nearly incompressible, which are properties that increase the computational cost of the simulations. In spite of the increasing number of studies in cardiac mechanics, there are relatively few works focusing on the efficient solution of the model equations. Land et al. (2012) proposed a modified Newton method and a strain prediction technique to reduce the number of Newton iterations needed, while Sundnes et al. (2014) proposed an efficient linearization of coupled passive and active mechanics problems, and Hadjicharalambous et al. (2014) presented a weakly penalized formulation for the problem in order to provide an efficient treatment of incompressibility.

The numerical performance of the simulations is an important feature for research, and in particular for clinical applications of the models. Coupled electro-mechanics simulations typically requires high spatial and temporal resolution, and the resulting computational problem is challenging to solve within the time constraints posed by clinical applications. Within this context iterative solvers become mandatory due to the large problem size, and the use of preconditioners is essential for improving their convergence. Algebraic Multigrid (AMG) methods are increasingly popular in computational science, due to their robustness when solving large unstructured sparse linear systems of equations. They have been used in a wide range of applications, ranging from computer graphics and animations (Tamstorf et al., 2015) to fluid mechanics (Stüben, 2001) and elasticity (Baker et al., 2009). In

the context of cardiac electrophysiology simulations these methods have shown a good performance (dos Santos et al., 2004; Plank et al., 2007), whereas for elasticity problems variants of the classical AMG preconditioner have been studied in (Baker et al., 2016) in terms of parallel scalability.

The numerical treatment of incompressible or nearly incompressible materials within the finite element method (FEM) framework can cause difficulties such as the well known volumetric locking of the solution. The simplest approach for enforcing incompressibility is the use of a penalty formulation with a large value for the bulk modulus, in order to prevent volumetric changes. However, it is well known that this approach leads to a highly ill-conditioned problem, which markedly deteriorates the performance of iterative solvers. Many numerical approaches within the FEM literature have been proposed to prevent these problems, which include mixed formulations (Brezzi and Fortin, 1991) and the usage of underintegrated elements and the B-bar/F-bar methods (Elguedj et al., 2008). An alternative approach for nearly incompressible materials is the Augmented Lagrangian (ALG) formulation (Simo and Taylor, 1991; Weiss et al., 1996), which is presented here for cardiac mechanics. The ALG formulation for nearly incompressible materials allows to control the volumetric changes to a desired tolerance, and also to reduce the ill-conditioning of the resulting linear systems.

2.7.1 Variational formulation

The finite element method was used to obtain the cardiac tissue deformation, described by equation (2.11). Therefore, it is necessary to find the variational formulation for this problem. A variational formulation based on the existence of an energy functional for the stresses and loads is presented. This type of formulation is useful for the construction of robust algorithms, which are based in optimization techniques (Holzapfel, 2000; Javier Bonet, 2008).

The total potential energy of the system Π is given by the sum of the internal Π_{int}

and external Π_{ext} energies, that is

$$\Pi(\mathbf{u}) = \Pi_{int}(\mathbf{u}) + \Pi_{ext}(\mathbf{u}), \quad (2.51)$$

$$\Pi_{int}(\mathbf{u}) = \int_{\Omega} \Psi(\mathbf{F}(\mathbf{u})) dV, \quad (2.52)$$

$$\Pi_{ext}(\mathbf{u}) = - \int_{\Omega} \mathbf{b} \cdot \mathbf{u} dV - \int_{\partial\Omega} \mathbf{t} \cdot \mathbf{u} dS, \quad (2.53)$$

where Ψ is the strain energy function, \mathbf{u} is the displacement field, \mathbf{b} are the body forces and \mathbf{t} is the traction on the surface.

The equilibrium state (deformed configuration) is obtained by finding the stationary position of the total potential energy, which occurs when the directional derivative with respect to displacements \mathbf{u} is zero in an arbitrary direction $\delta\mathbf{u}$. Then, the stationary position of Π is found by equating its first variation $\delta\Pi$ to zero

$$\delta\Pi(\mathbf{u}, \delta\mathbf{u}) = D_{\delta\mathbf{u}}\Pi(\mathbf{u}) = \left. \frac{d}{d\epsilon} \Pi(\mathbf{u} + \epsilon\delta\mathbf{u}) \right|_{\epsilon=0} = 0, \quad (2.54)$$

where $D_{\delta\mathbf{u}}$ represents the directional derivative with respect to displacements. The stationary position of this functional results in a variational formulation for the problem (2.11), which is equivalent to the principle of the virtual work (Javier Bonet, 2008) and it can be used by the finite element method to find the displacement field.

In order to consider incompressible materials, it is necessary to add a constraint in this formulation through a Lagrange multiplier (Holzapfel, 2000). Thus, the resulting problem has two unknowns and its solution becomes more difficult. However, there are numerical alternatives to treat the material incompressibility, such as the Penalty method, where the problem remains with only the displacement field as unknown.

2.7.2 *Penalty method*

The penalty method considers an incompressible material as nearly incompressible, allowing small volume changes (Javier Bonet, 2008; Holzapfel, 2000).

As presented in section 2.3.3, the strain energy function can be decomposed as $\Psi(\mathbf{C}) = \Psi_{iso}(\overline{\mathbf{C}}) + \Psi_{vol}(J)$, where the volumetric component must be defined in such a manner that if $J = 1$ and $\overline{\mathbf{C}} = \mathbf{I}$, then $\Psi_{iso} = \Psi_{vol} = 0$, ensuring an undeformed configuration without stress. Thus, $\Psi_{vol}(J)$ is characterized by the penalty parameter κ and a penalty

function $U(J)$:

$$\Psi_{vol}(J) = \kappa U(J), \quad (2.55)$$

where the penalty function $U(J) = \frac{1}{2}(J - 1)^2$ was adopted in this work. The penalty method treat the material as weakly compressible with a high value of κ . The material would be incompressible when the value of κ goes to infinity, but it is not possible numerically, then this approach always allows the material to have a small volume change (Holzapfel, 2000).

In a similar manner, we can split the second Piola-Kirchhoff tensor into an isochoric and volumetric parts:

$$\mathbf{S} = \mathbf{S}_{iso} + \mathbf{S}_{vol}, \quad (2.56)$$

resulting in

$$\mathbf{S} = 2 \frac{\partial \Psi_{iso}(\bar{\mathbf{C}})}{\partial \mathbf{C}} + Jp\mathbf{C}^{-1}, \quad (2.57)$$

where the hydrostatic pressure p is defined as

$$p = \frac{d\Psi_{vol}}{dJ} = \kappa \frac{dU(J)}{dJ} = \kappa(J - 1). \quad (2.58)$$

Then, the energy functional for the penalty method Π_p can be defined as

$$\Pi_p(\mathbf{u}) = \int_{\Omega} [\Psi_{vol}(J) + \Psi_{iso}(\bar{\mathbf{C}})] dV + \Pi^{\text{ext}}(\mathbf{u}), \quad (2.59)$$

where the functional is written only in terms of the displacement field and the material can be considered nearly incompressible through the penalty parameter κ , present in the function $\Psi_{vol}(J)$. This parameter is defined by the user and obtained by numerical experiments with the problem to be solved. In order to ensure a small volumetric variation, high values of κ are used. However, when the value of this parameter is increased, the conditioning number of the stiffness matrix from the finite element method also increases significantly (Holzapfel, 2000), which causes a poor performance of iterative solvers used. Another problem of this formulation is the locking phenomenon, a numerical problem which occurs when the value of κ is too high and the solution does not converge to the expected value (Hughes, 2012).

2.7.3 *Simo-Taylor-Pister formulation*

An alternative to the penalty method is the mixed three field formulation proposed by Simo-Taylor-Pister (STP) (Simo and Taylor, 1991; Simo et al., 1985), which is able to avoid the locking phenomenon. This formulation is robust to treat incompressibility and it has been used with success in biomechanics (Gasser et al., 2006).

As in the penalty method, the STP formulation uses a decomposed strain energy function $\Psi(\mathbf{C}) = \Psi_{iso}(\overline{\mathbf{C}}) + \Psi_{vol}(J)$. Furthermore, this formulation considers three independent variables: displacements \mathbf{u} , pressure p and dilatation \tilde{J} , resulting in the following energy functional:

$$\Pi_{STP}(\mathbf{u}, p, \tilde{J}) = \int_{\Omega_0} \left[\Psi_{iso}(\overline{\mathbf{E}}) + \Psi_{vol}(\tilde{J}) + p(J(\mathbf{u}) - \tilde{J}) \right] dV + \Pi_{ext}(\mathbf{u}), \quad (2.60)$$

The variable \tilde{J} must satisfy the constraint $J = \tilde{J}$ in a mean sense, where $J = \det(\mathbf{F})$ is imposed through the Lagrange multiplier p . Although this formulation has three unknowns, it can be rewritten in such a manner that only displacement will be an unknown. As described in Javier Bonet (2008), when the finite element discretization uses constant interpolation functions for p and \tilde{J} , these variables can be computed at the element level as

$$\tilde{J} = \frac{1}{V} \int_V J dV = \frac{v}{V}, \quad (2.61)$$

$$p = \left. \frac{dU}{d\tilde{J}} \right|_{\tilde{J}=v/V}. \quad (2.62)$$

It is important to emphasize that the parameter κ remains in the present formulation and, in general, it is still necessary a high value for this parameter in order to obtain small volume changes in the solution. However, Weiss et al. (1996) and Gasser et al. (2006) showed experiments about the robustness and applicability of this method in the context of elasticity and biomechanics.

2.7.4 *Augmented Lagrangian formulation*

The mixed three field formulation has been shown to be well suited for nearly incompressible materials (Gasser et al., 2006), but still relies on a large value of κ to control the volumetric changes, which in turn increases the ill-conditioning of the resulting

stiffness matrix. In this context iterative solvers may have a poor performance when solving these systems. The present work used the Augmented Lagrangian (ALG) approach to treat near-incompressibility for cardiac mechanics problems. This formulation was introduced in finite elasticity by Glowinski and Le Tallec (1982, 1984) and some works have applied this formulation to solve biomechanics problems such as in Weiss et al. (1996), which applied this method to evaluate the stress in a human knee ligament.

The energy functional for the ALG formulation is given by

$$\Pi_{ALG}(\mathbf{u}, p, \tilde{J}, \mu) = \int_{\Omega_0} \left[\Psi_{\text{iso}}(\bar{\mathbf{C}}) + \Psi_{\text{vol}}(\tilde{J}) + p(J - \tilde{J}) + \mu(\tilde{J} - 1) \right] dV + \Pi_{\text{ext}}, \quad (2.63)$$

where we remark that although it considers four variables, p and \tilde{J} are calculated at the element level and the new Lagrange multiplier μ is iteratively computed as described next.

The ALG formulation enforces the element-wise near-incompressibility condition through the addition of a term in the functional with a Lagrange multiplier μ for each finite element. This new Lagrange multiplier is computed by an Uzawa-like algorithm (Brezzi and Fortin, 1991; Glowinski and Le Tallec, 1989) given by:

$$\mu_{k+1} = \mu_k + \xi^c (\det \mathbf{F} - 1), \quad (2.64)$$

where ξ^c is a constant weight. When the mixed three-field formulation is used, the constraint $\det(\mathbf{F}) = 1$ is imposed in a mean sense, because the constraint is considered on variable \tilde{J} instead of $J = \det(\mathbf{F})$. With the ALG approach the penalty parameter κ that controls the volumetric term Ψ_{vol} can be reduced, which in turn results in a less ill-conditioned stiffness matrix.

Algorithm 2 shows how the ALG formulation enforces the constraint $\tilde{J} = 1$ within each finite element. First, the Lagrange multiplier is initialized with zero and after solving the nonlinear problem for the current load step, the volume change constraint is verified for each element. Then, the Lagrange multiplier is augmented for the elements that do not satisfy the criterion. The defined tolerance tol specifies the range of volumetric changes allowed. The next load increment is only performed when all elements satisfy the criterion.

In this way it is possible to control element-wise volume changes to any desired tolerance.

Algorithm 2: Augmented Lagrangian algorithm

```

1 Set Lagrange multiplier  $\mu_0 = 0$ 
2 while full load not reached yet do
3   Apply load increment
4    $k = 0$ 
5   do
6     Use Newton iteration to solve the nonlinear problem (2.63)
7     foreach finite element  $e$  that do not satisfy  $|\tilde{J} - 1| < tol$  do
8       Update Lagrange multiplier as  $\mu_{k+1}^e = \mu_k^e + \xi^e(\tilde{J} - 1)$ 
9     end foreach
10     $k = k + 1$ 
11    while there are elements  $e$  such that  $|\tilde{J} - 1| > tol$ 
12 end while

```

2.7.5 Finite element method

Computing the first variation of the functional energy, it is possible to find the stationary position, which can be discretized using the finite element method. The domain is divided in hexahedra or tetrahedra with the displacement field being approximated by piece-wise linear functions while the pressure p and dilatation \tilde{J} are approximated through constant piecewise functions. This finite element approximation is named $Q1 - Q0 - Q0$.

Constant elements were chosen for pressure and dilatation in order to compute this variables at the element level, as presented in section 2.7.3. This procedure enables to eliminate them from the problem, resulting in a system where the unknown is only the displacement field.

2.7.6 Newton's method

The FEM discretization results in a system of nonlinear equations, which can be solved using the Newton's method with the following iteration:

$$\mathbf{K}(\mathbf{u}^i)\Delta\mathbf{u} = \mathbf{T}^{ext} - \mathbf{T}^{int}(\mathbf{u}^i) \quad (2.65)$$

$$\mathbf{u}^{i+1} = \mathbf{u}^i + \Delta\mathbf{u}, \quad (2.66)$$

where \mathbf{K} is the global stiffness matrix, \mathbf{T}^{ext} is the vector of external loads and $\mathbf{T}^{int}(\mathbf{u}^i)$ the vector of internal nodal forces. The external loads are applied through a series of load increments with fixed length, which are controlled by the load parameter λ such that $\mathbf{T}^{ext} = \lambda\mathbf{T}$, being \mathbf{T} the total external load.

The linear systems involved in the iterations of the Newton's method were solved using the preconditioned Generalized Minimal Residual method (GMRES) (Saad, 2003).

2.7.7 *Preconditioners*

As mentioned, the linear systems that need to be solved for each step of the Newton method are ill-conditioned, which implies in a poor convergence for the iterative solvers used to this end. A manner to improve the convergence of this methods is the use of preconditioners, which modify the original linear system to create a better conditioned system.

A preconditioning approach that can be applied in an linear system of the form

$$\mathbf{K}\mathbf{u} = \mathbf{f}, \quad (2.67)$$

is the pre-multiplication by a matrix \mathbf{M}^{-1} as

$$\mathbf{M}^{-1}\mathbf{K}\mathbf{u} = \mathbf{M}^{-1}\mathbf{f}. \quad (2.68)$$

The preconditioner \mathbf{M}^{-1} needs to be efficient, the matrix has to be constructed with a low computational cost and the product $\mathbf{M}^{-1}\mathbf{K}$ must have a condition number less than \mathbf{K} .

2.7.8 *Multigrid method*

Before presenting the the preconditioner used in this work, a brief overview of the multigrid method is presented. The multigrid method was developed to solve linear systems resultant from the discretization of boundary value problems (Briggs et al., 2000). Some iterative methods such as Jacobi, Gauss-Seidel and Successive over-relaxation (SOR) methods can reduce the high frequency errors, but the low frequency errors remains present in the solution. This problem can be circumvented when the initial guess for the

iterative method is obtained from iterations in coarser discretizations.

Consider the residual as a measurement of the accuracy solution:

$$\mathbf{r} = \mathbf{f} - \mathbf{K}\bar{\mathbf{u}}, \quad (2.69)$$

where $\bar{\mathbf{u}}$ represent the approximate solution obtained by an iterative method. Considering that the error with respect to the exact solution \mathbf{u} is $\mathbf{e} = \mathbf{u} - \bar{\mathbf{u}}$, the following relation between error and residual can be written:

$$\mathbf{K}\mathbf{e} = \mathbf{r}. \quad (2.70)$$

Then it is possible to correct the approximated solution using the value for the error obtained solving (2.70):

$$\mathbf{u} = \bar{\mathbf{u}} + \mathbf{e}, \quad (2.71)$$

which results in a better approximation for the linear system solution.

Combining this information with methods of simple implementation the multigrid method was created, which uses stationary iterative methods, such as the relaxation methods in order to smooth the solution, removing high frequency errors. Then, the solution is transferred to a coarser grid, which introduce more oscillations in the error, allowing to use relaxation methods again. The coarsening process continues until it is possible to compute the error by solving (2.70) through a direct method. Finally, the solution \mathbf{u} is corrected using the computed error.

Due to the use of different grids in the multigrid method, it is necessary to transfer information between them. The information transfer from a more refined grid to a coarser one is done through the restriction operator \mathbf{R} , which is usually based on a weighted average using the values of a point and its neighbors. In order to transfer information from a coarser grid to a more refined one, the interpolation operator \mathbf{P} is used, where a linear interpolation already works effectively (Briggs et al., 2000).

The multigrid method can be applied using different schemes, such as V-cycle, W-cycle and μ -cycle, which depend on the sequence of steps and refinements used. The Figure 2.9 presents an example of the V-cycle scheme using three different grid levels.

In this example the multigrid performs the following steps:

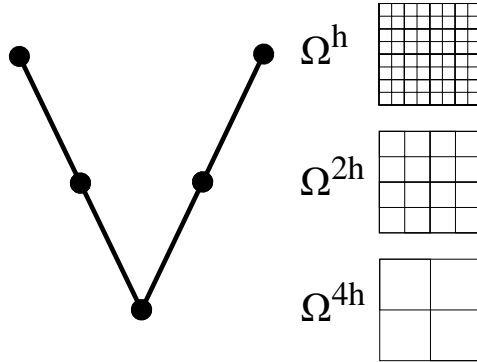


Figure 2.9: V-cycle scheme for the multigrid method.

- Perform ν_1 iterations using the stationary method to smooth the solution of $\mathbf{K}^h \mathbf{u}^h = \mathbf{f}^h$, with initial guess $\bar{\mathbf{u}}^h$ in the grid Ω^h
- Compute and restrict the residual $\mathbf{r}^{2h} = \mathbf{Rr}^h$
 - Perform ν_1 iterations using the stationary method to smooth the solution of $\mathbf{K}^{2h} \mathbf{e}^{2h} = \mathbf{r}^{2h}$, with initial guess $\mathbf{e}^{2h} = \mathbf{0}$ in the grid Ω^{2h}
 - Compute and restrict the residual $\mathbf{r}^{4h} = \mathbf{Rr}^{2h}$
 - * Compute the error $\mathbf{K}^{4h} \mathbf{e}^{4h} = \mathbf{r}^{4h}$, using a direct method
 - Interpolate the error $\mathbf{e}^{2h} = \mathbf{Pe}^{4h}$ and correct the solution $\bar{\mathbf{e}}^{2h} = \bar{\mathbf{e}}^{2h} + \mathbf{e}^{2h}$
 - Perform ν_2 iterations using the stationary method to smooth the solution of $\mathbf{K}^{2h} \mathbf{e}^{2h} = \mathbf{r}^{2h}$, with initial guess $\bar{\mathbf{e}}^{2h}$ in the grid Ω^{2h}
- Interpolate the error $\mathbf{e}^h = \mathbf{Pe}^{2h}$ and correct the solution $\bar{\mathbf{u}}^h = \bar{\mathbf{u}}^h + \mathbf{e}^h$
- Perform ν_2 iterations using a stationary method to smooth the solution of $\mathbf{K}^h \mathbf{u}^h = \mathbf{f}^h$, with initial guess $\bar{\mathbf{u}}^h$ in the grid Ω^h

The described method is known as geometric multigrid (GMG), where different grids were created to be used in different levels. This method works very well in structured meshes, where it is easy to define information transference between levels. However, when unstructured meshes are used it is difficult to apply the geometric multigrid. In order to circumvent this problem, the algebraic multigrid (AMG) was developed (Briggs et al., 2000), therefore, the method is not limited to solve linear systems resultant from a domain discretization, enabling its use in other types of systems.

The algebraic multigrid has the same steps of the geometric, where it is necessary to define grids with different resolutions in order to smooth the error. Furthermore, it is necessary to define the transfer operators between grids. The most refined grid is defined by a graph connecting the components of the matrix that represents the linear system (Briggs et al., 2000). An edge between vertices i and j is created in the graph if $a_{ij} \neq 0$ or $a_{ji} \neq 0$.

After defining the finest grid, it is necessary to define the concept of smoothing algebraically and then a scheme of relaxation. The coarser grids are constructed from the finest grid using the defined smoothing sense. These grids are subsets of unknowns from the original system, based on the dependence among them. Finally, the restriction and interpolation operators are defined to transfer information between grids.

2.7.9 Algebraic multigrid preconditioners for elasticity problems

When the multigrid method is used as a preconditioner, it is applied during some iterations using the original matrix of the system and the residual. Then, the solution from the multigrid is used as the preconditioned residual $\mathbf{z} = \mathbf{M}^{-1}\mathbf{r}$, used in iterative methods such as GMRES and Conjugate Gradient (CG).

In order to improve the convergence of iterative solvers we applied an Algebraic Multigrid (AMG) preconditioner (Briggs et al., 2000; Stüben, 2001) for the solution of the linear systems. When algebraic multigrid methods are applied to systems of PDEs, as is the present case for nonlinear elasticity, one approach that have traditionally been used for the construction of the preconditioner is the use of block preconditioner (also known as unknown-based preconditioner (Baker et al., 2016)). Although other approaches have been proposed for system of PDEs in elasticity (Baker et al., 2009), in this work we focused on assessing and comparing the performance of two AMG preconditioners: the block and the nodal approaches. The former was not considered for cardiac mechanics so far, whereas the latter was introduced by Augustin et al. (2016).

The block and nodal preconditioning schemes are presented below for elasticity problems. Consider the nonlinear elasticity problem in three dimensions where its stiffness matrix is ordered separating the degrees of freedom (dofs) associated with each

displacement direction, that is:

$$\mathbf{K} = \begin{bmatrix} \mathbf{K}_{xx} & \mathbf{K}_{xy} & \mathbf{K}_{xz} \\ \mathbf{K}_{yx} & \mathbf{K}_{yy} & \mathbf{K}_{yz} \\ \mathbf{K}_{zx} & \mathbf{K}_{zy} & \mathbf{K}_{zz} \end{bmatrix}, \quad (2.72)$$

where the degrees of freedom associated with the displacement in the x direction \mathbf{u}_x are followed by \mathbf{u}_y and then followed by the \mathbf{u}_z dofs.

The block AMG (B-AMG) preconditioner considers the ordering of the dofs as in equation (2.72), and then applies the classical AMG coarsening and interpolation algorithms to the different variables separately, i.e., only to the diagonal blocks \mathbf{K}_{xx} , \mathbf{K}_{yy} and \mathbf{K}_{zz} . This results in a block AMG preconditioner that can be written as

$$\mathbf{M}_{\text{B-AMG}}^{-1} = \begin{bmatrix} \mathbf{M}_{xx}^{-1} & 0 & 0 \\ 0 & \mathbf{M}_{yy}^{-1} & 0 \\ 0 & 0 & \mathbf{M}_{zz}^{-1} \end{bmatrix}, \quad (2.73)$$

where the preconditioning operator is decoupled into three blocks, and the linear system is divided into three problems where different preconditioners \mathbf{M}_{xx}^{-1} , \mathbf{M}_{yy}^{-1} and \mathbf{M}_{zz}^{-1} can be applied in each block. Note that this B-AMG preconditioner ignores the coupling between the unknowns in the x and y direction, x and z , and the others as well. However, as stated and shown in (Baker et al., 2016), it is quite effective and can be compared to more advanced AMG preconditioners in cases when there is a weak coupling between the different unknowns.

The nodal AMG (N-AMG) preconditioner block all unknowns common to the same physical node of the finite element mesh and uses a nodal ordering. In this case the typical structure of the stiffness matrix is

$$\mathbf{K} = \begin{bmatrix} K_{11} & K_{12} & \dots & K_{1n} \\ K_{21} & K_{22} & \dots & K_{2n} \\ \vdots & \vdots & \ddots & \vdots \\ K_{1n} & K_{n2} & \dots & K_{nn} \end{bmatrix}, \quad (2.74)$$

where n is the number of nodes of the finite element mesh and K_{ij} denotes a 3×3 block matrix connecting nodes i and j . In the nodal AMG approach the strong

dependency is considered between any nodes i and j . To compare these block entries K_{ij} typically (Augustin et al., 2016) the Frobenius norm is used which results in a condensed matrix with scalar entries which are then used for the coarsening algorithm of the algebraic multigrid preconditioner.

In the present work, B-AMG preconditioning approach was implemented through the `FieldSplit` feature from PETSc, that allows combining different preconditioners for individual fields or groups of fields. In this strategy, three blocks were created and an AMG preconditioner was applied for each block. While for the N-AMG approach it was necessary to perform a new ordering for the stiffness matrix and then configuring the nodal option in the PETSc library. For both B- and N-AMG preconditioners the BoomerAMG implementation, developed by Henson and Yang (2002) was used.

2.8 Simulations

Different types of cardiac mechanics simulations were performed in the present work to reproduce the LV function, using different material properties and geometries.

First, we validate our solver with respect to the cardiac mechanics benchmark, which consists of three problems, as shown in Figure 2.10(a). The former is the deformation of a beam fixed in the left face, the second problem reproduces the inflation of the left ventricle considering the simplified LV geometry and the later considers the same geometry, but simulates the active contraction of the ventricle.

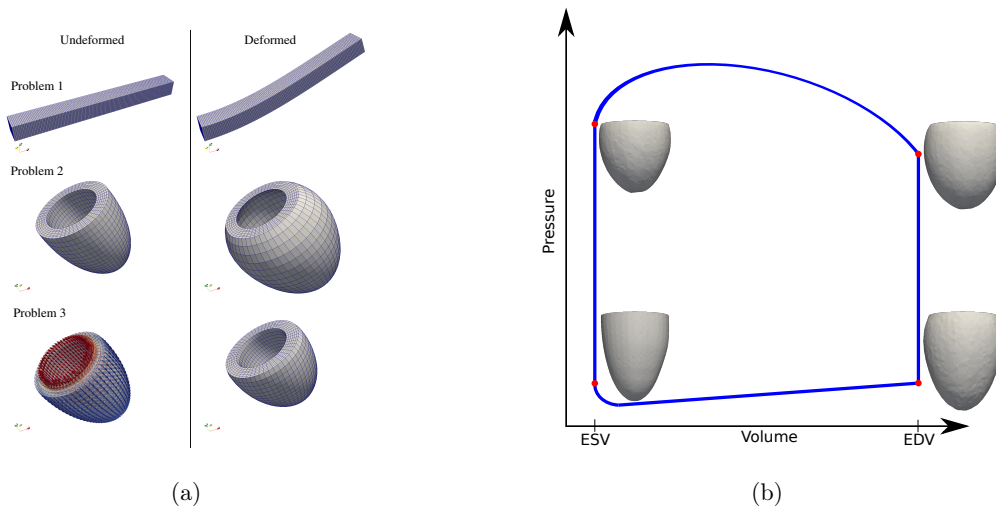


Figure 2.10: Types of cardiac mechanics simulations performed in the present work. (a) Benchmark problems. (b) Simulation of LV function during the full cardiac cycle.

The uncertainty quantification analyses were performed using simulations of the left ventricle that considers personalized geometries created with the presented mesh generator. First, simulations of the passive filling were considered, which are similar to the benchmark problem 2. Then simulations of the full cardiac cycle were considered in the analyses, as that shown in Figure 2.10(b), where the active stress and circulatory models described previously were used.

2.9 Uncertainty quantification and Sensitivity analysis

Scientific computing has been the principal tool to understand complex physical phenomena, where experimental studies can be expensive, difficult and lengthy to repeat. The main goal of computational simulations is the prediction of physical events or engineering problems behavior. To this end, scientific community has devoted extensive effort in order to develop efficient algorithms where the numerical errors are under control. This was the primary goal of numerical analysis which remains an active research field. Only a few studies focused in understanding what is the impact of errors or uncertainties in input data, such as parameters model, initial and boundary conditions and geometries.

The goal of uncertainty quantification is to investigate the impact of these errors in results obtained by computational simulations. Although several models have been successful in representing real phenomena, they are constrained to our ability in assigning

accurate values for several parameters of the governing equations. The uncertainty represents the variability in data and it is present everywhere, because models are not able to reproduce the complete phenomenon and experimental errors are inevitable. Then, in order to completely understand the results of numerical simulations, the capabilities and limitations of computational models, it is necessary to consider uncertainties.

This section presents uncertainty quantification and sensitivity analysis concepts used to investigate uncertainties in inputs of models used in cardiac mechanics simulations. The polynomial chaos approach and a collocation method are described, which have been used through the ChaosPy library (Feinberg and Langtangen, 2015) to quantify uncertainties in the numerical simulations.

2.9.1 An introductory example

Consider an introductory example, presented by Feinberg (2015) and reproduced here, describing the process of a concentration decay in time which is given by

$$u(t) = Ie^{-ct}, \quad (2.75)$$

where I is the initial concentration and c is the decay rate. If there is a small uncertainty in these parameters, the decay behavior can change significantly. Figure 2.11 shows the value of u when I and c are considered as random variables with uniform distributions in the range $(0, 0.1)$ and $(8, 10)$, respectively. Note that a small uncertainty in parameters can cause significant changes in decaying, where the final concentration has a high variation.

This simple example evidences that for some problems, specially a nonlinear problem, a small uncertainty in the input data can cause non-negligible changes in the results. Also, note that these variations can not be captured with increasing the precision of the numerical methods, which makes the incorporation of uncertainties in simulations necessary.

2.9.2 Uncertainty quantification techniques

Different methods have been applied to perform uncertainty quantification analysis, but the most used approach has been to consider uncertain data as random variables and then to reformulate the original deterministic systems as stochastic systems.

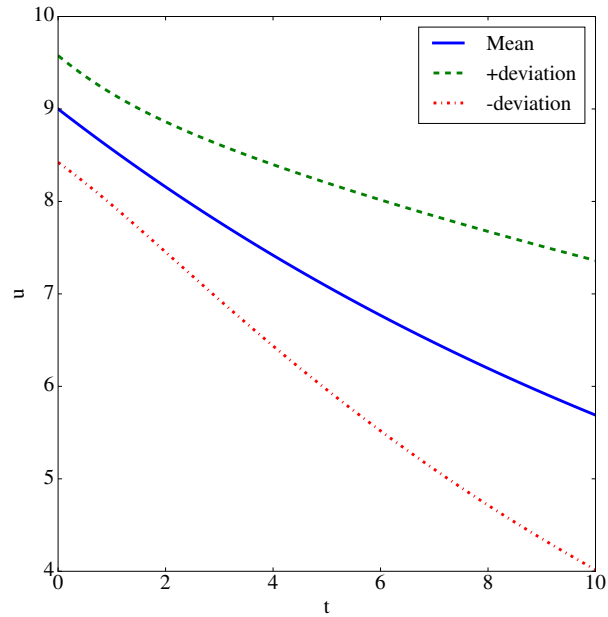


Figure 2.11: Stochastic solutions for the decaying process. The solid line represents the mean solution, whereas the dashed lines represent the deviation of random solutions.

Within this context, one of the most used methods for stochastic simulations is the Monte Carlo (MC) method, which generates independent samples from random model inputs based on a probability distribution. Then MC performs evaluations of the deterministic model using these samples, known as realizations, which are used to obtain statistical information such as mean and standard deviation for the problem. The implementation of this method is simple, but it is necessary a large number of realizations from the deterministic problem in order to obtain an accurate result for the statistical information.

Computation of the mean solution, for instance, converges with a ratio of $1/\sqrt{K}$, where K is the number of realizations (Fishman, 2013). The need of several realizations to obtain an accurate result is very expensive, specially when the deterministic problem solution is already costly.

A popular method, which does not need realizations, is the perturbation method (Nayfeh, 2008), where random fields are expanded using Taylor series around the mean and the series is truncate in a determined order. The expansion order usually is at most quadratic, because the resultant model becomes very complex for higher orders.

This approach has been used in several engineering fields (Liu et al., 1986; Hua et al., 2008). A limitation for this method is that the uncertainty magnitude can not be large, for instance, the method is not accurate for an uncertainty greater than 10%.

A more recent method called generalized polynomial chaos (gPC) (Xiu and Karniadakis, 2002) has been widely used for uncertainty quantification. In this method, stochastic solutions are expressed through an orthogonal polynomial that depends on the random model inputs. Here, different types of orthogonal polynomials can be used for a better convergence of the solution. This method is a spectral representation for the random space and its convergence is fast (Xiu and Karniadakis, 2002).

In order to compare the convergence of the MC and of the gPC methods, consider again the previous example of concentration decay. Figure 2.12 presents a comparison between MC and gPC approaches, in relation to the convergence when applied to uncertainty quantification of equation (2.75). The error when mean and standard deviation are approximated for each method was computed using different numbers of samples, in order to assess the convergence for these specific quantities. As it can be observed, the error decreases rapidly in gPC approach when the number of samples increases, while MC method requires more samples to compute the statistical information in a satisfactory way. This simple introductory example shows the accuracy and efficiency of gPC method with respect to MC in the uncertainty quantification context.

One of the present goals of this work is the study of uncertainty quantification in cardiac mechanics problems, where a deterministic simulation has already a high computational cost. Therefore, the use of Monte Carlo method is not feasible, due to the high number of realizations required in order to obtain an accurate result. Then, the generalized Polynomial Chaos approach was the technique chosen for this work and it will be described hereafter.

2.9.3 Generalized polynomial chaos

The uncertainty quantification investigates what are the effects in an specific quantity of interest when uncertainties are considered in model inputs. These quantities of interest are usually computed from the model solution and can be expressed through generalized polynomial chaos (Xiu, 2010).

Considering a vector $\boldsymbol{\xi} = (\xi_1, \xi_2, \dots, \xi_N)^T$ of model inputs composed by independent

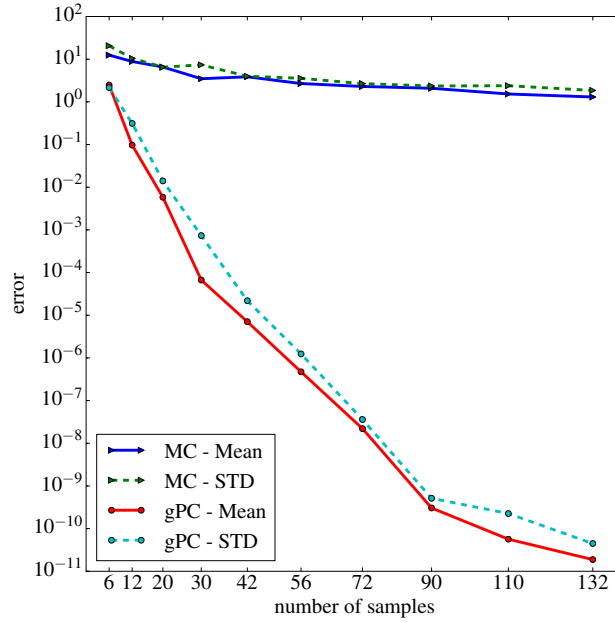


Figure 2.12: Mean and standard deviation errors for Monte Carlo (MC) and generalized polynomial chaos (gPC) methods.

random variables and assuming that the quantity of interest y is written in terms of these variables, it is possible to express this quantity through a infinite polynomial chaos expansion (Li and Zhang, 2007). In practical applications, this quantity of interest can be approximated by a finite expansion obtained through a linear combination of the elements from the polynomial chaos basis, as:

$$\bar{y}(\boldsymbol{\xi}) = \sum_{i=1}^P b_i \Phi_i(\boldsymbol{\xi}), \quad (2.76)$$

where b_i are the unknown coefficients and Φ_i are orthogonal polynomial functions in terms of the random variables. This polynomial chaos expansion with N random variables and order d has P terms, where P is given by

$$P = \frac{(N + d)!}{N!d!}. \quad (2.77)$$

For instance, a second order approximation with two random variables described by

normal distribution has $P = 6$ terms and can be written as

$$\bar{y}(\xi_0, \xi_1) = b_1 + b_2\xi_0 + b_3\xi_1 + b_4(\xi_0^2 - 1) + b_5(\xi_1^2 - 1) + b_6\xi_0\xi_1. \quad (2.78)$$

Defined the approximation for the quantity of interest, as in equation (2.76), it is necessary to determine the coefficients b_i that define the polynomial in terms of the random variables. To this end, a stochastic residual is defined

$$R(\{b_i\}, \boldsymbol{\xi}) = \bar{y} - y. \quad (2.79)$$

The coefficients b_i can be obtained through a weighted residual formulation in the random space, which can be expressed as

$$\int_{\boldsymbol{\xi}} R(\{b_i\}, \boldsymbol{\xi}) v_j(\boldsymbol{\xi}) p^{jt}(\boldsymbol{\xi}) d\boldsymbol{\xi} = 0, \quad (2.80)$$

where $v_j(\boldsymbol{\xi})$, $j = 1, \dots, P$ are the weighting functions and $p^{jt}(\boldsymbol{\xi})$ is the joint probability density function of the input random variables $\boldsymbol{\xi}$. Using this weighted residual formulation it is ensured that the error is orthogonal to the space spanned by the weighting functions and the choice of these functions will define the method properties used in stochastic analysis (Osnes and Sundnes, 2012). A typically choice is the Galerkin method, where weighting functions are the same functions used in polynomial expansion. Galerkin scheme has exponential convergence with respect to the polynomial order used, however this method needs to modify the deterministic numerical solution, resulting in a difficult implementation for complex problems (Li and Zhang, 2007).

2.9.3.1 Stochastic collocation method

An alternative to the Galerkin scheme is the collocation method, which is not intrusive, i.e., it can be applied without modifying the deterministic numerical solution implementation.

In the collocation method, the weighting functions are defined as

$$v_j(\boldsymbol{\xi}) = \delta(\boldsymbol{\xi} - \boldsymbol{\xi}_j), \quad j = 1, \dots, P, \quad (2.81)$$

where δ is the Dirac's delta function and $\boldsymbol{\xi}_j$ are the collocation points, i.e., samples of the input random variables. The collocation points can be chosen in different ways and in the case of multidimensional expansion with order d , the optimal choice is to create collocation points as combinations of the roots for the same expansion with order $d+1$ (Li and Zhang, 2007).

Using (2.81) in the weighted residual formulation (2.80) and taking into account the properties of Dirac delta function, the following relation is obtained

$$R(\{b_i\}, \boldsymbol{\xi}_j) = 0, \quad j = 1, \dots, P, \quad (2.82)$$

and, through the residual definition (2.79), it becomes equivalent to

$$\bar{y}(\boldsymbol{\xi}_j) = y(\boldsymbol{\xi}_j), \quad j = 1, \dots, P. \quad (2.83)$$

This relation defines a system of equations where the unknowns are the coefficients b_i of the polynomial chaos expansion for the quantity of interest. The left hand side of the system (2.83) represents the approximation for the quantity of interest via polynomial expansion \bar{y} evaluated in P collocation points. And the right hand side is defined by the quantity of interest obtained from the deterministic problem solution using the same collocation points. Thus, when collocation method is applied, the deterministic problem must be solved for P realizations using different model input values $\boldsymbol{\xi}_j$, without changing the deterministic solver implementation.

Usually the number of collocation points used is greater than the minimum required P , which results in a better approximation to the statistics (Hosder et al., 2007). In this case, the system becomes over-determined and regression methods are used to solve it (Feinberg and Langtangen, 2015).

The main computational cost is related to the solution of the deterministic problem, which is solved P times to construct the polynomial approximation for the quantity of interest. Hereafter, statistical information for this quantity, such as mean and standard deviation, can be extracted from the polynomial $\bar{y}(\boldsymbol{\xi})$, which typically has a lower evaluation cost than solving the original problem. It is important to remark that the number of quantities of interest is independent with respect to the number of terms P in the approximation, therefore an increase in quantities of interest has a negligible cost.

2.9.4 Sensitivity Analysis

Sensitivity analysis is used to quantify the contribution of each uncertain model input ξ_i to some output quantity of interest y . This analysis is important for model input fixing and input prioritization. Input fixing aims to identify uncertain inputs that have a low impact on the output, and therefore can be fixed in their range of uncertainty in future analyses. On the other hand, input prioritization aims to identify the inputs with the highest impact on the quantities of interest, which are the inputs that should be measured or estimated with the highest possible precision.

2.9.4.1 Sobol sensitivity indices

A variance-based method known as Sobol sensitivity indices (Sobol, 2001) was used in order to quantify input prioritization and fixing, through the main and total sensitivity indices.

The main index S_m^i shows the portion of the total variance in y that could be reduced if the exact value of ξ_i is known. It is computed as follows

$$S_m^i = \frac{\mathbb{V}[\mathbb{E}[y|\xi_i]]}{\mathbb{V}[y]}, \quad i = 1, \dots, N, \quad (2.84)$$

where \mathbb{V} is the variance and \mathbb{E} the expected value. The numerator represents the variance in y caused by uncertainty in ξ_i and the denominator is the total variance.

The total sensitivity index S_t^i represents the direct effect, computed in the main index, and in addition all interactions of ξ_i with the others uncertain inputs:

$$S_t^i = \frac{\mathbb{V}[y] - \mathbb{V}[\mathbb{E}[y|\xi_{i*}]]}{\mathbb{V}[y]}, \quad i = 1, \dots, N, \quad (2.85)$$

where $\mathbb{V}[y]$ is the total variance, ξ_{i*} is a set containing all uncertain inputs except ξ_i , then $\mathbb{V}[\mathbb{E}[y|\xi_{i*}]]$ is the variance caused by all uncertain inputs interactions where ξ_i is involved. The total sensitivity index is particularly useful to identify inputs that can be fixed, which are the inputs with $S_t^i \approx 0$. The variances used in the sensitivity indices computation can be calculated directly from the gPC expansion (Eck et al., 2016).

The presented Sobol indices are used to assess the sensitivity of scalar quantities, but for non-scalars such as time-varying quantities they are not the best choice. Because these indices are scaled by the variance, which is not constant for all point of a time

series Eck et al. (2017). Therefore, for time-varying quantities we computed the time-averaged sensitivity indices, proposed in Eck et al. (2017), where the main time-averaged sensitivity indices are given by

$$TAS_m^i = \frac{\int_{t_0}^{t_1} S_m^i(t) \mathbb{V}[Y]_t dt}{\int_{t_0}^{t_1} \mathbb{V}[Y]_t dt}, \quad (2.86)$$

and the total time-averaged sensitivity indices are computed through

$$TAS_t^i = \frac{\int_{t_0}^{t_1} S_t^i(t) \mathbb{V}[Y]_t dt}{\int_{t_0}^{t_1} \mathbb{V}[Y]_t dt}. \quad (2.87)$$

2.9.5 Surrogate model calibration

The polynomial degree d and the number of samples N_s have been chosen after assessing the convergence of the variance and total Sobol sensitivity indices, as suggested in Eck et al. (2016). The metrics considered and computed were the maximum relative error for the variance and the maximum absolute error for the total Sobol sensitivity indices, which were computed between different polynomial degrees. The maximum relative error among the variance of all QoI is defined as

$$\epsilon_r(d1, d2) = \max \left(\left| \frac{\mathbf{Q}^{d2} - \mathbf{Q}^{d1}}{\mathbf{Q}^{d2}} \right| \right), \quad (2.88)$$

where the vector \mathbf{Q} represents the variance of all quantities of interest, obtained through polynomial Chaos of order $d1$ and $d2$. And the maximum absolute error is defined as

$$\epsilon_a(d1, d2) = \max(|\mathbf{S}_t^{d2} - \mathbf{S}_t^{d1}|), \quad (2.89)$$

with \mathbf{S}_t being the vector of all total Sobol sensitivity indices.

Additionally, we performed a **leave-one-out** cross-validation test (Kersaudy et al., 2015), where we generated $N_s + 1$ samples and one point $\boldsymbol{\xi}^j$ is taken out of the construction of the surrogate model $\hat{f}^{(-j)}$, which is created using $N_s = 3P$ samples. The prediction

error at $\boldsymbol{\xi}^j$ is computed as:

$$\Delta^{(j)} = f(\boldsymbol{\xi}^{(j)}) - \hat{f}^{(-j)}(\boldsymbol{\xi}^{(j)}), \quad (2.90)$$

then after computing $\Delta^{(j)}$ for all $\boldsymbol{\xi}^{(j)}$, the error can be estimated by the leave-one-out error:

$$Err_{LOO} = \frac{1}{n} \sum_{j=1}^n (\Delta^{(j)})^2, \quad (2.91)$$

To facilitate the interpretation of the leave-one-out error, the usually employed Q^2 coefficient was computed as:

$$Q^2 = 1 - \frac{Err_{LOO}}{\mathbb{V}(\boldsymbol{\xi})}, \quad (2.92)$$

where the closer Q^2 is to 1, the better is the approximation of the model.

2.9.6 *ChaosPy*

The Python library ChaosPy (Feinberg and Langtangen, 2015) performs uncertainty quantification and sensitivity analysis through Monte Carlo method and also the generalized polynomial chaos. The unknown coefficients for the gPC can be determined through the collocation method or using a pseudo spectral projection.

ChaosPy is able to generate scalar random variables using different predefined probability distribution, then it is possible to create samples for these variables through different available techniques. With these samples simulations can be performed using the Monte Carlo method or construct polynomial chaos for uncertainty quantification in an specific model.

The Algorithm 2.1 presents an implementation using ChaosPy for uncertainty quantification of equation (2.75). In this example, the stochastic collocation method was used to construct quadratic polynomials chaos. After importing required libraries, the forward model is defined in lines 5 and 6, which depends on time \mathbf{t} , decaying rate \mathbf{c} and initial concentration \mathbf{I} . The last two parameters were considered as stochastic and therefore it is necessary to define a probability distribution for them. In this case, uniform distribution were defined for these parameters in lines 9 and 10. Next, the number of realizations required to create the polynomial chaos is computed, according to equation (2.77). Then samples are generated in line 15, considering the defined

distribution, and the model is evaluated for each sample, as shown in line 16.

A polynomial chaos is created using the function presented in line 18, which generate an orthogonal polynomial with order d based on a given distribution. Then, polynomial coefficients are determined in line 19 through information about the polynomial chaos expansion, the generated samples for the random model inputs and the model evaluations for these samples. Thus, a polynomial that approximates the quantity of interest is obtained and it is possible to compute statistical measurements from this approximation, such as mean and standard deviation computed in lines 21 and 22.

```

1 import chaospy as cp
2 import numpy as np
3 from math import factorial
4
5 def model(t, c, I):
6     return I*np.exp(-c*t)
7
8 t = np.linspace(0.001, 10, 101)
9 c1 = cp.Uniform(0,0.1)
10 c2 = cp.Uniform(8,10)
11 distribution = cp.J(c1, c2)
12 d = 2
13 P = factorial(2+d)/(factorial(2)*factorial(d))
14
15 samples = distribution.sample(P, "M")
16 evals = [model(t, sample[0], sample[1]) for sample in samples.T]
17
18 polynomial_expansion = cp.orth_ttr(d, distribution)
19 model_approx = cp.fit_regression(polynomial_expansion, samples,
20                                 evals)
21
22 expected = cp.E(model_approx, distribution)
23 deviation = cp.Std(model_approx, distribution)

```

Algorithm 2.1: Algorithm for uncertainty quantification in equation (2.75) using the ChaosPy library.

The library allows customization, such as the creation of new probability distribution, construction of new polynomials, new sampling schemes and new approaches to generate collocation or integration points. Due to its simple use and flexibility this library has been chosen as uncertainty quantification and sensitivity analysis tool in the present work. See more details in the work of Feinberg and Langtangen (2015).

2.9.7 Uncertainty quantification in cardiac mechanics

The investigation of complex problems that can help in clinical diagnostics have been possible due to the development of mathematical and geometric models that are more realistic in describing the cardiac function, and the use of efficient numerical methods to solve these models. Within this context, patient specific simulations have been subject of significant medical and scientific interest (Trayanova and Winslow, 2011; Lee et al., 2014), where it is necessary to use a different set of parameters and geometries for each patient. These model inputs vary significantly among patients and it is necessary to quantify how these developed models behave in different scenarios. Then, recent studies have focused in the uncertainty quantification of models representing the electrical and mechanical activities of the heart.

An uncertainty quantification analysis have been performed by Hurtado et al. (2017) through the polynomial chaos approach, using an electro-mechanical 3D model of the heart. The action potential duration and the maximum calcium concentration were some of the quantities of interest considered, which were the most influenced by uncertainties in parameters representing the maximal calcium conductance and the maximal conductance of the slow delayed rectifier potassium channel.

In the context of cardiac mechanics, Osnes and Sundnes (2012) quantified uncertainties in parameters of a constitutive law for the cardiac tissue, considering a tridimensional simulation of the left ventricle during the diastole phase. The polynomial chaos approach has also been used combined with the collocation method and the quantities of interest most impacted by uncertainties were the displacement and rotation at the apex, and the torsion at the ventricle base. An analysis considering the same type of simulation was reported in Rodríguez-Cantano et al. (2019), where uncertainties in the fiber orientation field were also included. The sensitivity of fiber stress and strain due to variations in left ventricle shape have also been shown in Choi et al. (2010); Barbarotta and Bovendeerd

(2019). Whereas the impact of variability in shape (Di Achille et al., 2018) and material properties (Kallhovd et al., 2019) has also been investigated in simulations reproducing the ventricular function during the entire cardiac cycle.

The uncertainty quantification has also been applied in studies of the circulatory system, such as in the work of Huberts et al. (2014) that consider uncertainties in flow simulations within arteriovenous fistulae. Whereas in the work developed by Biehler and Wall (2018) uncertainties were considered in geometries of abdominal aortas aneurysms, where the wall thickness of aneurysms was considered as a scalar stochastic variable and also as stochastic field. Then, the analysis quantified how uncertainties in geometries impacts in the stress and in the aneurysm rupture risk.

Uncertainty in wall thickness is likely to be important also in cardiac mechanics models, since the overall mechanical properties of the myocardial wall are tightly linked to its thickness, and because patient specific models created from images are likely to include noise and uncertainty. Also, these models are typically constructed by semi-manual segmentation of echocardiographic or magnetic resonance images (Crozier et al., 2016). The resolution of the images varies substantially with the image modality and the direction (axis) considered, with typical values in the order of 1-5 mm. The process becomes a source of uncertainty because the contour extraction depends on user intervention, and will directly impact the ventricle wall thickness and other measurements, as discussed by Suinesiaputra et al. (2014). Furthermore, there is substantial variability of anatomical parameters among patients, as presented in the work of Bai et al. (2015) which reported about 15% of variability in the wall thickness of healthy patients. Under pathological conditions the variability can increase even more, as in the case of asynchronous electrical activation (Prinzen et al., 1995; Van Oosterhout et al., 1998; Vernooij et al., 2004). For instance, in the work of Van Oosterhout et al. (1998) an experiment with dogs was reported where the late activated region wall thickness increased $23 \pm 12\%$. The same study also reported an experiment in patients with left bundle branch block (LBBB), where the septum thickness decreased about 20% and the thickness in the free wall increased approximately 10%. These natural and pathological variations indicate that an accurate reconstruction of the patient anatomy is important for clinical applications. However, to properly assess the demands on this reconstruction it is important to quantify the impact of these variations on the model's predictions.

3 Cardiac mechanics solver performance

Before presenting the main contribution of the thesis, which is related to quantify how uncertainties impact on the cardiac mechanics simulations, we present the numerical improvements performed in the solver.

This chapter presents results for the numerical approach presented in this work and implemented in the in-house cardiac mechanics solver named Cardiax, where we carried out several simulations for the cardiac mechanics benchmark problems. First we present the results in order to validate our implementation. Next, we present some results with focus on the performance of the block- and nodal-AMG preconditioners for cardiac mechanics only. Finally, we assess the performance and accuracy with respect to volume changes of the ALG formulation for the benchmark problems. The results presented in this chapter were published in the work Campos et al. (2018).

3.1 Benchmark problems

The benchmark consists of three problems and uses the constitutive model proposed by Guccione et al. (1995) for passive cardiac tissue. Figure 3.1 shows the geometry of the three problems in their undeformed and deformed configurations.

The first problem consists of a deforming rectangular beam whose geometry is defined by $x \in [0, 10]$, $y \in [0, 1]$, $z \in [0, 1]$ mm. The transversely isotropic Guccione constitutive law was used with the following parameters: $C = 2$ kPa, $b_f = 8$, $b_t = 2$, $b_{fs} = 4$. The fiber direction is constant along the long axis, i.e. $(1, 0, 0)$. Boundary conditions: the left face ($x = 0$) is fixed in all directions and a pressure of 0.004 kPa is applied to the entire bottom face ($z = 0$).

The second problem involves the inflation of an ellipsoid-like geometry, as presented in section 2.4.1, representing a simplified left ventricle, with isotropic material parameters. This problem tests a deformation pattern similar to cardiac inflation. The Guccione model was used with the following parameters: $C = 10$ kPa, $b_f = 1$, $b_t = 1$, $b_{fs} = 1$. Boundary

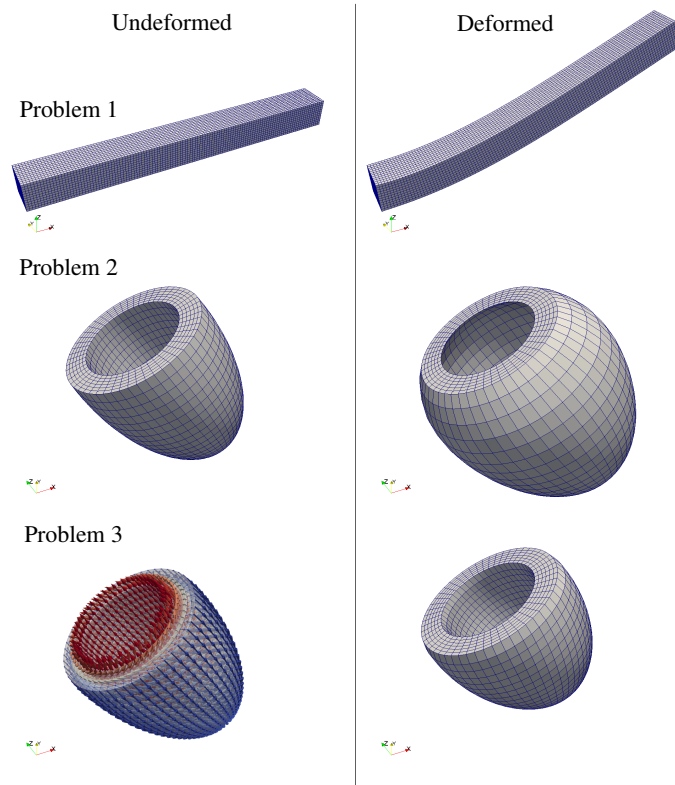


Figure 3.1: Undeformed and deformed configurations of the benchmark problems 1-3. The arrows in the undeformed configuration for problem 3 indicates the fiber orientation.

conditions: the base plane ($z = 5 \text{ mm}$) is fixed in all directions and a pressure of 10 kPa is applied to the endocardial surface.

The third problem used the same geometry from the second problem, but it considers a transversely isotropic material simulating the inflation and active contraction of the left ventricle. This problem tests the active contraction and uses a complex realistic fiber distribution, which are important features for a cardiac mechanics solver. This problem used the following parameters: $C = 2 \text{ kPa}$, $b_f = 8$, $b_t = 2$, $b_{fs} = 4$. Boundary conditions: the base plane ($z = 5 \text{ mm}$) is fixed in all directions, a pressure of 15 kPa is applied to the endocardial surface and an active stress $T_a = 60 \text{ kPa}$ is applied in the fiber direction.

At this point it is important to remark that problems 1 and 2 are purely passive and as such the active stress component in equation (2.24) is not considered. Only problem 3 of the benchmark considers the active part of the additive split of the stress tensor, where equation (2.25) is used to apply the active stress in the fiber direction.

3.1.1 Benchmark metrics

In order to compare the tested solvers in the benchmark, displacements and strain in different points of the domain are measured. For problem 1, the deformed z component of displacement is measured in the position $(10, 0.5, 1)$, represented by the green point in Figure 3.2.

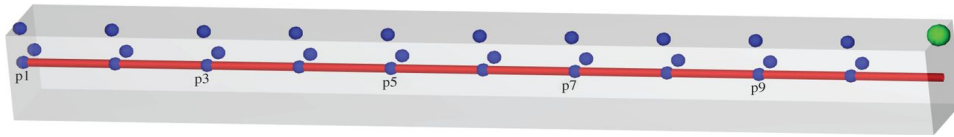


Figure 3.2: Problem 1 geometry, where observed measures are: the deformed z position in the green point; the deformed configuration of the red line; and the strains computed in axial directions using the blue points. (extracted from Land et al. (2015))

The deformed configuration of the red line in the same figure, located in $(x, 0.5, 0.5)$, is also compared among the solvers. Finally, some strain measures are computed in the points $p1 - p10$, which are located under the red line. The strains are computed in x , y and z directions, using the blue points.

The strains S_i are computed from the distance change between pair of n points with coordinates X_1^i and X_2^i in the undeformed configuration and the coordinates in x_1^i and x_2^i in deformed configuration, where $i = 0, 1, \dots, n$. In order to compute the strain, a finite difference scheme is used:

$$S_i = \left(\frac{\|x_1^i - x_2^i\|}{\|X_1^i - X_2^i\|} \right) \times 100\%. \quad (3.1)$$

For x direction, the neighbor points along the red line are used: $X_1^i = (i, 0.5, 0.5)$ and $X_2^i = (i + 1, 0.5, 0.5)$, $i = 0, 1, \dots, 8$. And for the transversal directions the used points are $X_1^i = (i, 0.5, 0.5)$ and $X_2^i = (i, 0.9, 0.5)$ for y direction and $X_2^i = (i, 0.5, 0.9)$ for z direction, $i = 0, 1, \dots, 9$.

For the problems 2 and 3 the deformed z positions of the ventricle apex are measured in the endocardium and epicardium, represented by the green points in Figure 3.3. Other comparison measure is the deformed configuration of the red line located in the ventricular middle wall. And the strain measurements in longitudinal, circumferential and radial directions are also computed in points of the endocardium, epicardium and middle wall. The longitudinal and radial strains are calculated in the points $p1 - p10$ through the blue

points in Figure 3.3(a) and the circumferential strains is obtained using the blue points presented in Figure 3.3(b).

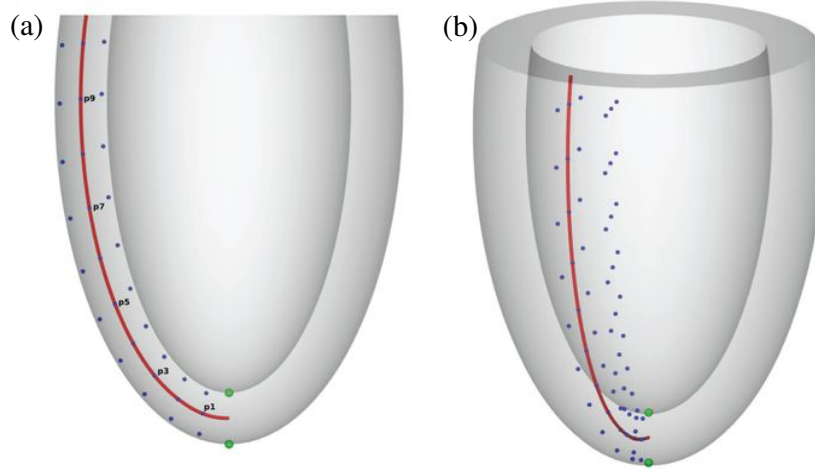


Figure 3.3: Undeformed geometry used in problems 2 and 3, with green points indicating location to measure apex displacement at endocardium and epicardium; middle wall apex-base line in red and blue points to compute strains. (a) Blue points used to compute longitudinal and radial strains ($v_i = 0$) at the points p1-p9 under the red line. (b) Blue points used to compute circumferential strains ($v_i = \pi/10$) at points p1-p9. (extracted from Land et al. (2015))

The points used in strain calculation are obtained from the parametrization (2.22), extract the points along the apex-base lines: $v_i = 0$, $u_i = u_1 + (u_2 - u_1)/n_u \times (i + 1) \times 0.95$, where $u_1 = -\pi$, $u_2 = -\arccos 5/(17 + 3t)$, $n_u = 10$, with $i = 0, 1, \dots, n_u - 1$. These lines are extracted along the endocardium ($t = 0.1$), epicardium ($t = 0.9$) and middle wall ($t = 0.5$). The pairs of neighbor points along each line are used to compute the longitudinal strains. While the pairs of points between endocardium and middle wall; middle wall and epicardium; endocardium and epicardium are used to compute the radial strain at endocardium, epicardium and middle wall, respectively. In order to obtain the circumferential strain, the second point X_2^i is derived from the rotation of each line by an angle $v_i = \pi/10$, instead of $v_i = 0$, as shown in Figure 3.3(b).

3.1.2 Metric to compare Cardiax with the benchmark participants

Prior to investigating the performance of the Augmented Lagrangian method combined with a block-AMG preconditioner, we first assessed the ability of the Cardiax code with the STP formulation in (2.60) for solving the benchmark problems proposed by Land

et al. (2015).

To this end we considered the value of the solution in key points of the three benchmark problems as a reference, which are the green points presented in Figures 3.2 and 3.3. An average value of the solution \tilde{s} in these key points considering the results of all participants codes in the benchmark (Land et al., 2015) was computed. To compare our results with this average, we considered the relative error

$$error = \frac{s - \tilde{s}}{\tilde{s}}, \quad (3.2)$$

where s is the value of the solution obtained by our code at the selected key point.

In order to obtain a reference solution for each problem we performed a series of experiments where we tuned the corresponding parameters of our solvers. The κ value associated to the results with smallest relative error (3.2) was considered as a reference for further comparison of accuracy and performance of the numerical methods discussed.

3.1.3 Experiments

The experiments proposed in the cardiac mechanics benchmark, detailed in Figure 3.1, were performed with Cardiax considering the following meshes: for Problem 1, a mesh of $50 \times 5 \times 5$ elements was used, whereas, for both Problems 2 and 3, a mesh of $24 \times 54 \times 6$ elements was considered. In each case the *error*, given by (3.2), between our solution and the average of the results from the benchmark, was below 1%. The Newton method was used to solve the nonlinear problem with a fixed number of load increments. For the first problem 10 load increments were used, whereas 100 load increments were used for the second and third problems. The Newton convergence criterion used was based on the residual norm with 10^{-6} specified as tolerance. The preconditioned GMRES method was used for the solution of the linear systems considering a relative convergence tolerance in the residual norm of 10^{-4} . The BoomerAMG preconditioner was used with the default settings, that is, a V-cycle V(1,1) scheme was considered with the Falgout coarsening strategy and a symmetric-SOR/Jacobi for relaxation.

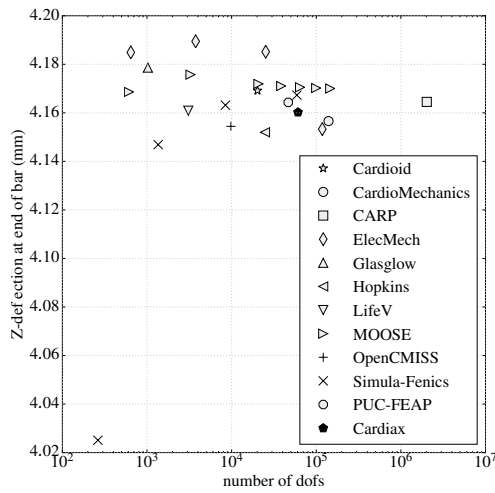
Figure 3.4(a)-(c) shows the same graphs used by the cardiac mechanics benchmark (Land et al., 2015), but here we added our results to verify the accuracy of the solution obtained by our code and compare it to the other implementations.

Figure 3.4(a) shows our results combined with the results from the benchmark participants for Problem 1. In particular, in this case a value of $\kappa = 70$ kPa resulted in an error of 0.15%. Smaller values such as $\kappa = 50$ kPa resulted in errors above 1%, which quickly deviates from the other results of the benchmark.

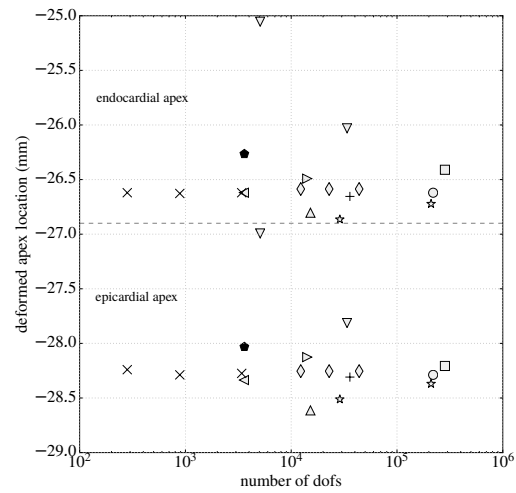
The results for the Problems 2 and 3 are shown Figure 3.4(b) and (c). For Problem 2 we found that $\kappa = 300$ kPa resulted in an error of 0.86%, whereas for Problem 3 a larger value such as $\kappa = 1000$ kPa had to be used in order to obtain an error of 0.78%. All these *errors* are within the standard deviation of the benchmark results. Table 3.1 shows the average solution and standard deviation (computed from the benchmark data (Land et al., 2015)) at the key points for the three benchmark problems.

Table 3.1: Average solutions and standard deviation computed at the key points from the results of the cardiac mechanics benchmark (Land et al., 2015).

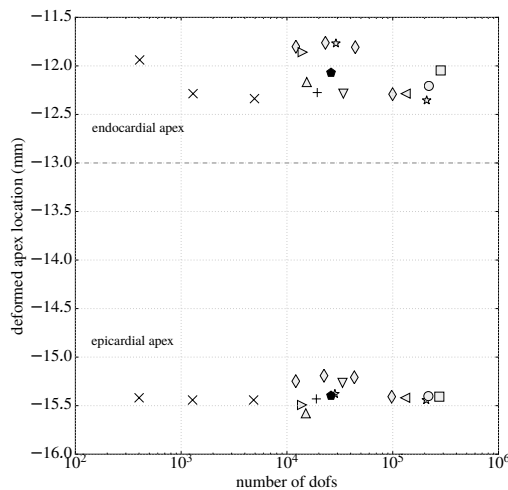
	Average Solution (Key point)		Standard deviation (Key point)	
Problem 1	4.161 (Tip)		0.032 (Tip)	
Problem 2	-28.196 (Epi)	-26.482 (Endo)	0.363 (Epi)	0.440 (Endo)
Problem 3	-15.405 (Epi)	-12.098 (Endo)	0.108 (Epi)	0.231 (Endo)



(a) Problem 1



(b) Problem 2



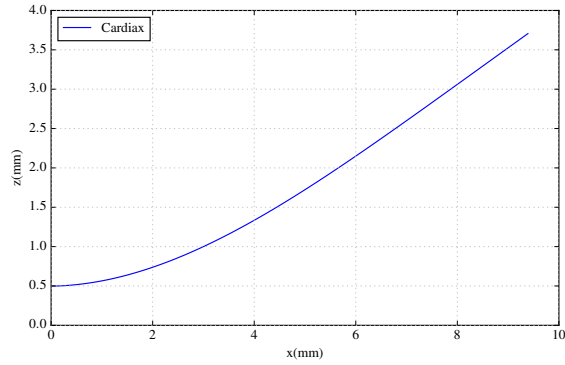
(c) Problem 3

Figure 3.4: Benchmark results, where the labels in this graph refer to all the codes tested in the benchmark paper, except our results which were added here under the label Cardiax.

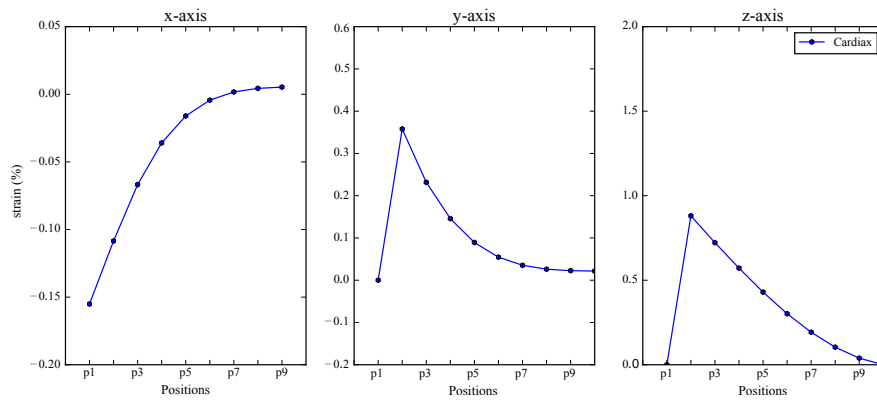
We notice that our results are close to the mean of the codes tested in the cardiac mechanics benchmark (Land et al., 2015), demonstrating that our code was able to simulate the cardiac mechanical activity properly.

The deformed line in the domain center and the axial strains are presented in Figure 3.5 for problem 1. These measures provide global information about the solution behavior,

where the present solver obtained satisfactory results, closer to the results presented in the benchmark tested solvers.



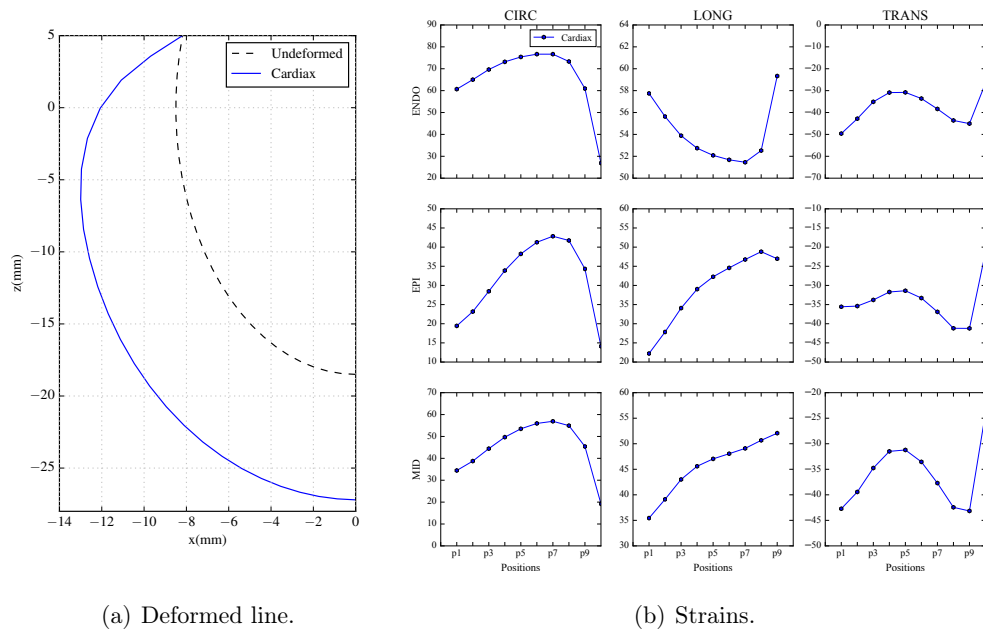
(a) Deformed position of a line.



(b) Strains.

Figure 3.5: Problem 1: (a) deformation of the line $(x, 0.5, 0.5)$; (b) strain along the lines in direction of x -, y - and z -axes.

Figure 3.6 shows the results for problem 2, where the deformed line in the middle wall is presented in panel (a), while the strain measures in circumferential, longitudinal and transmural directions are presented in panel (b). Strains are computed in different points of the endocardium, epicardium and middle ventricular wall. Both plots have qualitative and quantitative behavior similar to the results presented in (Land et al., 2015).



(a) Deformed line.

(b) Strains.

Figure 3.6: Problem 2: (a) deformation of a line in the middle of ventricular wall and (b) strain measures in the circumferential (CIRC), longitudinal (LONG) and transmural (TRANS) directions at different positions.

The same measures are now presented to problem 3 in Figure 3.7, where the deformed line after the contraction is presented in panel (a) and the strains are presented in (b), which are also in agreement with the benchmark results.

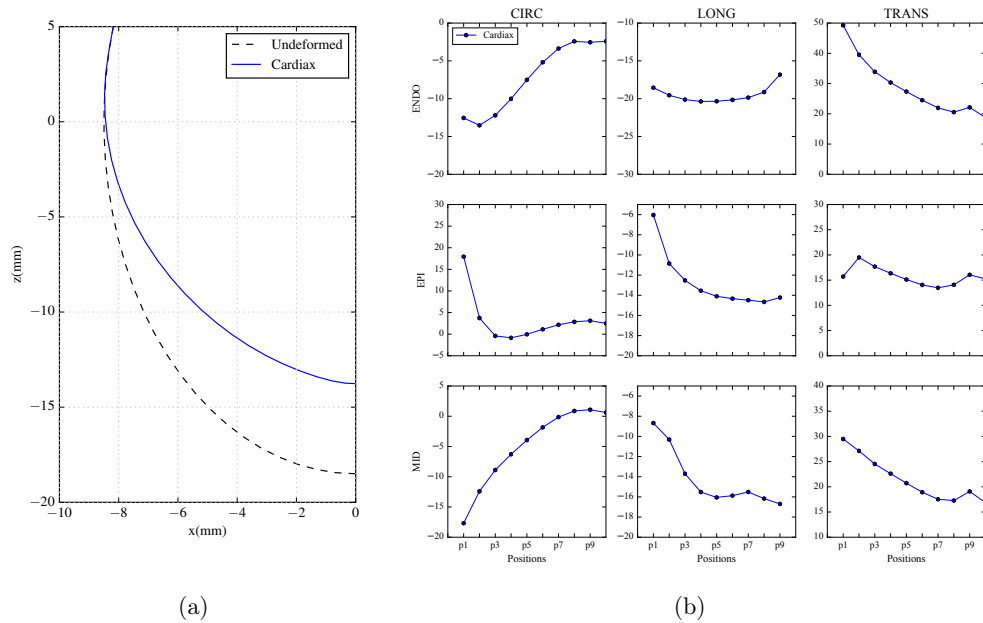


Figure 3.7: Problem 3: (a) deformation of a line in the middle of ventricular wall; (b) twisting motion of the same line; and (c) strain measures in the circumferential (CIRC), longitudinal (LONG) and transmural (TRANS) directions at different positions.

Another test was still performed for problem 3, in order to view the ventricle torsion behavior, due to the helix fiber orientation. Figure 3.8 presents this result for the line in the middle wall, where the dashed line represents the undeformed configuration, which moves to the blue line after contraction. This behavior is also in agreement with results presented in the benchmark.

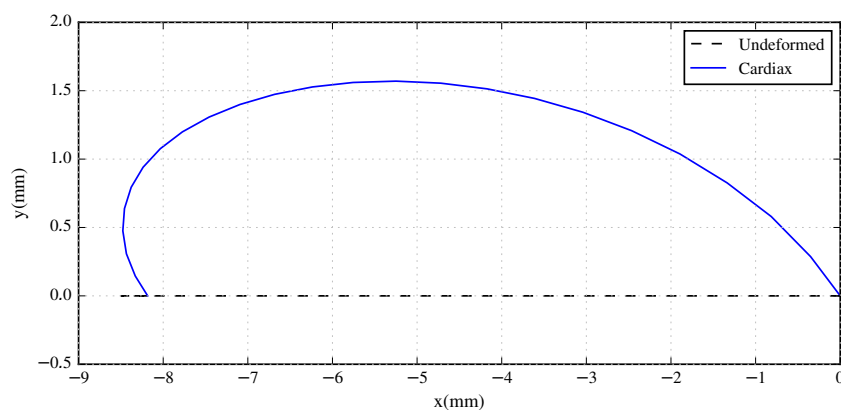


Figure 3.8: Twisting motion of the middle wall line for problem 3.

3.2 Performance of the preconditioners

After the first set of simulations was performed and satisfactory results were obtained for the benchmark problems, we focused on the AMG preconditioners and on the Augmented Lagrangian for improving the performance of cardiac mechanics simulations.

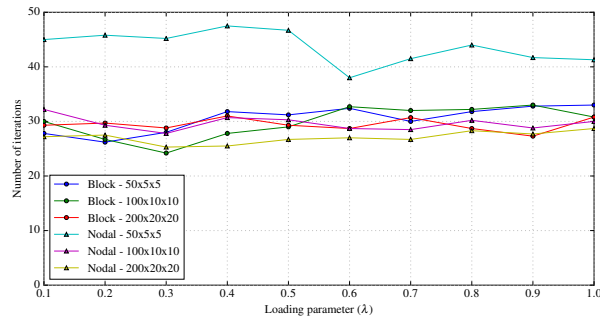
Initially, we assessed the performance of the B-AMG and N-AMG preconditioners using the STP formulation. The influence of the preconditioners was analyzed mainly through the number of iterations spent by the linear system solver. Another important property that was investigated was the robustness of the block-AMG preconditioner with respect to the problem size. Thus, refined meshes for each problem were created and we observed the behavior of the Krylov solver for these instances to assess the performance of the preconditioner.

Table 3.2 presents the number of iterations required by the Newton method to converge and the average of GMRES iterations (within the Newton step) selected at different stages of the solution using the block and nodal preconditioners. It shows that the GMRES method converged with a reasonable number of iterations for all problems, even for the most difficult Problem 3.

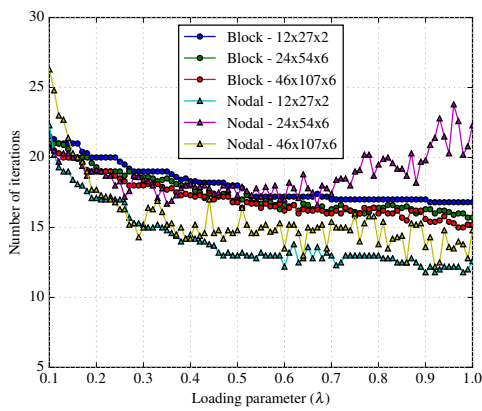
Table 3.2: Block (B) and nodal (N) AMG preconditioners performance study: number of Newton iterations and average of GMRES iterations at some selected loading parameters (λ)

λ	Problem 1				Problem 2				Problem 3			
	Newton		GMRES		Newton		GMRES		Newton		GMRES	
	B	N	B	N	B	N	B	N	B	N	B	N
0.1	6	6	30.0	32.2	6	6	21.0	20.7	6	6	33.0	42.5
0.2	5	6	26.7	29.3	7	7	19.3	19.1	6	6	33.2	35.5
0.3	5	6	24.2	27.8	7	7	18.6	18.4	6	6	30.7	32.5
0.4	5	6	27.8	30.7	7	7	18.0	18.1	6	7	29.2	28.3
0.5	5	6	29.0	30.3	7	6	16.9	17.3	7	6	28.6	27.3
0.6	5	6	32.7	28.7	7	7	16.6	17.0	6	6	27.7	26.2
0.7	5	6	32.0	28.5	6	7	16.3	17.4	5	5	27.2	25.8
0.8	5	6	32.2	30.2	9	8	16.4	19.5	5	5	26.4	24.6
0.9	5	6	33.0	28.8	6	6	16.3	19.8	5	4	26.6	24.8
1.0	5	6	30.8	30.0	7	9	15.7	22.3	6	5	27.5	25.0

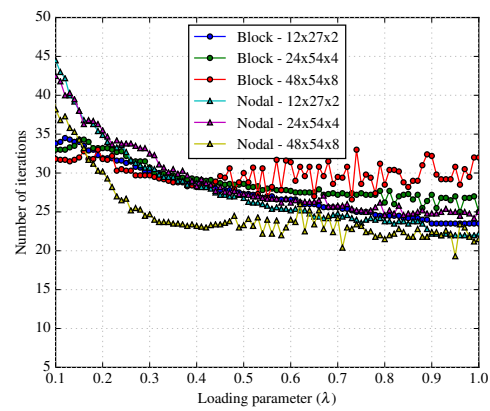
Next we evaluated the performance of the block and nodal AMG preconditioners when the meshes used for the problems were refined. Figure 3.9 shows the average of GMRES iterations per step for different levels of mesh refinements. In a mean sense, it is possible to notice that the number of GMRES iterations does not increase when the mesh is refined for all the problems, except in problem 2 for the nodal-AMG preconditioner which seemed more sensitive to the mesh refinement than the block preconditioner.



(a) Problem 1



(b) Problem 2



(c) Problem 3

Figure 3.9: Comparison of GMRES iterations for each loading parameter (λ) for different mesh discretizations of the geometry in the benchmark problems.

Concerning a performance comparison between both preconditioners Tables 3.3 and 3.4 show the mean number of GMRES iterations for different loading parameters and the total solution time for block and nodal AMG preconditioners, respectively. Although in terms of GMRES iterations the block and nodal AMG preconditioners are, in general, competitive within the 3 problems considered, it is clear that the nodal AMG preconditioner is much faster in terms of execution time for all the cases.

Table 3.3: Block AMG preconditioner: average of GMRES iterations at different loading parameters (λ) and total solution time in seconds for the benchmark problems using different mesh refinements.

λ	Problem 1			Problem 2			Problem 3		
	50x5x5	100x10x10	200x20x20	12x27x2	24x54x6	46x107x6	12x27x2	24x54x4	48x54x8
0.1	27.8	30.0	29.3	21.5	21.0	20.7	33.8	33.2	35.4
0.2	26.2	26.7	29.7	20.0	19.3	19.0	31.9	33.2	32.4
0.3	28.0	24.2	28.8	19.0	18.6	18.0	30.2	30.7	28.7
0.4	31.8	27.8	31.0	18.3	18.0	17.3	28.8	29.2	26.2
0.5	31.2	29.0	29.3	18.0	16.9	16.8	27.3	28.6	25.4
0.6	32.4	32.7	28.7	17.2	16.6	16.2	26.6	27.7	24.2
0.7	30.0	32.0	30.7	17.0	16.3	16.0	25.6	27.2	22.2
0.8	31.8	32.2	28.7	17.0	16.4	16.0	24.5	26.4	20.7
0.9	32.8	33.0	27.3	17.0	16.3	15.6	23.5	26.6	21.0
1.0	33.0	30.8	30.8	16.8	15.7	15.2	23.5	27.5	21.8
Time (s)	41	431	6835	161	3060	9098	424	7568	45080

Table 3.4: Nodal AMG preconditioner: average of GMRES iterations at different loading parameters (λ), and total solution time in seconds for the benchmark problems using different mesh refinements.

λ	Problem 1			Problem 2			Problem 3		
	50x5x5	100x10x10	200x20x20	12x27x2	24x54x6	46x107x6	12x27x2	24x54x4	48x54x8
0.1	45.0	32.2	27.2	22.3	20.7	26.3	44.5	42.5	38.2
0.2	45.8	29.3	27.5	17.1	19.1	17.7	34.9	35.5	30.2
0.3	45.2	27.8	25.3	15.2	18.4	15.0	30.7	32.5	24.7
0.4	47.5	30.7	25.5	14.5	18.1	14.2	28.7	28.3	23.2
0.5	46.7	30.3	26.7	13.0	17.3	14.8	26.8	27.3	23.3
0.6	38.0	28.7	27.0	12.2	17.0	13.5	25.2	26.2	24.0
0.7	41.5	28.5	26.7	13.0	17.4	15.4	24.8	25.8	24.2
0.8	44.0	30.2	28.3	13.0	19.5	13.8	23.8	24.6	21.5
0.9	41.7	28.8	27.7	11.8	19.8	13.6	22.2	24.8	22.4
1.0	41.3	30.0	28.7	12.6	22.3	14.8	22.2	25.0	21.5
Time (s)	22	194	2557	34	1411	4394	68	1244	6320

3.3 Augmented Lagrangian formulation

Here we present performance results of the ALG formulation when it is combined with the AMG preconditioners. As we already mentioned, the ALG formulation allows controlling the volume change *a priori* and thus it allows the use of smaller values for penalty parameter κ while keeping the desired level of volume change in a element-wise fashion.

As a result we have linear systems that are less ill-conditioned, which result in faster convergence of the iterative solvers. In all simulations of this experiment we used a tolerance for the element-wise volume change given by $tol = 0.05$ when ALG formulation was used. The experiments were performed considering the following meshes: for Problem 1, a mesh of $120 \times 12 \times 12$ elements was used, whereas, for Problem 2 a mesh of $12 \times 27 \times 2$ elements was considered and for Problem 3 we used a mesh of $24 \times 54 \times 6$ elements.

In order to evaluate the performance of the Augmented Lagrangian formulation we carried out the simulations using ALG in contrast with the simulations without it, that is, considering the STP formulation. The performance of the Augmented Lagrangian approach was evaluated using the number of iterations of the Newton method, the number of iterations of the GMRES solver, the execution time measured in seconds, the total volumetric changes (VC) as the ratio of deformed to the undeformed volume and also the maximum value of $|\tilde{J} - 1|$ within all elements of the mesh.

For all the three benchmark problems, we considered the STP formulation together with the values of the κ parameter that resulted in the smaller errors as a reference. Then, for the ALG method we started using the same κ used in the STP formulation and progressively reduced it, while controlling volumetric changes using the tol parameter of the ALG approach. We proceeded reducing the value of κ iteratively keeping *error* below a specified value of 0.2% for problem 1 and of 2% for problems 2 and 3. We found that since there was less variability in the results of the benchmark for problem 1 a smaller value had to be used, while with 2% for the other problems all the results obtained were in good agreement with the average of the benchmark data. Henceforth, we compared the performance of the STP and ALG formulations, taking the previous κ for the STP and the reduced value for the ALG formulation. It is important to remark that simply reducing κ in the STP formulation results in large volumetric changes and unacceptable measures for the *error*, whereas in the ALG approach we can control volume changes and thus keeps the *error* under control.

Table 3.5 shows the κ values for the STP formulation and also the one which resulted in the best results for the ALG approach, time spent by the linear solver, element-wise volume change and global volumetric change (VC) for the benchmark problems simulations using ALG and STP (without ALG) formulations.

It is important to note that three different problems have been considered and for each

problem a different value for κ could be used. Further, after a reference value for κ in each problem was defined, the results from Table 3.5 shows that when the ALG approach was used with a reduced κ , an improvement in performance was obtained, the volumetric changes are under control and the error with this simulation is close to the error without ALG considering a larger value for κ .

For the Problem 1 we could not further reduce κ for two reasons: when this parameter is reduced the *error* increases and the results quickly diverge from the average of the benchmark data; and the volumetric changes in this problem are quite small, for instance, ranging from 0.007 to 0.03 when κ varies from 70 to 10 kPa. Therefore, in this problem the ALG approach could not improve performance when using the block preconditioner and with the nodal preconditioner an improvement of about 24% was obtained.

When κ was reduced from 300 to 40 kPa in Problem 2 we obtained a $2\times$ performance improvement using ALG formulation with the block preconditioner and 60% with the nodal preconditioner, while keeping the *error* smaller than 1%. In this case, simply reducing κ in the STP formulation results in a volumetric change of $|\tilde{J} - 1| = 0.1$, which is quite large for cardiac mechanics.

For Problem 3 the original $\kappa = 1000$ kPa from the STP formulation was reduced to $\kappa = 100$ kPa resulting in an *error* below 2%. With this setting the ALG formulation achieved an improvement of about 91% and 21% for the block and nodal preconditioners, respectively, and the volume change was kept below the tolerance for the ALG formulation, whereas for the STP it achieved a higher value. Although the *error* here was bigger than the other cases, it can be considered as a satisfactory result within the benchmark problem 3 and comparable to the results of other participants codes in the benchmark as shown in Figure 3.4(c). To summarize, with this choice of κ we obtained an improved performance while controlling volumetric changes and the *error*. The results with $\kappa = 100$ kPa in the STP formulation delivered a very high error of about 8%, and unacceptable results both for the key points and volumetric changes.

We also remark that in all problems small global volume changes, denoted in Table 3.5 by VC, have been achieved. In particular for problem 1 very small changes were observed, whereas for problems 2 and 3 values of the same order of magnitude of *tol* were obtained.

Table 3.5: Comparison of STP and ALG: bulk modulus κ , global volume change (VC), volumetric changes measured as $\max |\tilde{J} - 1|$ within all finite elements, *error* and time spent by the linear solver using the block (B-AMG) and nodal (N-AMG) preconditioners.

	Formulation	κ (kPa)	VC	$\max \tilde{J} - 1 $	error (%)	B-AMG	N-AMG
Problem 1	STP	70	$1e-5$	0.01	0.15	847	562
	ALG	70	$1e-5$	0.01	0.14	995	452
Problem 2	STP	300	0.02	0.01	0.86	161	34
	ALG	40	0.02	0.04	0.63	76	21
Problem 3	STP	1000	0.01	0.09	0.78	10886	1551
	ALG	100	0.03	0.05	1.88	5679	1281

The most significant impact of the ALG formulation is on the iterative solver performance as shown in Table 3.6 for problems 2 and 3 only. The table presents the number of Newton iterations and the average of GMRES iterations in the Newton steps selected at different stages of the solution. The Uzawa iterations are also presented for the ALG results which were obtained with block preconditioners.

Table 3.6: Newton iterations and average of GMRES iterations (its) at different loading levels (λ) for the benchmark problems. For ALG results, the Uzawa iterations (Uz) are also presented. (Problem 2 with STP formulation used $\kappa = 300$ kPa and with ALG used $\kappa = 40$ kPa; Problem 3 with STP formulation used $\kappa = 1000$ kPa and with ALG used $\kappa = 100$ kPa).

λ	Problem 2			Problem 3		
	STP	ALG		STP	ALG	
	Newton (its)	Uz	Newton (its)	Newton (its)	Uz	Newton (its)
0.1	6 (21.5)	2	7 (9.9)	6 (32.7)	3	10 (14.1)
0.2	7 (20.0)	2	7 (9.0)	6 (32.8)	2	7 (13.0)
0.3	6 (19.0)	2	7 (9.0)	7 (29.9)	2	10 (12.5)
0.4	6 (18.3)	2	7 (8.8)	7 (29.0)	2	10 (12.2)
0.5	5 (18.0)	2	5 (8.6)	7 (28.1)	2	7 (11.8)
0.6	4 (17.2)	2	6 (8.0)	7 (28.9)	2	8 (12.0)
0.7	4 (17.0)	3	14 (8.0)	6 (28.8)	2	6 (12.0)
0.8	4 (17.0)	2	5 (8.0)	5 (27.0)	2	10 (12.2)
0.9	4 (17.0)	2	15 (8.0)	5 (27.2)	2	7 (12.5)
1.0	4 (16.8)	2	20 (8.1)	4 (28.5)	3	16 (14.7)

In Problem 2, GMRES iterations decreased significantly while Newton iterations increase. This increase in Newton iterations happened because ALG formulation had more difficulty to enforce the volume change imposed, where two or three Uzawa iterations have been performed, however, as we observed this did not impact on the overall performance, as shown in Table 3.5. The same behavior took place in Problem 3, where the number of GMRES iterations decreased while there was an increase in the number of Newton steps. However, the ALG formulation still improved the overall performance of the iterative solver, which was the most demanding part during the solution process.

3.4 Effect of tolerance on ALG

We finally assessed the effect of choosing different values in the ALG approach for the tolerance (tol), as detailed in Algorithm 2. Typical values for volumetric changes within the cardiac wall are between 5% and 10% due to the intravascular blood flow, as demonstrated experimentally in Yin et al. (1996).

Although tol is a tolerance for the local volumetric change restriction within a finite element, given by $|\tilde{J} - 1|$, we used the value of 0.05 for it since it resembles typical volume changes in cardiac tissue. We note however that the choice of tol is very important and could result in improved performance or better results in terms of enforcing incompressibility. Therefore, we carried out an experiment to study its effect on these features (linear solver time and *error*).

Table 3.7 shows the results of Problem 3 simulations for $\kappa = 100$ kPa with different values for the ALG algorithm tolerance (tol). In one hand the results shows that increasing this tolerance we get more volumetric changes and thus higher values for the *error* in contrast with a shorter time spent by the linear solver with block and nodal AMG preconditioners, since the ALG converges more quickly. On the other hand, when stricter values for tol are used, such as 0.02 or 0.01, smaller volume changes are observed together with smaller values for the *error*. However, additional iterations of the ALG algorithm are required for convergence which in turn results in longer execution time.

Table 3.7: Effect of the tolerance (tol) on the error and on the linear solver time using ALG using the block (B-AMG) and nodal (N-AMG) preconditioners.

ALG tol	$error_{epi}$ (%)	$error_{endo}$ (%)	B-AMG (s)	N-AMG (s)
0.01	0.36	0.13	6090	1619
0.02	0.77	0.46	5654	1544
0.05	1.88	1.39	5678	1281
0.10	3.48	2.85	4083	1108

3.5 Discussions

Our results show that the ALG formulation combined with an efficient preconditioner, such as an AMG preconditioner evaluated here both with the block and nodal versions, brought a significant gain of performance in all experiments carried out within the cardiac mechanics benchmark suite. In addition, the ALG approach enabled to control the volume change *a priori*, that is, a tolerance is chosen before the simulation and the ALG formulation with the Uzawa algorithm guarantees that this volume change will be respected. Without the Augmented Lagrangian it is necessary to choose a value of κ , perform the simulation and only after the simulation the volume change can be verified to decide if this volumetric change is acceptable or not.

With respect to the AMG preconditioners, a detailed comparison of the block and nodal AMG preconditioners for cardiac mechanics was presented. Both preconditioners were efficient and robust for the cardiac mechanics benchmark problems, and they converged in a similar number of iterations. Increasing the problem size (by refining the meshes) confirmed the robustness of both preconditioners, keeping a constant number of iterations. However, the nodal preconditioner proved to be more efficient in terms of total execution time, even in case where the block preconditioner converged in fewer iterations. This result is somewhat non-intuitive, and we have explored a wide range of parameter settings in the PETSc solver in order to improve the computational performance of the block preconditioner. Although tuning solver parameters yield slight performance increases for certain cases, the conclusion remains that the nodal preconditioner is more efficient in terms of computational time.

4 Uncertainty quantification in passive filling simulations

This chapter presents results for experiments aimed to study how geometrical uncertainties are propagated through a model of passive cardiac mechanics. We hypothesize that uncertainty in wall thickness is at least as important as uncertainty in constitutive parameters, and test this hypothesis by performing UQ and sensitivity analysis for passive inflation of an idealized left ventricle. The relatively simple case of a passive LV was chosen to limit the complexity and number of parameters in the model, and thereby facilitate a quantitative study and interpretation of the results. The results presented in this chapter were published in the work Campos et al. (2019).

4.1 Settings

The parameterized LV geometry described in section 2.4.2 is used, where the wall thickness may be varied through the domain to create a patient-specific model. The baseline values for the helix angles of the fiber orientation considered in this work are: $\alpha_{endo} = 50^\circ$, $\alpha_{epi} = -50^\circ$, $\beta_{endo} = -65^\circ$ and $\beta_{epi} = 25^\circ$, which are based on the values used by Rodríguez-Cantano et al. (2019).

In order to reproduce the LV passive filling phase, a pressure is applied to the endocardium surface increasing from 0 to 2 kPa with steps of 0.2 kPa, as similarly used by Choi et al. (2010); Shavik et al. (2017) and Gao et al. (2017). On the epicardial surface we assume homogeneous Neumann boundary conditions (i.e. stress free), while for the basal plane ($z = 0$ cm) we apply the following Dirichlet boundary conditions: all points are fixed in z -axis, and the epicardium points on the base plane are fixed in all directions, as used by Shavik et al. (2017) and similarly in Land et al. (2015).

The UQ and SA analyses in this work were performed using the ChaosPy toolbox. The gPC was created via collocation method, where the model realizations were obtained using the solver described previously. The Sobol sensitivity indices were also computed

from the constructed gPC via ChaosPy.

4.2 Quantities of interest

Six quantities of interest (QoI) were considered in the present study: base and apex deformed wall thickness, the cavity volume, the ventricular torsion and mean fiber stress and strain. Next we specify the definition and calculation of each QoI in more detail.

The deformed wall thickness at the base and apex are quantified by the ratio of deformed (end-diastolic) to undeformed (reference) wall thickness. It is defined by

$$W_D = \frac{\sqrt{(p_{epi}^\Omega - p_{endo}^\Omega)^2}}{\sqrt{(p_{epi}^{\Omega_0} - p_{endo}^{\Omega_0})^2}}, \quad (4.1)$$

where the numerator represents the distance between a point in the epicardium p_{epi}^Ω and a point in the endocardium p_{endo}^Ω at the deformed configuration; the denominator is the distance between a point in the epicardium $p_{epi}^{\Omega_0}$ and a point in the endocardium $p_{endo}^{\Omega_0}$ at the reference configuration.

The *cavity volume* is the volume of the left ventricle cavity at the end of the passive filling, which is the volume between the endocardium surface in the deformed configuration and the basal plane.

The *normalized LV torsion*, T , describes the twist undergone by the left ventricle at the end of the passive filling. This measure is based on the rotation between basal and apical slices, as shown in Figure 4.1(a). It was computed as in Shavik et al. (2017) through

$$T = \frac{(\phi_{apex} - \phi_{base})(\rho_{apex} + \rho_{base})}{2D}, \quad (4.2)$$

where ρ_{apex} and ρ_{base} are the mean radius of the basal and apical slices, respectively, and D is the distance between the slices. In order to ensure that the slice diameter is not zero, we chose $D = 5$ cm, which is smaller than the long axis. Also ϕ_{apex} and ϕ_{base} are the rotation angles at apical and basal slices. Points on endocardial and epicardial surfaces were used to compute an average value of T , due to the variation of twist across the wall (Shavik et al., 2017).

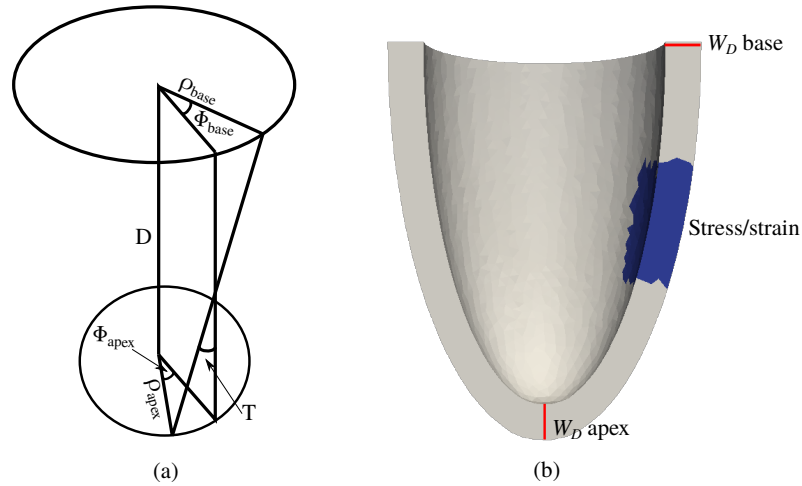


Figure 4.1: Quantities of interest. (a) Left ventricular torsion sketch adapted from Shavik et al. (2017) with circles representing the basal and apical slices. (b) Measured positions for W_D at the apex and base, mean fiber stress and strain at segment 12 (highlighted in blue).

Finally, the *fiber stress* σ_f and *fiber strain* e_f are computed using

$$\sigma_f = \mathbf{f}^T \boldsymbol{\sigma} \mathbf{f}, \quad (4.3)$$

$$e_f = \mathbf{f}_0^T \mathbf{E} \mathbf{f}_0, \quad (4.4)$$

where $\boldsymbol{\sigma}$ is the Cauchy stress tensor, \mathbf{E} is the Green-Lagrange strain tensor, \mathbf{f}_0 is the reference fiber direction and \mathbf{f} is the deformed fiber direction. To simplify the analysis it is useful to define scalar output quantities, and we therefore computed the mean stress and strain over the AHA segment 12 (blue region in Figure 4.1(b)), which was considered as a reference segment in the experiments described next.

4.3 Uncertain inputs and experiments

SA and UQ analyses were performed for a series of experiments considering uncertainties in wall thickness and in the material parameters in (2.14), to assess the impact of geometry on QoIs. For material parameter uncertainty we considered global, uniform parameters, while the uncertain wall thickness was applied for different regions. Initially we used the same uncertain wall thickness value for all segments, resulting in LV geometry samples with uniform thickness throughout the ventricle (Experiment 1).

Additional experiments were performed using more realistic geometries, where the wall thickness was allowed to vary from segment to segment. In order to simplify the analysis we applied the wall thickness uncertainty in smaller regions of the ventricle, which were chosen to be similar to a pathological case of asynchronous electrical activation (Experiments 2 and 3). The selected segments correspond to the lateral wall, which according to Smiseth and Aalen (2019) in case of asynchronous electric activation of the left ventricle, such as in patients with left bundle branch block (LBBB), tends to become thicker as a result of the increased workload due to out of phase contractions of parts of the left ventricle. This leads to an asymmetric LV wall thickness distribution, which we represent here with uncertainty in the lateral region.

Figure 4.2 presents the regions where wall thickness was considered as uncertain with colored segments, where (a) represents the first experiment with constant wall thickness and (b) and (c) represents the thickness variability in different segments of the LV lateral region reproducing pathological conditions.

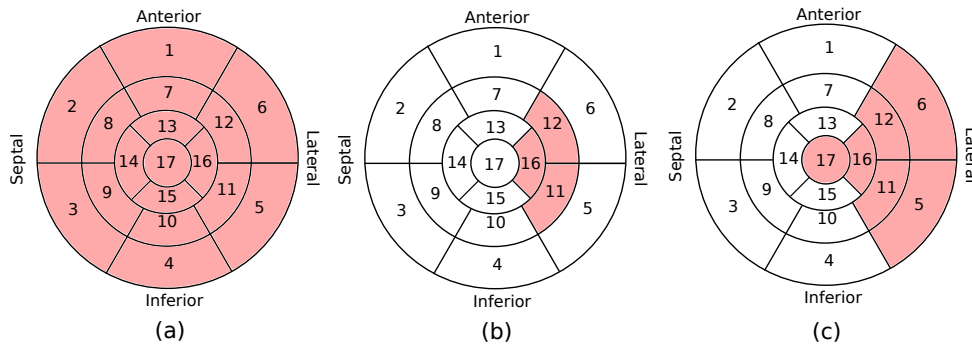


Figure 4.2: 17 AHA segments diagrams representing the three experiments performed, with the colored segments indicating where the wall thickness was considered as uncertain. (a) Experiment 1: uncertain constant wall thickness. (b) Experiment 2: uncertainty in medial-lateral and apical-lateral regions. (c) Experiment 3: adding uncertainty in basal-lateral and apical-lateral segments.

The baseline wall thickness values for all segments are reported in Table 4.1, which were extracted from Bai et al. (2015), for healthy patients.

Table 4.1: Baseline values of the left ventricle wall thickness for each AHA segment reported by Bai et al. (2015).

Segment	Region	Wall thickness (cm)
1	Basal anterior	0.621
2	Basal anteroseptal	0.638
3	Basal inferoseptal	0.623
4	Basal inferior	0.582
5	Basal inferolateral	0.538
6	Basal anterolateral	0.666
7	Mid anterior	0.640
8	Mid anteroseptal	0.706
9	Mid inferoseptal	0.841
10	Mid inferior	0.664
11	Mid inferolateral	0.594
12	Mid anterolateral	0.692
13	Apical anterior	0.547
14	Apical septal	0.619
15	Apical inferior	0.540
16	Apical lateral	0.587
17	Apex	0.437

Figure 4.3 shows geometrical samples generated in the third experiment, where it is possible to see the variability of wall thickness in the lateral region. Note that although the wall thickness of some segments such as 8, 9 and 14 were not considered as uncertain, they are affected by the neighboring segments during the generation of the LV sample, as can be noticed in geometrical sample #76.

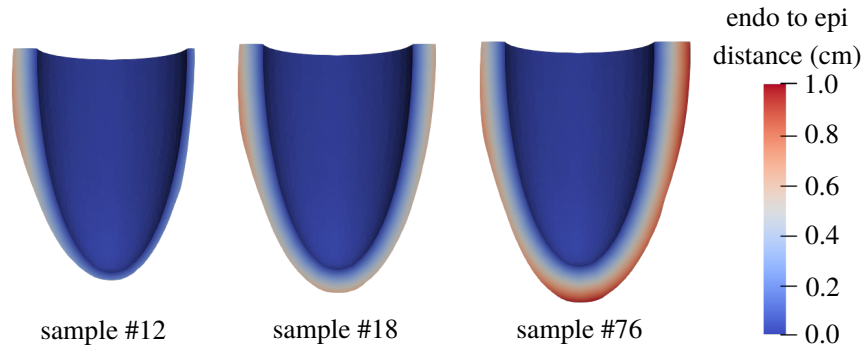


Figure 4.3: Long axis section of geometrical samples used in the third experiment. Color maps represents the endocardial to epicardial distance.

An overview of the uncertain input parameters is shown in Table 5.1, where the chosen probability distributions and ranges of uncertainty are presented. For the material parameters and fiber angles, we chose the distributions in agreement with Osnes and Sundnes (2012) and Rodríguez-Cantano et al. (2019), using a coefficient of variation (COV) of 15%. The coefficient of variation is the ratio between standard deviation (STD) and mean values: $COV = 100 \cdot \frac{Std}{Mean} \%$ that provides information about the variability of some quantity. The LV wall thickness was also considered as an uncertain model input, through a scalar random variable with normal probability distribution using 15% and 30% for COV, representing a range of healthy and pathological variabilities, respectively. The chosen ranges of variability are in agreement with values reported by Bai et al. (2015) and Prinzen et al. (1995).

Table 4.2: Model inputs considered as uncertain.

Model input	Unit	Distribution	Mean	COV
C	kPa	Lognormal	1.1	15%
b_f		Normal	6.6	15%
b_t		Normal	4.0	15%
b_{fs}		Normal	2.6	15%
Angle α_{endo}	degrees	Normal	50	15%
Angle α_{epi}	degrees	Normal	-50	15%
Angle β_{endo}	degrees	Normal	-65	15%
Angle β_{epi}	degrees	Normal	25	15%
Bulk modulus (κ)	kPa	Normal	100	15%
Wall thickness (wt)	cm	Normal	0.64	15% / 30%

A second order generalized polynomial chaos was used in these analyses, as used in Osnes and Sundnes (2012), which was constructed via collocation method using $3P$ samples, with P computed through (2.77). The procedure used to select this settings is described in the next section. Mean and standard deviation were computed for the quantities of interest through gPC in order to assess the uncertainty propagation, and the parameter sensitivities were assessed by computing the main and total Sobol sensitivity indices for each variable.

4.4 Surrogate model calibration

Using Experiment 1 settings, polynomial chaos expansions with orders between $d = 1$ and $d = 4$ with samples size between $N_s = P$ to $N_s = 3P$ were generated and UQ analysis was carried out with COV = 15% for all uncertain inputs. Table 4.3 presents the maximum relative error ϵ_r for the variance and the maximum absolute error ϵ_a for the total Sobol indices, as described in Section 2.9.5, using different number of samples, where the notation $\epsilon_r(1,2)$ was used to denote the error between the polynomial orders 1 and 2, while $\epsilon_r(2,3)$ is the error between orders 2 and 3, and so on.

Table 4.3: Maximum relative error (reported as %) between all quantities of interest for variance and total Sobol sensitivity indices when the polynomial order and the number of samples are varied.

Number of samples N_s	Variance error (%)			Sobol indices error (%)		
	$\epsilon_r(1,2)$	$\epsilon_r(2,3)$	$\epsilon_r(3,4)$	$\epsilon_a(1,2)$	$\epsilon_a(2,3)$	$\epsilon_a(3,4)$
P	15370.42	86.77	49.25	70.88	51.77	29.64
2P	28.20	31.98	27.37	10.40	10.80	8.5
3P	30.61	5.19	5.07	5.24	4.68	4.73

From the results we found that sufficient accuracy was obtained with a polynomial degree $d = 2$ and $N_s = 3P$ for the experiments. For instance, for the setup used in Experiment 1 the errors between $d = 2$ and $d = 3$ using $3P = 198$ samples were 5.19% for the variance and 4.68% for the total Sobol sensitivity indices. Additionally, since the errors did not decay significantly using polynomial orders 3 and 4, a second order polynomial chaos was used for the UQ analyses presented in this work.

Table 4.4 presents Err_{LOO} and Q^2 from the Leave-One-Out cross validation test, for each quantity of interest considered in the experiment, where Q^2 was greater than 0.9 for all quantities, except W_D Apex. The results using second order polynomial chaos and $3P$ samples were considered satisfactory and, therefore, this setting was adopted for the following experiments.

Table 4.4: Leave-one-out error and Q^2 coefficient for each QoI.

QoI	Err_{LOO}	Q^2
W_D Base	4.8064×10^{-5}	0.9434
W_D Apex	9.4643×10^{-5}	0.7793
Cavity Volume	2.2793×10^{-2}	0.9992
Torsion	5.9910×10^{-3}	0.9765
Stress	3.4443×10^{-2}	0.9954
Strain	1.1132×10^{-6}	0.9987

4.5 Preliminary experiment

A preliminary experiment similar to the one presented by Rodríguez-Cantano et al. (2019) was performed to compare the results with respect to other studies in the context of SA and UQ for cardiac mechanics. In this experiment, the parameters from Guccione model (C , b_f , b_t and b_{fs}), fiber angles, and κ were considered as uncertain with $\text{COV} = 15\%$ and a LV geometry with constant wall thickness of 0.64 cm was used. Note that in this first experiment the uncertainty in geometry was not considered. The results showed that the parameter C , related to material stiffness, presented the highest Sobol main sensitivity index, as shown in Figure 4.4. This result is in agreement with findings reported by Osnes and Sundnes (2012) and Rodríguez-Cantano et al. (2019).

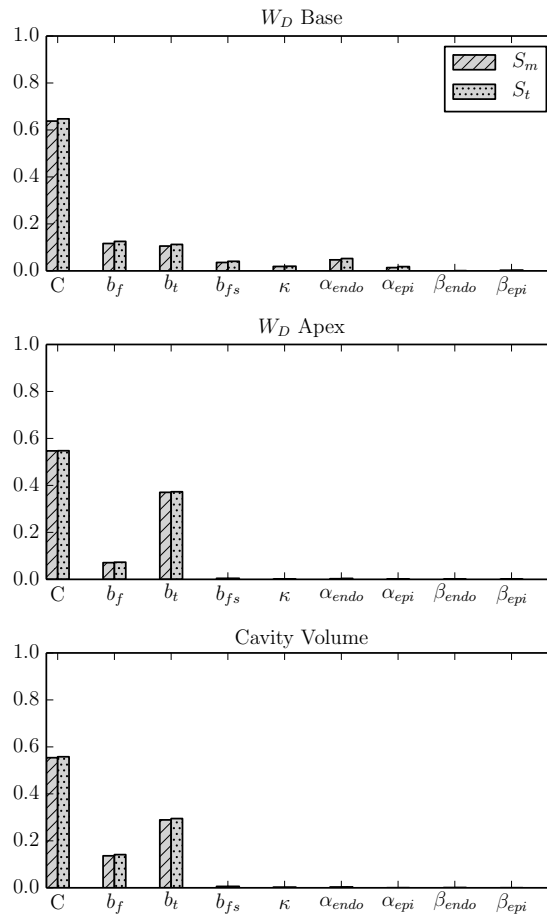


Figure 4.4: Main (S_m) and Total (S_t) Sobol sensitivity indices for the preliminary experiment.

4.6 Experiment 1: Constant wall thickness

The first experiment considered all model inputs from Table 5.1 as uncertain and considered the same uncertain wall thickness in all LV segments, resulting in geometrical samples with constant thickness throughout the ventricle.

Table 5.3 presents the uncertainty propagation for the chosen quantities of interest, through the values of mean, standard deviation and coefficient of variation. The QoI most affected by uncertainties in the chosen model inputs were torsion, stress and strain, where the variability with respect to the mean reached 58%, 64% and 27%, respectively. As expected, increasing the uncertainty range of wall thickness led to a higher variability in all QoIs, but the increase was particularly pronounced for the stress, for which the variability more than doubled.

Table 4.5: Experiment 1: uncertainty propagation for each quantity of interest, considering 15% and 30% of uncertainty for wall thickness and 15% for the other model inputs.

QoI	Mean		STD		COV	
	15%	30%	15%	30%	15%	30%
W_D Base	0.82	0.81	0.03	0.04	4.0	5.0
W_D Apex	0.91	0.90	0.02	0.03	3.0	4.0
Cavity volume	81.65	82.49	5.63	7.33	7.0	9.0
Torsion	1.23	1.35	0.59	0.78	48.0	58.0
Mean stress	10.83	12.68	2.92	8.11	27.0	64.0
Mean strain	0.16	0.16	0.03	0.04	19.0	27.0

Figure 4.5 shows the Sobol sensitivity indices for each QoI, considering 15% and 30% of uncertainty in wall thickness and 15% in the other inputs. The striped bars represent the main sensitivity indices S_m and the dotted bars are the total sensitivity indices S_t . From the main Sobol sensitivity indices it may be noticed that the material stiffness parameter C and wall thickness (wt) are the most sensitive model inputs. When the uncertainty range is 15% for all model inputs, C is the input with the highest impact on W_D apex, W_D base and cavity volume, where it is responsible for about 40% of the total variability. For strain measures, C is as important as wall thickness and b_f , while mean stress is very sensitive to wall thickness. Only in torsion a different behavior was observed, where b_t

is responsible for 40% of the resultant variability. However, when the uncertainty range of wall thickness is 30% all quantities, except torsion, are very sensitive to this input. Furthermore, the low total sensitivity indices of κ , b_{fs} and fiber angles indicate that these inputs can be fixed to an arbitrary value within their range of uncertainty, without much impact on the results.

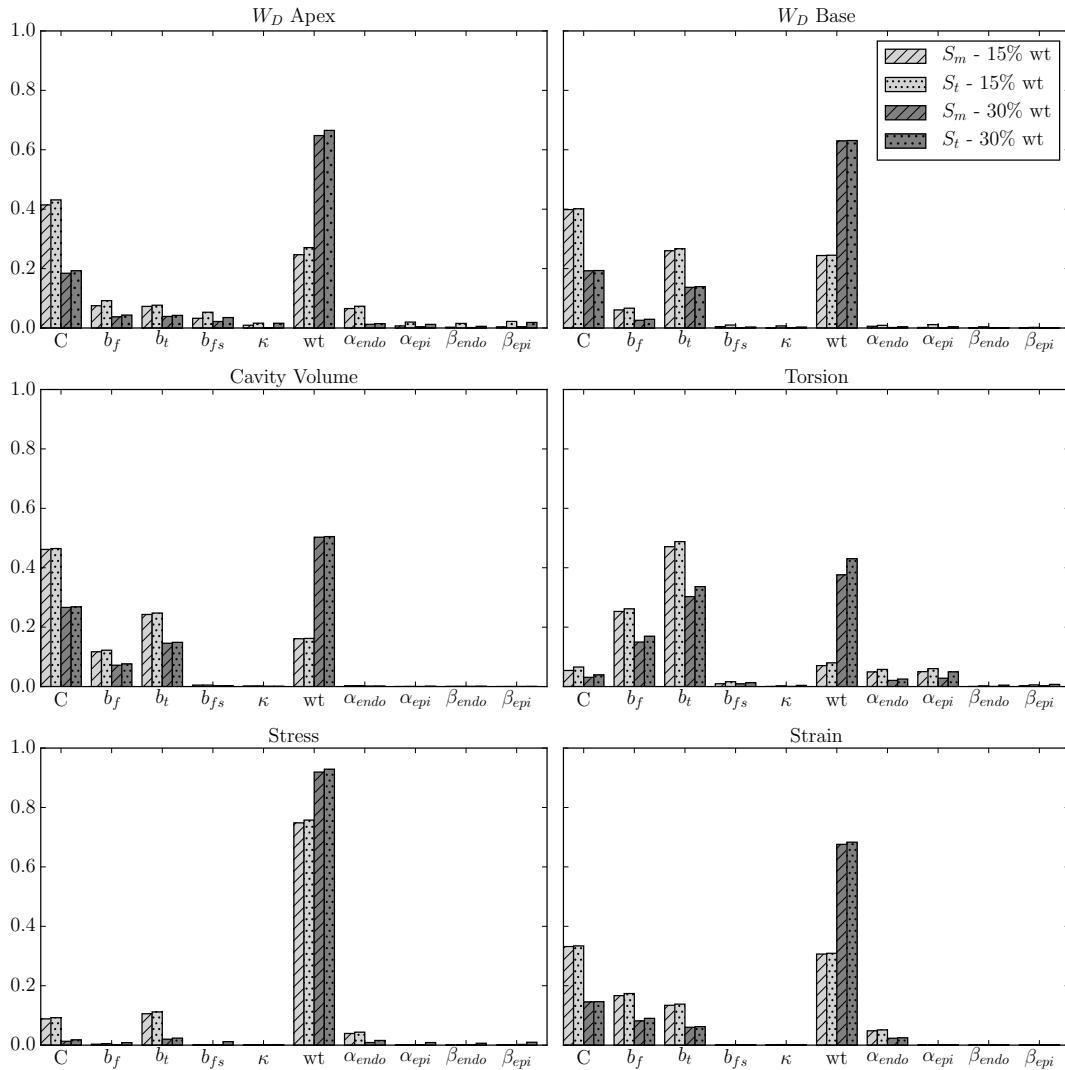


Figure 4.5: Experiment 1: Main (S_m) and Total (S_t) Sobol sensitivity indices for each quantity of interest considering 15% and 30% of uncertainty for wall thickness and 15% of uncertainty for the other parameters.

4.7 Experiment 2: Uncertainty in medial-lateral and apical-lateral regions

Now the uncertainty in wall thickness is considered only in a few segments, instead of in the entire left ventricle. In this experiment three segments have the same uncertain value: one apical and two medial segments of the lateral region, while the rest of the segments are fixed to the mean values reported in Table 4.1.

As shown in Table 4.6, torsion, stress and strain are again the quantities most affected by model input uncertainty. In this experiment, it was observed that mean stress and strain measures (at the selected segment 12) varied less than in the first case.

Figure 4.6 shows that wall thickness has a high impact in torsion, stress and strain. Also, according to the S_m index, wall thickness has a small impact on the W_D apex and base, which is likely because these quantities are measured outside the region of uncertain wall thickness.

Table 4.6: Experiment 2: uncertainty propagation for each quantity of interest, considering 15% and 30% of uncertainty for wall thickness and 15% for the other model inputs.

QoI	Mean		STD		COV	
	15%	30%	15%	30%	15%	30%
W_D Base	0.81	0.81	0.025	0.028	3.1	3.5
W_D Apex	0.86	0.86	0.029	0.027	3.4	3.1
Cavity volume	82.05	82.18	5.222	5.321	6.4	6.5
Torsion	1.87	2.04	0.849	1.368	45.4	67.2
Mean stress	11.56	12.63	2.573	5.658	22.3	44.8
Mean strain	0.16	0.17	0.029	0.039	17.6	23.2

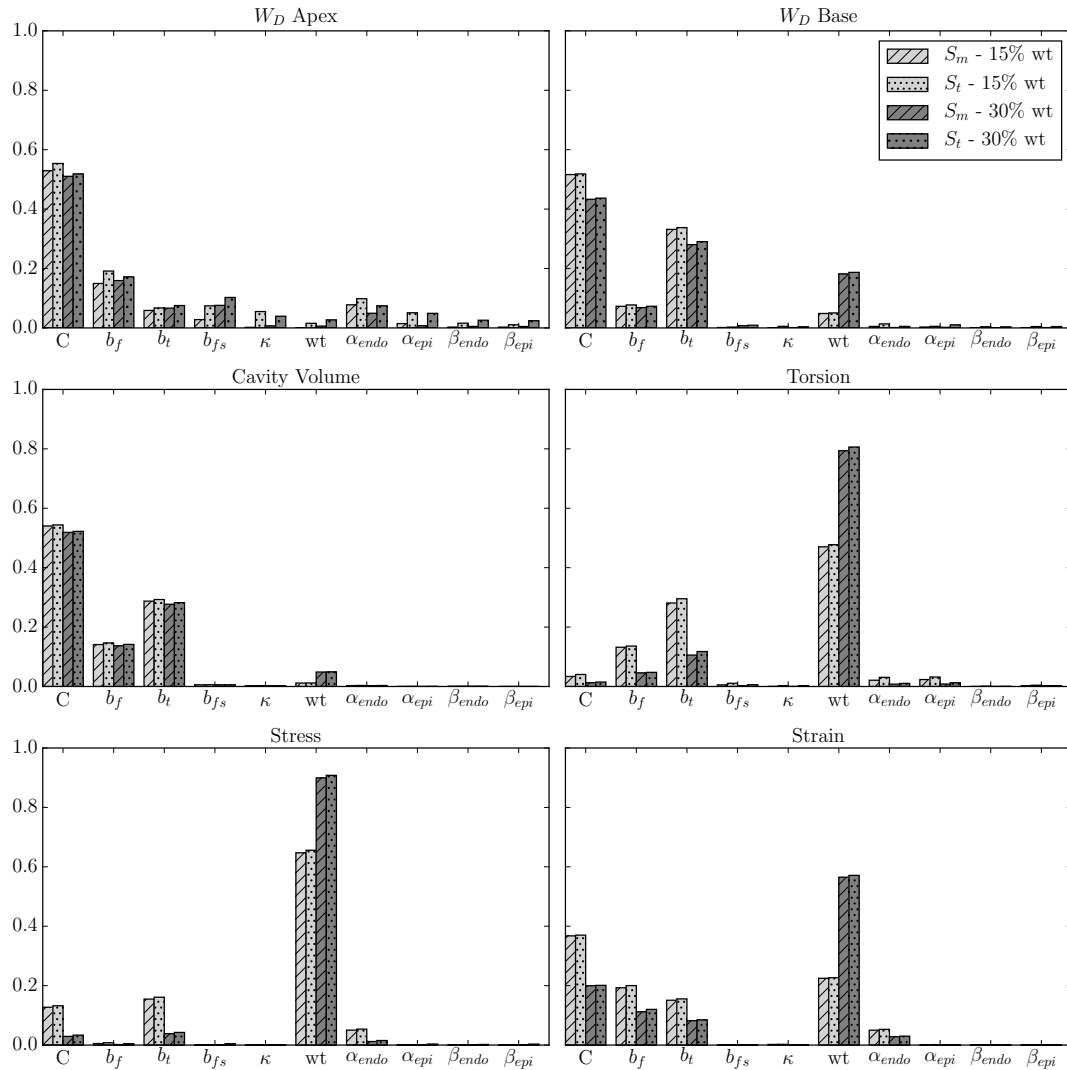


Figure 4.6: Experiment 2: Main (S_m) and Total (S_t) Sobol sensitivity indices for each quantity of interest considering 15% and 30% of uncertainty for wall thickness and 15% of uncertainty for the other parameters.

4.8 Experiment 3: Including uncertainty in apex and basal-lateral region

In the last experiment we increased the region of uncertainty in wall thickness by adding the apex segment and two basal segments to the previous setting (b) (see Fig. 4.2). This rendered the wall thickness in the entire lateral region as uncertain, as shown in Figure 4.2(c).

The behavior was similar to the previous experiment, where torsion, stress and strain are the most impacted quantities. That is, when 15% uncertainty is considered for all inputs, torsion and stress were more influenced by wall thickness; and strain by C and wall thickness. Therefore, Figure 4.7 presents only the Sobol indices for the quantities where the changes were significant with respect to the previous experiment. Note that W_D for apex and base were more impacted by wall thickness, because now the wall thickness varies in the basal and apical segments. Furthermore, when the wall thickness uncertainty range is 30% it dominates the variability for all quantities, except for cavity volume, as in the previous experiment.

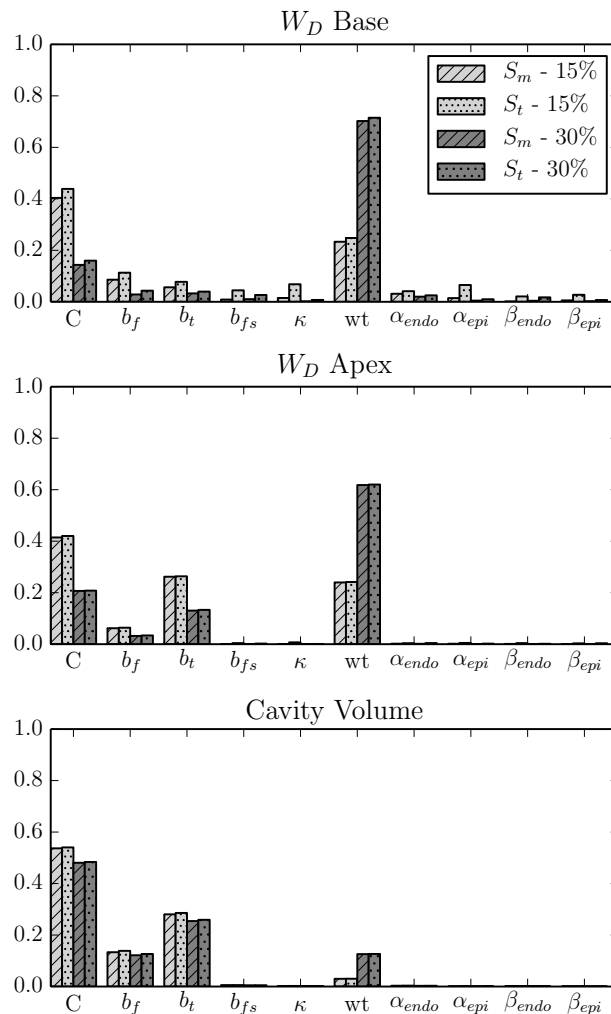


Figure 4.7: Experiment 3: Main (S_m) and Total (S_t) Sobol sensitivity indices for torsion, W_D base and apex considering 15% and 30% of uncertainty for wall thickness and 15% of uncertainty for the other parameters.

4.9 Global effects on stress and strain

For simplicity, fiber stress and strain measures observed in the previous experiments were considered as the mean value over all the elements of the segment number 12 in the LV medial-lateral region. Here, to assess the spatial variation of stress and strain, the mean value of these quantities over each of the 17 segments was computed from the experiment 3 with 30% uncertainty for wall thickness and 15% uncertainty for the other parameters.

Figure 4.8 presents uncertainty propagation for these mean values of all segments. In basal segments lower values of the mean stress and strain are observed, whereas in the medial and apical segments the mean stress is higher. Note that, as expected, the deviation was higher in the segments (and also in their neighbors) where uncertainty in wall thickness was considered in experiment 3 (see Figure 4.2(c)). The behavior of mean stress and strain at the apical segment are similar, where more deviation was observed.

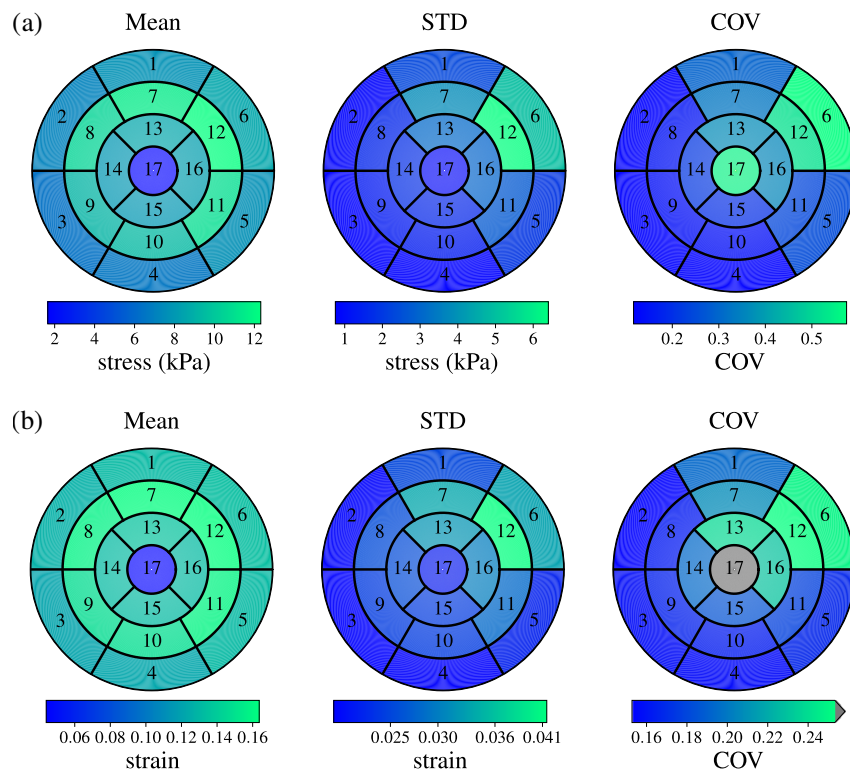


Figure 4.8: Bull's eye plot of the uncertainty propagation in mean fiber (a) stress and (b) strain for all segments. The uncertainty range was 30% for wall thickness and 15% for the other parameters.

4.10 Discussions

The goal of the present chapter was to study the importance of uncertainty in LV wall thickness, material properties and fiber orientation in cardiac mechanics outputs. An image-based personalized geometrical model is usually considered an important component of a patient-specific cardiac mechanics model, and such a geometry will include uncertainties from a number of sources. In this work it has been shown, through uncertainty quantification and sensitivity analyses, how these uncertainties can impact important quantities of interest.

A parameterized strategy was applied in the generation of LV geometries, which is based on the 17 AHA segments diagram. This approach enables the construction of geometrical samples with thickness varying throughout the domain using scalar random variables, instead of more complex approaches such as stochastic fields (Biehler and Wall, 2018; Biehler et al., 2015). Furthermore, this strategy allows the use of available data from the literature, as those presented in the work of Bai et al. (2015), for wall thickness variability to generate different geometric models.

A partial verification of our model was performed by running preliminary UQ and SA studies considering uncertainties in material parameters and fiber orientation, and comparing the results with previous works. The results were found to be in agreement with the results reported by Osnes and Sundnes (2012) and Rodríguez-Cantano et al. (2019).

The main finding of the present work is that wall thickness proved to be at least as important as material parameter uncertainty in the majority of the cases. In the first experiment all quantities except torsion, were significantly influenced by uncertainty in wall thickness. As expected, the impact of wall thickness uncertainty becomes more pronounced when the coefficient of variation is increased to 30%, which is in the range of variations seen during pathological conditions, and therefore within the range of expected variation from manual image segmentation. Additionally, in all experiments the coefficient of variation for torsion, mean stress and strain was relevant, achieving large values, as shown in Tables 5.3 and 4.6. Interesting is to note that these are exactly the quantities of interest which were most impacted by changes in wall thickness.

Cavity volume was only significantly affected by wall thickness when it was varied uniformly across the left ventricle, while the regional uncertainty hardly impacted this QoI

at all. Local measures, such as W_D apex and base are mostly influenced by wall thickness when this input varies in the measured location. On the other hand, the assumption of uncertain wall thickness only in the lateral region, which could be relevant for pathological conditions as presented in the work of Prinzen et al. (1995), has a high impact in torsion, which might occur due to asymmetric LV thickness.

The use of different uncertainty range for wall thickness, representing healthy and pathological variability showed the different impacts in the quantities of interest. In the first case material stiffness and wall thickness are the major source of variability in QoI, while in the second scenario wall thickness becomes even more important in the majority of the quantities.

The results of this work suggest that the generation of geometrical models for the left ventricle is an important step in cardiac mechanics simulations for clinical use. For instance, fiber stress was very impacted due to uncertainties in wall thickness, and this is a quantity difficult to be computed from experiments and an accurate way to obtain its value is through patient-specific simulations. Furthermore, fiber stress is an important indicator in cardiac diseases involving remodeling process, where its quantification can guide interventions to reduce abnormal stress. This sheds light on the importance of accurate and robust image segmentation and measurements for automatic or semi-automatic mesh generation. When considering pathological cases, where a remodeling of the LV wall is observed, this is even more important. In summary, this makes the generation of patient-specific geometries for clinical applications even more challenging.

Previous works (Biehler and Wall, 2018) reported that stress is very influenced by uncertainties in wall thickness, where the peak wall stress in abdominal aortic aneurysms is sensitive to variations in wall thickness.

In the context of cardiac mechanics, a study of passive filling simulations varying the wall thickness and curvature of a thick-walled ellipsoid was reported by Choi et al. (2010), where both geometrical aspects impacted significantly the transmural fiber stress and strain. The present work is in agreement with these findings, since the experiments showed wall thickness being responsible for more than 70% of stress variability in all cases. This quantity was the one most strongly affected by wall thickness, which is to be expected from fundamental mechanical considerations and the definition of stress as force per area. Furthermore, and also in line with basic mechanical considerations, the impact

on stress is local, in the sense that a region of uncertain wall thickness will mostly impact the stress in the same region. Strain is also significantly impacted due to uncertainties in wall thickness, mainly when the uncertainty range is 30%.

5 Uncertainty quantification of left ventricle simulations during the cardiac cycle

This chapter presents the results for uncertainty quantification analysis in left ventricle simulations during the full cardiac cycle. The simulations take into account uncertainties in the ventricular geometry, fiber orientation, constitutive parameters, active stress magnitude, and in parameters of the coupled circulatory model. Uncertainty quantification and sensitivity analyses are performed to determine how important quantities of clinical interest, such as ejection fraction, pressure, and stress, are affected by these uncertainties and which model inputs have the highest impact on each computed quantity of interest. The results presented in this chapter are going to be submitted as a manuscript to a special issue on Uncertainty Quantification in Cardiac Modelling and Simulation from the Philosophical Transactions of the Royal Society A.

5.1 Settings

The cardiac tissue deformation is described by the quasi-static mechanical problem presented in (2.11), using the Guccione et al. (1995) constitutive model to describe the passive behavior of the tissue and the Kerckhoffs et al. (2003) model to represent the active contraction. To represent the ventricular activity during the cardiac cycle, a time varying pressure boundary condition is applied to the endocardial surface. This pressure is determined from the lumped parameter model presented in Section 2.6, which represents the circulatory system.

The parameterized LV geometry described in section 2.4.2 is used, where the wall thickness may be varied through the domain to create a patient-specific model. On the epicardial surface we assume homogeneous Neumann boundary conditions (i.e. stress free), while for the basal plane ($z = 0$ cm) we apply the following Dirichlet boundary conditions: all nodes are fixed in z -axis, and the epicardium nodes on the base plane are

fixed in all directions, as used by Shavik et al. (2017).

5.2 Experiments

Uncertainty quantification and sensitivity analyses were performed for left ventricle simulations during the cardiac cycle in a series of four experiments. A cardiac cycle of 900 ms was considered, where the active stress was applied simultaneously in all points at time 200 ms. Uncertainties were considered in the parameters of the constitutive model, regional wall thickness, fiber angles, maximum value for active stress, and in the parameters of the circulatory model. The uncertain inputs were described through Normal distributions with 5% coefficient of variation (COV), where $\text{COV} = 100 \cdot \frac{\text{Std}}{\text{Mean}} \%$.

The geometrical samples were constructed using the parameterized approach based on the 17 AHA segments. The long and short axis lengths were fixed to 60 mm and 40 mm, respectively. The uncertainty in wall thickness was considered through a scalar random variable. For this, a multiplicative factor was introduced to change the wall thickness baseline value of each AHA segment as follows:

$$s_i = s_i * (1 + wt_s), \quad i = 1, \dots, 17. \quad (5.1)$$

where s_i represents the baseline value for wall thickness in the i_{th} segment and wt_s is a sample of the random variable wt .

Table 5.1: Uncertain model inputs, described through Normal distribution with 5% for the coefficient of variation.

Model input	Unit	Mean value	Model input	Unit	Mean value
C	kPa	0.66	Aortic valve resistance (R_{ao})	kPa·ms·ml ⁻¹	3.85
b_f		6.6	Peripheral resistance (R_{per})	kPa·ms·ml ⁻¹	140
b_t		4.0	Venous resistance (R_{ven})	kPa·ms·ml ⁻¹	1.4
b_{fs}		2.6	Mitral valve resistance (R_{mv})	kPa·ms·ml ⁻¹	1.75
Wall thickness factor (wt)	mm	0	Aortic compliance (C_{art})	ml·kPa ⁻¹	14
Longitudinal fiber angle (α_{endo})	degrees	60	Venous compliance (C_{ven})	ml·kPa ⁻¹	300
Longitudinal fiber angle (α_{epi})	degrees	-60	End-systolic elastance ($E_{es,LA}$)	kPa·ml ⁻¹	0.06
Transverse fiber angle (β_{endo})	degrees	-65	Scaling factor for EDPVR (A_{LA})	kPa	0.05867
Transverse fiber angle (β_{epi})	degrees	25	Exponent for EDPVR (B_{LA})	ml ⁻¹	0.049
Maximum active stress (T_{ref})	kPa	75	Time to end-systole (t_{max})	ms	200
			Time constant of relaxation (τ)	ms	25

Experiment 1: In the first experiment the uncertain inputs were the constitutive parameters of the passive tissue, wall thickness, fiber angles and the maximum

value for active stress, while the parameters for the circulatory model were fixed to reference values. The mean value of wall thickness in all segments s_i of equation (5.1) was 6.4 mm, resulting in simplified LV geometries with constant wall thickness throughout the domain.

Experiment 2: This experiment considers the same set of uncertain inputs as the previous, except for wall thickness. Here, the mean value for wall thickness in each AHA segment s_i followed the baseline values reported in the atlas of Bai et al. (2015) (see Table 4.1) to generate more realistic geometries of the left ventricle.

Experiment 3: In this case the wall thickness uncertainty was considered only in segments of the lateral region which corresponds to the segments 5, 6, 11, 12, 16 and 17 (see Fig. 4.2(c)). Thus, asymmetric uncertainty in wall thickness is considered within the physiological range as presented by Bai et al. (2015). This experiment also adds uncertainty in the parameters of the circulatory model, that is, all parameters presented in Table 5.1 are considered in this analysis.

Experiment 4: The setting of this experiment is same of Experiment 2, but here an increase in the uncertainty of wall thickness is considered. Here we represent errors during the segmentation process as described in the study of Suinesiaputra et al. (2015), where measurements of left ventricular mass or volumes obtained by different groups for the same MR images of patients differ in average by 20% when compared to consensus measurements. Thus, in this experiment we assume a coefficient of variation for wall thickness of 20%, while for all the other uncertain inputs COV was 5%.

5.2.1 Quantities of interest

Some local and global measurements were considered as quantities of interest (QoI) in the analyses. The local measurements were the left ventricle torsion, mean fiber stress and strain in a chosen AHA segment, which were all measured in the early ejection. Global quantities were extracted from the pressure volume (PV) loop: ejection fraction, end systolic pressure and maximal variation of pressure over time.

The normalized *LV torsion* denoted by T describes the twist of the ventricle in some time instant and it is based on the rotation between basal and apical slices. In this work it was considered at the end of the early ejection and was computed as (Shavik et al.,

2017):

$$T = \frac{(\phi_{apex} - \phi_{base})(\rho_{apex} + \rho_{base})}{2D}, \quad (5.2)$$

where ρ_{apex} and ρ_{base} are the mean radius of the basal and apical slices, respectively, and D is the distance between the slices. The rotation angles at apical and basal slices are ϕ_{apex} and ϕ_{base} . Due to the variation of twist across the wall, an average value of T was computed using points on endocardial and epicardial surfaces, as suggested in the work of Shavik et al. (2017).

The *fiber stress* σ_f is calculated using the Cauchy stress tensor $\boldsymbol{\sigma}$ and the fiber direction in its deformed configuration \mathbf{f} :

$$\sigma_f = \mathbf{f}^T \boldsymbol{\sigma} \mathbf{f}. \quad (5.3)$$

And the *fiber strain* e_f is computed through the Green-Lagrange strain tensor \mathbf{E} and undeformed fiber direction \mathbf{f}_0 :

$$e_f = \mathbf{f}_0^T \mathbf{E} \mathbf{f}_0. \quad (5.4)$$

Scalar values of both measures were calculated in order to simplify the analysis, where the average of stress and strain over the AHA segment 12 was considered as QoI in all experiments.

The ejection fraction represents the percentage of blood that is pumped each time the ventricle contracts and characterizes the LV function. It is defined as:

$$EF = \frac{EDV - ESV}{EDV}, \quad (5.5)$$

where EDV is the end diastolic volume and ESV is the end systolic volume.

The maximal rate of change in pressure over time, denoted by dP/dt_{max} , is a common indicator of changes in cardiac contractility and it was obtained through the computation of the first derivative of pressure with respect to time and taking its maximal value. As pressure is obtained at discrete time steps, a first order finite difference scheme was used to compute the derivative. The end systolic pressure was also considered as a QoI, which is the pressure measured in the end of the ejection phase.

5.3 Results

This section presents the results of uncertainty quantification and sensitivity analyses for all experiments. For the sake of compactness, we chose to present and compare only the experiments where relevant differences appear.

5.3.1 Surrogate model calibration

The quality of the surrogate model was assessed using the Leave-One-Out (LOO) cross validation test, as presented in Section 2.9.5. The analyses were performed using second order polynomials chaos constructed with $N_s = 3P$ samples, corresponding to 693 samples for experiment 3 and 198 samples in experiments 1, 2 and 4. Table 5.2 presents Q^2 for the considered quantities of interest in each experiment, where Q^2 from the cross validation test was greater than 0.9 for most of the quantities, except for torsion. Considering a trade-off between computational cost and accuracy of the surrogate model, this setting for the construction of the polynomial chaos was chosen for the experiments presented next.

Table 5.2: Q^2 coefficient obtained by the leave-one-out cross validation test for the QoIs in each experiment.

Experiment	Torsion	σ_f	e_f	ESP	EF	dP/dt_{max}
1	0.92	0.98	0.94	0.99	0.99	0.99
2	0.85	0.98	0.97	0.99	0.99	0.99
3	0.88	0.99	0.99	0.99	0.99	0.99
4	0.75	0.98	0.88	0.96	0.97	0.99

5.3.2 Uncertainty propagation

Table 5.3 presents the uncertainty propagation results, which shows that in Experiment 1 the most impacted quantities of interest were ventricular torsion and EF, with 19.1% and 9.6% of variability, respectively. The outputs fiber stress σ_f , fiber strain e_f and dP/dt_{max} had also a variability greater than 5% considered for the uncertain inputs. Moreover, the end-systolic pressure was the quantity less impacted by the uncertainties.

For Experiment 2, the uncertainty propagation results shows that torsion was also the most impacted quantity with COV= 16%, followed by EF with COV= 13.4%. There was

a significant increase in the variation of EF when compared to the previous experiment. The mean value of torsion increased, while its variability was lower than in Experiment 1. The behaviour for the remaining quantities was similar to the previous experiment.

The most impacted quantities in Experiment 3 were torsion and EF, as in the previous cases. The coefficient of variation for T increased to 21.7%, while for EF it decreased to 10.9%. The variability of fiber stress and fiber strain slightly increased and the remaining observable outputs had similar variability in comparison with experiments 1 and 2, where the COV is close to the one considered in the inputs.

In Experiment 4, which is not shown here, all quantities were very impacted by the uncertainties considered in wall thickness, where the lowest COV was obtained in ESP (10.5%). Note that here the ejection fraction is the most impacted quantity with 36.8% of coefficient of variation.

Table 5.3: Mean value, standard deviation (STD) and the corresponding coefficient of variation (COV) of the quantities of interest for all experiments.

	QoI	Torsion	σ_f	e_f	ESP	EF	dP/dt_{max}
Experiment 1	Mean	7.15	100.55	0.21	95.75	0.59	1171.76
	STD	1.36	7.42	0.01	2.97	0.06	75.25
	COV	19.1	7.40	5.60	3.1	9.6	6.40
Experiment 2	Mean	9.87	112.54	0.22	94.00	0.56	1104.47
	STD	1.58	8.22	0.01	3.94	0.07	71.94
	COV	16.0	7.30	5.30	4.2	13.4	6.5
Experiment 3	Mean	9.73	112.35	0.22	94.18	0.56	1104.71
	STD	2.11	9.06	0.02	3.24	0.06	58.19
	COV	21.7	8.1	7.8	3.4	10.9	5.3
Experiment 4	Mean	10.6	118.59	0.22	91.53	0.51	1101.59
	STD	2.72	31.87	0.02	9.57	0.19	187.71
	COV	25.7	26.9	10.9	10.5	36.8	17.0

To show the uncertainties in volume and pressures curves, we chose experiment 2 as an illustrative case. Figure 5.1 shows the variability of pressure and volume during the cardiac cycle from the 95% prediction interval, where it is notable that end systolic volume is highly impacted by the uncertainties. The most significant change in the pressure profile is the peak value, while in the PV-loop it is possible to observe high variations in the beginning of ejection phase and also at the end of systole, which impacts the ejection fraction. Results for experiment 1 and 3 showed the same patterns as the results of

experiment 2.

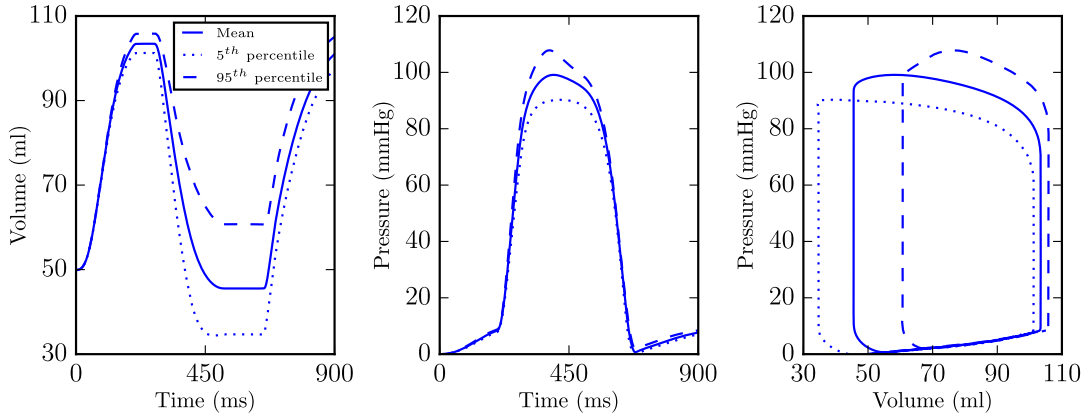


Figure 5.1: Mean value and variations in the 95% confidence interval for volume and pressure profiles as a function of time and PV-loop, respectively, for Experiment 2.

Figure 5.2 shows the density distribution estimated for each quantity of interest in experiments 2 and 4. The distributions are near symmetric in fiber strain and dP/dt_{max} , indicating they could be described by normal distributions, while the remaining quantities presented significant asymmetry. Comparing both experiments, it is clear that variability is higher in Experiment 4, as expected due to the high COV for the parameters, resulting in more dispersion in the curves for this case.

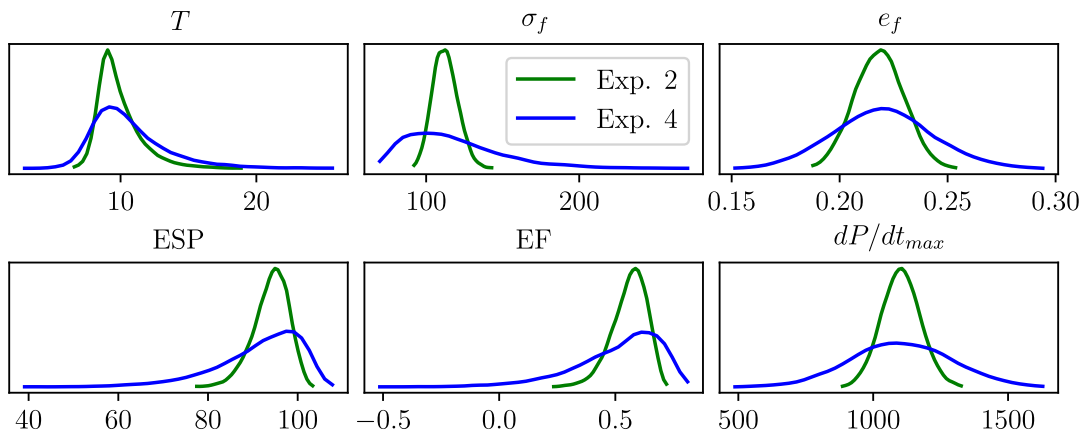


Figure 5.2: Probability densities of QoIs for experiments 2 and 4.

5.3.3 Sensitivity analysis

The Sobol sensitivity indices were computed for all quantities of interest, and the results are shown in Figure 5.3 (top) for Experiment 1. The results show that most outputs

are strongly influenced by wall thickness, while parameters of the passive constitutive model have low impact on the outputs. The magnitude of the active stress, T_{ref} , also has significant impact on the end systolic pressure, ejection fraction and dP/dt_{max} , but a low impact on the other quantities. Variation in fiber angles mainly affects LV torsion and fiber strain.

The time-averaged Sobol sensitivity indices (Figure 5.3 (bottom)) show that the wall thickness and T_{ref} are the input parameters with the highest impact in pressure and volume as a time series. This result confirms the influence of both model inputs in the quantities extracted from the PV-loop, presented in Figure 5.3 (top), such as ESP, EF and dP/dt_{max} . The sensitivity analysis for Experiment 2, where regional differences in wall thickness were incorporated in the geometries, showed a pattern similar to experiment 1, which considers constant wall thickness.

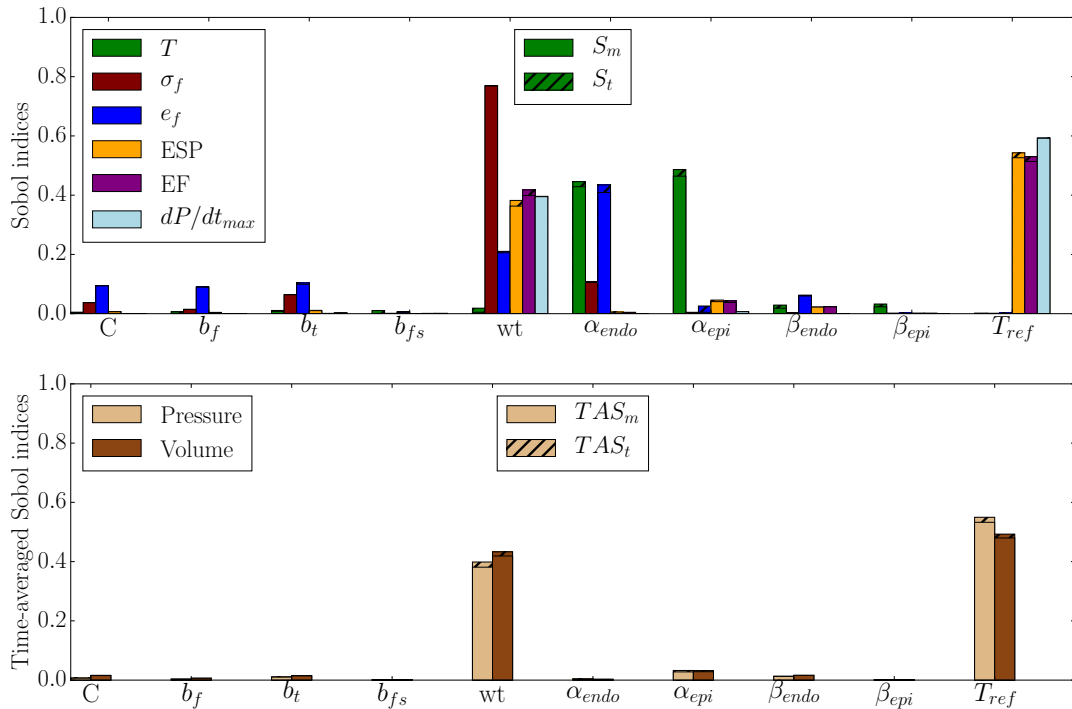


Figure 5.3: Experiment 1: sensitivity analysis with main and total Sobol indices (top) and time-averaged indices (bottom). Striped bars represent the total Sobol indices while the solid bars show the main indices.

Comparing the results of experiment 3 to those of experiments 1 and 2, we note that the impact of T_{ref} in the selected outputs increases. The sensitivity of torsion to wall thickness increased significantly in this case, where this input shows to be as important as

fiber angles. Wall thickness presented the largest Sobol indices for fiber stress and fiber strain. These results show that asymmetric uncertainties in wall thickness may cause more impact on torsion and less impact on EF, ESP and dP/dt_{max} .

The time-averaged Sobol indices in Figure 5.4 (bottom) show that wall thickness and T_{ref} are still the inputs with the highest impact on pressure and volume time series. However, for experiment 3, these quantities were more sensitive to T_{ref} than to wall thickness.

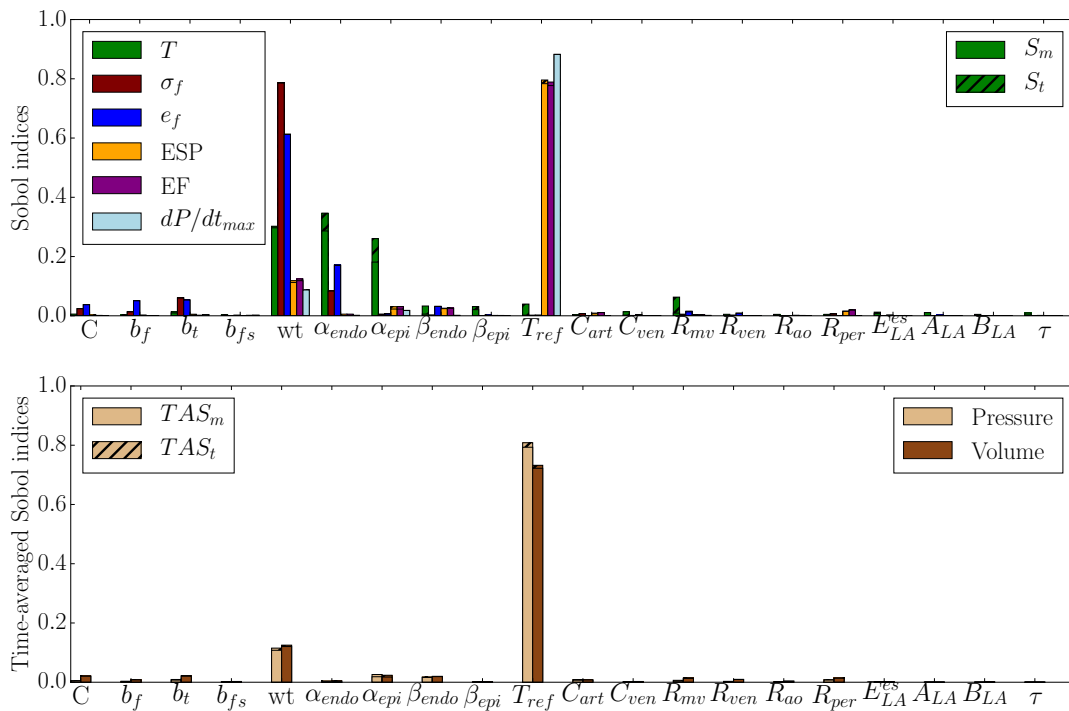


Figure 5.4: Experiment 3: sensitivity analysis with main and total Sobol indices (top) and time-averaged indices (bottom).

In Experiment 4 it was observed that wall thickness dominates the influence in all QoIs, as expected, since a large variation of wall thickness parameter was considered with $COV=20\%$. In this case the Sobol indices for wall thickness were greater than 0.7 for all quantities and about 0.6 for torsion. The fiber angles still have an impact on torsion, whereas the remaining uncertain inputs have low impact on the quantities of interest. The time-averaged Sobol index related to wall thickness was greater than 0.9 for pressure and volume time series.

5.3.4 Stress and strain time series

The previous experiments considered fiber stress and strain as scalar quantities of interest extracted in the beginning of ejection phase at segment 12. Figure 5.5 shows stress and strain time series to analyze the uncertainty of these quantities during the entire cycle.

Figure 5.5(a) presents the mean stress for the whole ventricle over time, followed by the stress time series in each AHA segment. The segments of the medial region presented the largest values of stress and the variability is also larger in medial and apical regions, whereas basal segments presented a lower deviation from the mean. Furthermore, the significant variation is located in the time interval of the ejection phase. Figure 5.5(b) presents the time series for the mean fiber strain, where it can be noted that the more significant variability is also during the ejection phase. The time-averaged Sobol indices for these quantities showed that wall thickness and T_{ref} are the uncertain inputs with the highest impact on both time series.

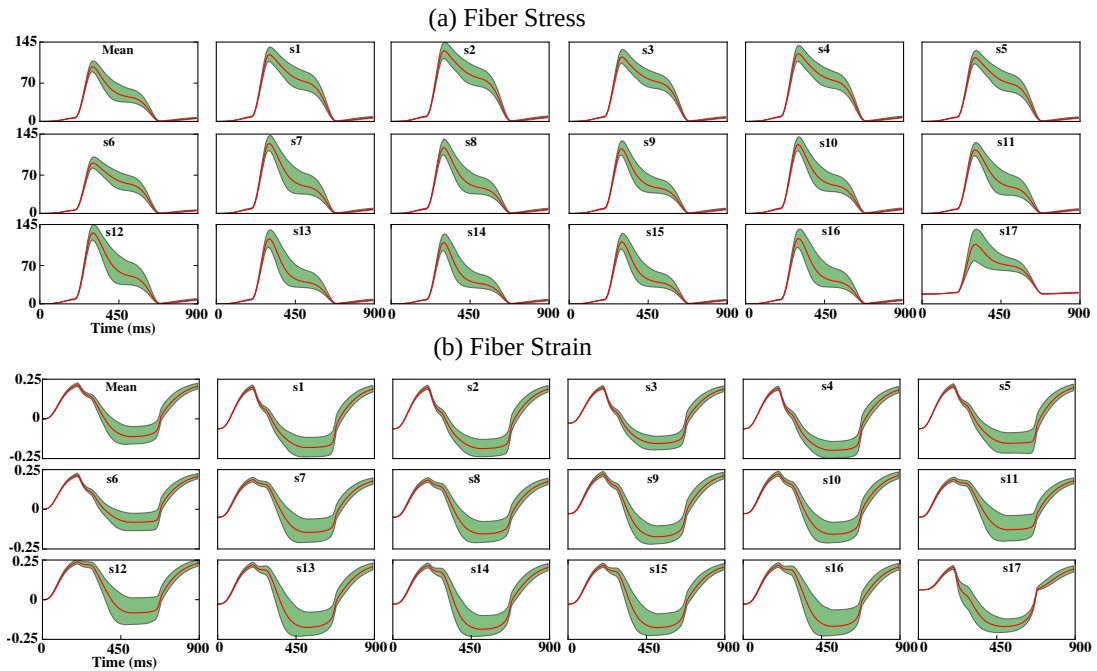


Figure 5.5: Experiment 2: uncertainty propagation for (a) stress and (b) fiber strain time series in each AHA segment s_i , for $i = 1, \dots, 17$. The figures also show the mean stress and fiber strain over the whole ventricle (top left).

5.4 Discussions

The aim of this chapter was to study the impact of uncertainties in different inputs and also to determine the most important parameters with respect to the outputs of a cardiac mechanics model for full cycle simulations. The model parameters considered in this study were geometry (regional wall thickness), fiber orientation, constitutive model properties, active stress magnitude and the parameters of the circulatory model used to reproduce the time varying pressure in the LV cavity. Then, uncertainty quantification and sensitivity analyses were performed to assess the impact on quantities that are important in clinical use.

A parameterized approach based on the 17 AHA segments diagram was used to incorporate uncertainties in the LV geometry, through the wall thickness value in each segment. This approach allows changes in the left ventricle shape based on quantities with a direct clinical interpretation. Uncertainties can be incorporated in the entire ventricle to represent uncertainties for instance in image segmentation, or regionally to represent pathology or some region of increased variability. Furthermore, this strategy enables the use of scalar random variables for wall thickness instead of random fields (Rodríguez-Cantano et al., 2019; Biehler and Wall, 2018), which are more complex to be performed. LV wall thickness measurement in the 17 AHA segments can be found in the literature, as in the atlas developed by Bai et al. (2015) that present the wall thickness values and the variability among patients for each AHA segment.

All uncertain inputs were described by normal distribution with 5% coefficient of variation, which is within the range of uncertainty usually considered. The experiments showed that torsion and ejection fraction were the most affected quantities by the uncertain inputs. The main responsible inputs to their variability were the wall thickness, the magnitude of the active stress and the angles related to the longitudinal fiber direction.

Different tests were performed to incorporate uncertainty in wall thickness, where experiment 1 and experiment 2 obtained similar results, showing that variations in the mean values of wall thickness do not cause a different behaviour in the analyses when uncertain wall thickness is considered in a homogeneous manner. However, when wall thickness is varied only in the lateral region of the ventricle as in experiment 3, torsion and fiber strain become more sensitive to this input, whereas end systolic pressure, ejection fraction and dP/dt_{max} become less sensitive to wall thickness and more sensitive to active

stress. Experiment 4 considered a large variability in wall thickness and it was observed that uncertainties from this input dominates the impact on all quantities of interest. This case reflects a variability caused by errors during the segmentation process, as presented in the work of Suinesiaputra et al. (2015). The propagation of segmentation errors used to reconstruct LV geometry can substantially affect the models predictions.

It was verified that parameters of the circulatory model have a small contribution in the variability of the observed quantities, including the time series quantities. Therefore, these parameters could be fixed in a value within their range of uncertainty. However, a larger variability for these inputs is yet to be tested. In the near future, we plan to perform new experiments, including larger uncertainties on different parameters to study how this would affect forward uncertainty quantification and sensitivity analysis.

An interesting result was presented in the time-averaged Sobol sensitivity indices, where the magnitude of the active stress has shown high impact in the pressure and volume time series. Consequently, the quantities computed from the PV-loop, such as ejection fraction, were very sensitive to uncertainties in active stress. T_{ref} changes the level of contractility, which in turn affects the pressure and volume of the LV cavity, as reported by Kallhovd et al. (2019).

Other works (Rodríguez-Cantano et al., 2019; Campos et al., 2019) have also used the Laplace-Dirichlet algorithm to assign the fiber orientation in LV geometries and reported that uncertainty in these angles did not impact significantly quantities of interest extracted at the end of the passive filling phase. However, the present study which considered the full cardiac cycle showed that LV torsion and fiber strain extracted at early ejection are very sensitive to the angles related to fiber direction, which is expected due to the LV contraction caused by the active stress applied in the fiber direction.

As reported by Choi et al. (2010) and in the last chapter, it was observed that wall thickness has the largest impact on fiber stress. The analysis of uncertainty propagation for fiber stress and strain time series showed that these quantities presented significant variability at the ejection phase. The deviation are larger in the medial and apical region than basal region. The sensitivity analysis showed that these time series are more sensitive to wall thickness and the magnitude of active stress.

Finally, the present study has some limitations in the sense that long and short axis lengths were not considered, and as reported by Barbarotta and Bovendeerd (2019)

the LV size can influence strain. Furthermore, only models of the mechanical function were considered, and the further investigation of strongly coupled electromechanical models (Hurtado et al., 2017), where tissue will locally contract at different times and the electrical activity can impact in the active stress, can further advance this study.

In summary, the present study showed that the geometrical reconstruction and fiber orientation assignment are more important than parameters of the constitutive and circulatory models, highlighting the need of an accurate process in the generation of geometrical models. Uncertainties in these inputs have significant impact in important quantities such as ejection fraction and fiber stress. The magnitude of the active stress is also very important and can cause significant variations in the ventricular function during the cardiac cycle. Furthermore, the presented analyses can guide other works in the construction of simplified models with lower computational cost, where geometrical aspects should be prioritized.

6 Conclusion

The present work focused on uncertainty quantification and sensitivity analysis for cardiac mechanics simulations. Analyses were performed in simplified and personalized geometries of the left ventricle to verify the uncertainty propagation in model predictions and the influence of each uncertain input in the clinical quantities studied. Additionally, an Augmented Lagrangian formulation combined with an algebraic multigrid preconditioner for the numerical solution of cardiac mechanics problems was studied.

Initially, analyses for cardiac mechanics simulations reproducing the left ventricle passive filling phase were performed. LV wall thickness, fiber orientation and constitutive parameters were considered as uncertain model inputs, where a parametrization of the left ventricle geometry was used to consider uncertainties in regional wall thickness. The results showed that uncertainties in wall thickness impact the chosen quantities of interest in the same proportion of uncertain stiffness or even more in some cases. Particularly, the experiments showed that stress is highly influenced due to uncertainties in wall thickness, which is a quantity difficult to be measured and generally it is computed through computational models. The experiments also showed that biological variability in healthy patients is sufficient to impact the quantities of interest and this impact increases significantly when pathological variability is considered.

Next, analyses were performed considering the left ventricle function during the entire cardiac cycle, which allowed the assessment of important quantities used in clinical applications. The input parameters considered were the regional wall thickness, fiber orientation, constitutive material properties, active stress and circulatory model parameters used to prescribe pressure loading. The results showed that torsion and ejection fraction are the quantities most impacted by the uncertain inputs and all quantities are very sensitive to the active stress magnitude as well as by wall thickness. When wall thickness varies only in the LV lateral region, the outputs become less sensitive to this uncertain input, except for torsion which becomes more sensitive to wall thickness. Furthermore, the volume and pressure over time were very sensitive to the magnitude of the active stress and wall thickness. Therefore, the results have shown that patient-specific simulations requires accuracy in the processes of geometry reconstruction, fiber

orientation assignment and the choice of active stress magnitude.

In addition, numerical improvements of the cardiac mechanics solver were also presented. The proposed Augmented Lagrangian formulation combined with the AMG preconditioner brought more efficiency for the Krylov iterative solver in the simulations. We also showed that the ALG formulation allows to control volumetric changes in *a priori* fashion, which is not possible with other standard formulations, and how this can affect enforcing incompressibility, error and performance. Therefore, ALG can be used to improve performance of iterative solvers by reducing κ as well as for tuning the simulations to achieve a specified volume change.

6.1 Future works

A possible extension of the present work is to consider one random variable wall thickness value for each AHA segment, or representing the wall thickness as stochastic fields, and then quantify uncertainties in a more general case. The same approach could also be applied to consider spatial variability for the material parameters and fiber orientation. The resulting analysis will include a large number of uncertain input parameters, which will complicate the quantification and understanding of the role of individual contributions, but could give a more detailed assessment on the total uncertainty in the model output.

This type of analysis could be extended to consider strongly coupled electro-mechanics simulations, where other uncertain inputs would have to be considered, such as those from models of the electrical and mechanical behavior at the cellular level and the model for the electrical wave propagation in the tissue. Analyses using more realistic geometries considering both ventricles and also both atria could be another step of study towards the translation of these simulations to clinical applications.

REFERENCES

- RCP Kerckhoffs, PHM Bovendeerd, JCS Kotte, FW Prinzen, K Smits, and T Arts. Homogeneity of cardiac contraction despite physiological asynchrony of depolarization: a model study. *Annals of Biomedical Engineering*, 31(5):536–547, 2003.
- Wikimedia Commons. File:diagram of the human heart.svg — wikimedia commons, the free media repository, 2019. URL https://commons.wikimedia.org/w/index.php?title=File:Diagram_of_the_human_heart.svg&oldid=355529738. [Online; accessed 26-September-2019].
- Richard Klabunde. *Cardiovascular physiology concepts*. Lippincott Williams & Wilkins, 2011.
- Wikimedia Commons. File:conduction system en (cardionetworks ecgpedia).png — wikimedia commons, the free media repository, 2018. URL [https://commons.wikimedia.org/w/index.php?title=File:Conduction_system_en_\(CardioNetworks_ECGpedia\).png&oldid=315689305](https://commons.wikimedia.org/w/index.php?title=File:Conduction_system_en_(CardioNetworks_ECGpedia).png&oldid=315689305). [Online; accessed 27-September-2019].
- Avan Suinesiaputra, Brett R Cowan, Ahmed O Al-Agamy, Mustafa A Elattar, Nicholas Ayache, Ahmed S Fahmy, Ayman M Khalifa, Pau Medrano-Gracia, Marie-Pierre Jolly, Alan H Kadish, et al. A collaborative resource to build consensus for automated left ventricular segmentation of cardiac mr images. *Medical Image Analysis*, 18(1):50–62, 2014.
- Sander Land, Viatcheslav Gurev, Sander Arens, Christoph M. Augustin, Lukas Baron, Robert Blake, Chris Bradley, Sebastian Castro, Andrew Crozier, Marco Favino, Thomas E. Fastl, Thomas Fritz, Hao Gao, Alessio Gizzi, Boyce E. Griffith, Daniel E. Hurtado, Rolf Krause, Xiaoyu Luo, Martyn P. Nash, Simone Pezzuto, Gernot Plank,

- Simone Rossi, Daniel Ruprecht, Gunnar Seemann, Nicolas P. Smith, Joakim Sundnes, J. Jeremy Rice, Natalia Trayanova, Dafang Wang, Zhinuo Jenny Wang, and Steven A. Niederer. Verification of cardiac mechanics software: benchmark problems and solutions for testing active and passive material behaviour. *Proceedings of the Royal Society of London A: Mathematical, Physical and Engineering Sciences*, 471(2184), 2015. ISSN 1364-5021. doi: 10.1098/rspa.2015.0641.
- Sheikh Mohammad Shavik, Samuel T Wall, Joakim Sundnes, Daniel Burkhoff, and Lik Chuan Lee. Organ-level validation of a cross-bridge cycling descriptor in a left ventricular finite element model: effects of ventricular loading on myocardial strains. *Physiological reports*, 5(21), 2017.
- Wenjia Bai, Wenzhe Shi, Antonio de Marvao, Timothy JW Dawes, Declan P O'Regan, Stuart A Cook, and Daniel Rueckert. A bi-ventricular cardiac atlas built from 1000+ high resolution mr images of healthy subjects and an analysis of shape and motion. *Medical Image Analysis*, 26(1):133–145, 2015.
- World Health Organization. Cardiovascular disease, September 2019. URL http://origin.who.int/cardiovascular_diseases/en.
- Emelia J. Benjamin, Paul Muntner, Alvaro Alonso, Marcio S. Bittencourt, Clifton W. Callaway, April P. Carson, Alanna M. Chamberlain, Alexander R. Chang, Susan Cheng, Sandeep R. Das, Francesca N. Dellinger, Luc Djousse, Mitchell S.V. Elkind, Jane F. Ferguson, Myriam Fornage, Lori Chaffin Jordan, Sadiya S. Khan, Brett M. Kissela, Kristen L. Knutson, Tak W. Kwan, Daniel T. Lackland, Tené T. Lewis, Judith H. Lichtman, Chris T. Longenecker, Matthew Shane Loop, Pamela L. Lutsey, Seth S. Martin, Kunihiro Matsushita, Andrew E. Moran, Michael E. Mussolino, Martin O'Flaherty, Ambarish Pandey, Amanda M. Perak, Wayne D. Rosamond, Gregory A. Roth, Uchechukwu K.A. Sampson, Gary M. Satou, Emily B. Schroeder, Svati H. Shah, Nicole L. Spartano, Andrew Stokes, David L. Tirschwell, Connie W. Tsao, Mintu P. Turakhia, Lisa B. VanWagner, John T. Wilkins, Sally S. Wong, Salim S. Virani, and null null. Heart disease and stroke statistics—2019 update: A report from the american heart association. *Circulation*, 139(10):e56–e528, 2019. doi: 10.1161/CIR.0000000000000659.

- Hermenegild J Arevalo, Fijoy Vadakkumpadan, Eliseo Guallar, Alexander Jebb, Peter Malamas, Katherine C Wu, and Natalia A Trayanova. Arrhythmia risk stratification of patients after myocardial infarction using personalized heart models. *Nature Communications*, 7:11437, 2016.
- G. F. Tomaselli and E. Marbán. Electrophysiological remodeling in hypertrophy and heart failure. *Cardiovascular Research*, 42(2):270–283, 1999.
- Harald Osnes and Joakim Sundnes. Uncertainty analysis of ventricular mechanics using the probabilistic collocation method. *IEEE Transactions on Biomedical Engineering*, 59(8):2171–2179, 2012.
- Daniel E Hurtado, Sebastián Castro, and Pedro Madrid. Uncertainty quantification of two models of cardiac electromechanics. *International Journal for Numerical Methods in Biomedical Engineering*, 2017.
- Daniel D Streeter, Henry M Spotnitz, Dali P Patel, John Ross, and Edmund H Sonnenblick. Fiber orientation in the canine left ventricle during diastole and systole. *Circulation Research*, 24(3):339–347, 1969.
- Ian J LeGrice, BH Smaill, LZ Chai, SG Edgar, JB Gavin, and Peter J Hunter. Laminar structure of the heart: ventricular myocyte arrangement and connective tissue architecture in the dog. *American Journal of Physiology-Heart and Circulatory Physiology*, 269(2):H571–H582, 1995.
- J. Sundnes, G. T. Lines, X. Cai, B. F. Nielsen, K. A. Mardal, and A. Tveito. *Computing the electrical activity in the heart*. Springer Science & Business Media, 2007.
- E. J. Vigmond, R. Weber dos Santos, A. J. Prassl, M. Deo, and G. Plank. Solvers for the cardiac bidomain equations. *Progress in Biophysics and Molecular Biology*, 96(1):3–18, 2008.
- B. L. Oliveira, B. M. Rocha, L. P. S. Barra, E. M. Toledo, J. Sundnes, and R. Weber dos Santos. Effects of deformation on transmural dispersion of repolarization using in silico models of human left ventricular wedge. *International Journal for Numerical Methods in Biomedical Engineering*, 2013.

- Piero Colli Franzone, Luca F. Pavarino, and Simone Scacchi. Bioelectrical effects of mechanical feedbacks in a strongly coupled cardiac electro-mechanical model. *Math. Models Methods Appl. Sci.*, 26(27), 2016.
- Azzam Hazim, Youssef Belhamadia, and Stevan Dujljevic. Control of cardiac alternans in an electromechanical model of cardiac tissue. *Computers in Biology and Medicine*, 63:108–117, 2015.
- Douglas L. Mann and M. R. Bristow. Mechanisms and models in heart failure: The biomechanical model and beyond. *Circulation*, 111(21), 2005.
- Lik Chuan Lee, Joakim Sundnes, Martin Genet, Jonathan F. Wenk, and Samuel T. Wall. An integrated electromechanical-growth heart model for simulating cardiac therapies. *Biomechanics and Modeling in Mechanobiology*, 15:791–803, 2016.
- Sander Land, Steven A Niederer, and Nicolas P Smith. Efficient computational methods for strongly coupled cardiac electromechanics. *IEEE Transactions on Biomedical Engineering*, 59(5):1219–1228, 2012.
- J Sundnes, S Wall, H Osnes, T Thorvaldsen, and AD McCulloch. Improved discretisation and linearisation of active tension in strongly coupled cardiac electro-mechanics simulations. *Computer Methods in Biomechanics and Biomedical Engineering*, 17(6): 604–615, 2014.
- Myrianthi Hadjicharalambous, Jack Lee, Nicolas P. Smith, and David A. Nordsletten. A displacement-based finite element formulation for incompressible and nearly-incompressible cardiac mechanics. *Computer Methods in Applied Mechanics and Engineering*, 274:213 – 236, 2014. ISSN 0045-7825. doi: <http://dx.doi.org/10.1016/j.cma.2014.02.009>.
- Lik Chuan Lee, Samuel T Wall, Martin Genet, Andy Hinson, and Julius M Guccione. Bioinjection treatment: Effects of post-injection residual stress on left ventricular wall stress. *Journal of Biomechanics*, 47(12):3115–3119, 2014.
- N. A. Trayanova and R. Winslow. Whole-heart modeling: Applications to cardiac electrophysiology and electromechanics. *Circulation Research*, 108(1), 2011.

- Rafael Sachetto Oliveira, Sergio Alonso, Fernando Otaviano Campos, Bernardo Martins Rocha, João Filipe Fernandes, Titus Kuehne, and Rodrigo Weber dos Santos. Ectopic beats arise from micro-reentries near infarct regions in simulations of a patient-specific heart model. *Scientific Reports*, 8(1):16392, 2018.
- Gabriel Balaban, Henrik Finsberg, Simon Funke, Trine F. Håland, Einar Hopp, Joakim Sundnes, Samuel Wall, and Marie E. Rognes. In vivo estimation of elastic heterogeneity in an infarcted human heart. *Biomechanics and Modeling in Mechanobiology*, 17(5): 1317–1329, Oct 2018. ISSN 1617-7940. doi: 10.1007/s10237-018-1028-5.
- A Quaglino, S Pezzuto, PS Koutsourelakis, A Auricchio, and R Krause. Fast uncertainty quantification of activation sequences in patient-specific cardiac electrophysiology meeting clinical time constraints. *International Journal for Numerical Methods in Biomedical Engineering*, page e2985, 2018.
- Rocío Rodríguez-Cantano, Joakim Sundnes, and Marie E Rognes. Uncertainty in cardiac myofiber orientation and stiffnesses dominate the variability of left ventricle deformation response. *International Journal for Numerical Methods in Engineering*, 79(11):1–20, 2019.
- Wouter Huberts, WP Donders, Tammo Delhaas, and FN Vosse. Applicability of the polynomial chaos expansion method for personalization of a cardiovascular pulse wave propagation model. *International Journal for Numerical Methods in Biomedical Engineering*, 30(12):1679–1704, 2014.
- Gerhard A Holzapfel, Thomas C Gasser, and Ray W Ogden. A new constitutive framework for arterial wall mechanics and a comparative study of material models. *Journal of Elasticity and the Physical Science of Solids*, 61(1-3):1–48, 2000.
- J Biehler and WA Wall. The impact of personalized probabilistic wall thickness models on peak wall stress in abdominal aortic aneurysms. *International journal for numerical methods in biomedical engineering*, 34(2):e2922, 2018.
- Bernardo Martins Rocha. *Modelagem da atividade eletromecânica do coração e os efeitos da deformação na repolarização*. PhD thesis, Laboratório Nacional de Computação Científica, 2014.

- JPF Rodrigues, TR Schmal, Johnny Moreira Gomes, BM Rocha, and RW dos Santos. Patient-specific left ventricle mesh generation using the bull's eye of the wall thickness measurements from medical images. In *VI Latin American Congress on Biomedical Engineering CLAIB 2014, Paraná, Argentina 29, 30 & 31 October 2014*, pages 393–396. Springer, 2015.
- Gerhard A. Holzapfel. *Nonlinear Solid Mechanics: A Continuum Approach for Engineering*. Wiley, 2000.
- Richard D. Wood Javier Bonet. *Nonlinear Continuum Mechanics for Finite Element Analysis*. Cambridge, New York, second edition, 2008.
- Kevin D Costa, Peter J Hunter, JS Wayne, LK Waldman, JM Guccione, and Andrew D McCulloch. A three-dimensional finite element method for large elastic deformations of ventricular myocardium: II—prolate spheroidal coordinates. *Journal of Biomechanical Engineering*, 118(4):464–472, 1996.
- JD Humphrey and FCP Yin. On constitutive relations and finite deformations of passive cardiac tissue: I. a pseudostrain-energy function. *Journal of Biomechanical Engineering*, 109(4):298–304, 1987.
- Julius M Guccione, Andrew D McCulloch, LK Waldman, et al. Passive material properties of intact ventricular myocardium determined from a cylindrical model. *J Biomech Eng*, 113(1):42–55, 1991.
- Kevin D Costa, Jeffrey W Holmes, and Andrew D McCulloch. Modelling cardiac mechanical properties in three dimensions. *Philosophical transactions of the Royal Society of London. Series A: Mathematical, Physical and Engineering sciences*, 359(1783):1233–1250, 2001.
- Gerhard A Holzapfel and Ray W Ogden. Constitutive modelling of passive myocardium: a structurally based framework for material characterization. *Philosophical Transactions of the Royal Society A: Mathematical, Physical and Engineering Sciences*, 367(1902): 3445–3475, 2009.
- Samuel T Wall, Joseph C Walker, Kevin E Healy, Mark B Ratcliffe, and Julius M

- Guccione. Theoretical impact of the injection of material into the myocardium. *Circulation*, 114(24):2627–2635, 2006.
- V Gurev, J Constantino, JJ Rice, and NA Trayanova. Distribution of electromechanical delay in the heart: insights from a three-dimensional electromechanical model. *Biophysical Journal*, 99(3):745–754, 2010.
- HM Wang, H Gao, XY Luo, C Berry, BE Griffith, RW Ogden, and TJ Wang. Structure-based finite strain modelling of the human left ventricle in diastole. *International Journal for Numerical Methods in Biomedical Engineering*, 29(1):83–103, 2013.
- Jay D Humphrey. *Cardiovascular solid mechanics: cells, tissues, and organs*. Springer Science & Business Media, 2013.
- Manuel D Cerqueira, Neil J Weissman, Vasken Dilsizian, Alice K Jacobs, Sanjiv Kaul, Warren K Laskey, Dudley J Pennell, John A Rumberger, Thomas Ryan, Mario S Verani, et al. Standardized myocardial segmentation and nomenclature for tomographic imaging of the heart. *Circulation*, 105(4):539–542, 2002.
- Christophe Geuzaine and Jean-François Remacle. Gmsh: A 3-d finite element mesh generator with built-in pre-and post-processing facilities. *International Journal for Numerical Methods in Engineering*, 79(11):1309–1331, 2009.
- Jason D Bayer, Robert C Blake, Gernot Plank, and Natalia A Trayanova. A novel rule-based algorithm for assigning myocardial fiber orientation to computational heart models. *Annals of Biomedical Engineering*, 40(10):2243–2254, 2012.
- D. Ambrosi and S. Pezzuto. Active stress vs. active strain in mechanobiology: Constitutive issues. *Journal of Elasticity*, 107(2):199–212, Apr 2012. ISSN 1573-2681. doi: 10.1007/s10659-011-9351-4.
- John Jeremy Rice, Fei Wang, Donald M Bers, and Pieter P De Tombe. Approximate model of cooperative activation and crossbridge cycling in cardiac muscle using ordinary differential equations. *Biophysical Journal*, 95(5):2368–2390, 2008.
- BJ van Nierop. Coupling a finite element model of left ventricular mechanics in a closed loop lumped parameter model of circulatory hemodynamics. 2007. URL <http://www.mate.tue.nl/mate/pdfs/7975.pdf>.

- Mark H Holmes. *Introduction to numerical methods in differential equations*. Springer: Berlin, Germany, 2011.
- Roy CP Kerckhoffs, Maxwell L Neal, Quan Gu, James B Bassingthwaite, Jeff H Omens, and Andrew D McCulloch. Coupling of a 3d finite element model of cardiac ventricular mechanics to lumped systems models of the systemic and pulmonic circulation. *Annals of Biomedical Engineering*, 35(1):1–18, 2007.
- Rasmus Tamstorf, Toby Jones, and Stephen F. McCormick. Smoothed aggregation multigrid for cloth simulation. *ACM Transactions on Graphics*, 34(6):Article 245, 2015.
- K. Stüben. A review of algebraic multigrid. *Journal of Computational and Applied Mathematics*, 2001.
- A. H. Baker, Tz. V. Kolev, and U. M. Yang. Improving algebraic multigrid interpolation operators for linear elasticity problems. *Numerical Linear Algebra with Applications*, 17:495–517, 2009.
- Rodrigo Weber dos Santos, Gernot Plank, Steffen Bauer, and Edward J Vigmond. Parallel multigrid preconditioner for the cardiac bidomain model. *IEEE Transactions on Biomedical Engineering*, 51(11):1960–1968, 2004.
- G. Plank, M. Liebmann, R. Weber dos Santos, E. J. Vigmond, and G. Haase. Algebraic multigrid preconditioner for the cardiac bidomain model. *IEEE Transactions on Biomedical Engineering*, 54(4):585 – 596, 2007.
- Allison H Baker, Axel Klawonn, Tzanio Kolev, Martin Lanser, Oliver Rheinbach, and Ulrike Meier Yang. Scalability of classical algebraic multigrid for elasticity to half a million parallel tasks. In *Software for Exascale Computing-SPPEXA 2013-2015*, pages 113–140. Springer, 2016.
- Franco Brezzi and Michel Fortin. *Mixed and Hybrid Finite Element Methods*. Springer Series in Computational Mathematics, 1991.
- Thomas Elguedj, Yuri Bazilevs, Victor M. Calo, and Thomas J.R. Hughes. B-bar and F-bar projection methods for nearly incompressible linear and non-linear elasticity and plasticity using higher-order NURBS elements. *Computer Methods in Applied Mechanics and Engineering*, 197:33–40, 2008.

- J. C. Simo and R. L. Taylor. Quasi-incompressible finite elasticity in principal stretches. continuum basis and numerical algorithms. *Computer Methods in Applied Mechanics and Engineering*, 85:273–310, 1991.
- J. Weiss, B. Maker, and S. Govindjee. Finite element implementation of incompressible, transversely isotropic hyperelasticity. *Computer Methods in Applied Mechanics and Engineering*, 135:107–128, 1996.
- Thomas JR Hughes. *The finite element method: linear static and dynamic finite element analysis*. Courier Corporation, 2012.
- J. C. Simo, R. L. Taylor, and K. S. Pister. Variational and projection methods for the volume constraint in finite deformation elasto-plasticity. *Computer Methods in Applied Mechanics and Engineering*, 51:177–208, 1985.
- T. C. Gasser, R. W. Ogden, and G. A. Holzapfel. Hyperelastic modelling of arterial layers with distributed collagen fibre orientations. *J. R. Soc. Interface*, 3:15–35, 2006.
- R. Glowinski and P. Le Tallec. Numerical solution of problems in incompressible finite elasticity by augmented lagrangian methods. i. two-dimensional and axisymmetric problems. *SIAM Journal on Applied Mathematics*, 42:400–429, 1982.
- R. Glowinski and P. Le Tallec. Numerical solution of problems in incompressible finite elasticity by augmented lagrangian methods. ii. three-dimensional problems. *SIAM Journal on Applied Mathematics*, 44:710–733, 1984.
- Roland Glowinski and Patrick Le Tallec. *Augmented Lagrangian and operator-splitting methods in nonlinear mechanics*. SIAM, 1989.
- Y. Saad. *Iterative methods for sparse linear systems*. SIAM (Society for Industrial and Applied Mathematics), 2003.
- W. L. Briggs, V. E. Henson, and S. F. McCormick. *A Multigrid Tutorial*. Society for Industrial and Applied Mathematics, second edition, 2000.
- Christoph M Augustin, Aurel Neic, Manfred Liebmann, Anton J Prassl, Steven A Niederer, Gundolf Haase, and Gernot Plank. Anatomically accurate high resolution modeling of human whole heart electromechanics: a strongly scalable algebraic

- multigrid solver method for nonlinear deformation. *Journal of Computational Physics*, 305:622–646, 2016.
- V.E. Henson and U.M. Yang. BoomerAMG: A parallel algebraic multigrid solver and preconditioner. *Applied Numerical Mathematics*, 41:155–177, 2002.
- Jonathan Feinberg and Hans Petter Langtangen. Chaospy: An open source tool for designing methods of uncertainty quantification. *Journal of Computational Science*, 11:46 – 57, 2015. ISSN 1877-7503. doi: <http://dx.doi.org/10.1016/j.jocs.2015.08.008>.
- Jonathan Feinberg. Some improvements and applications of non-intrusive polynomial chaos expansions. 2015.
- George Fishman. *Monte Carlo: concepts, algorithms, and applications*. Springer Science & Business Media, 2013.
- Ali H Nayfeh. *Perturbation methods*. John Wiley & Sons, 2008.
- Wing Kam Liu, Ted Belytschko, and A Mani. Probabilistic finite elements for nonlinear structural dynamics. *Computer Methods in Applied Mechanics and Engineering*, 56(1): 61–81, 1986.
- XG Hua, YQ Ni, ZQ Chen, and JM Ko. An improved perturbation method for stochastic finite element model updating. *International Journal for Numerical Methods in Engineering*, 73(13):1845–1864, 2008.
- Dongbin Xiu and George Em Karniadakis. The wiener-asky polynomial chaos for stochastic differential equations. *SIAM journal on scientific computing*, 24(2):619–644, 2002.
- Dongbin Xiu. *Numerical methods for stochastic computations: a spectral method approach*. Princeton university press, 2010. ISBN 9780691142128.
- Heng Li and Dongxiao Zhang. Probabilistic collocation method for flow in porous media: Comparisons with other stochastic methods. *Water Resources Research*, 43(9), 2007.
- Serhat Hosder, Robert Walters, and Michael Balch. Efficient sampling for non-intrusive polynomial chaos applications with multiple uncertain input variables. In

- 48th AIAA/ASME/ASCE/AHS/ASC Structures, Structural Dynamics, and Materials Conference*, page 1939, 2007.
- Ilya M Sobol. Global sensitivity indices for nonlinear mathematical models and their monte carlo estimates. *Mathematics and Computers in Simulation*, 55(1-3):271–280, 2001.
- Vinzenz Gregor Eck, Wouter Paulus Donders, Jacob Sturdy, Jonathan Feinberg, Tammo Delhaas, Leif Rune Hellevik, and Wouter Huberts. A guide to uncertainty quantification and sensitivity analysis for cardiovascular applications. *International Journal for Numerical Methods in Biomedical Engineering*, 32(8), 2016.
- VG Eck, J Sturdy, and LR Hellevik. Effects of arterial wall models and measurement uncertainties on cardiovascular model predictions. *Journal of biomechanics*, 50:188–194, 2017.
- Pierric Kersaudy, Bruno Sudret, Nadège Varsier, Odile Picon, and Joe Wiart. A new surrogate modeling technique combining kriging and polynomial chaos expansions—application to uncertainty analysis in computational dosimetry. *Journal of Computational Physics*, 286:103–117, 2015.
- Hon Fai Choi, Jan D’hooge, FE Rademakers, and Piet Claus. Influence of left-ventricular shape on passive filling properties and end-diastolic fiber stress and strain. *Journal of Biomechanics*, 43(9):1745–1753, 2010.
- Luca Barbarotta and Peter Bovendeerd. A computational approach on sensitivity of left ventricular wall strains to geometry. In *International Conference on Functional Imaging and Modeling of the Heart*, pages 240–248. Springer, 2019.
- Paolo Di Achille, Ahmed Harouni, Svyatoslav Khamzin, Olga Solovyova, John Jeremy Rice, and Viatcheslav Gurev. Gaussian process regressions for inverse problems and parameter searches in models of ventricular mechanics. *Frontiers in physiology*, 9:1002, 2018.
- S Kallhovd, J Sundnes, and ST Wall. Sensitivity of stress and strain calculations to passive material parameters in cardiac mechanical models using unloaded geometries. *Computer methods in biomechanics and biomedical engineering*, 22(6):664–675, 2019.

A. Crozier, C. M. Augustin, A. Neic, A. J. Prassl, M. Holler, T. E. Fastl, A. Hennemuth, K. Bredies, T. Kuehne, M. J. Bishop, S. A. Niederer, and G. Plank. Image-based personalization of cardiac anatomy for coupled electromechanical modeling. *Annals of Biomedical Engineering*, 44(1):58–70, Jan 2016. ISSN 1573-9686. doi: 10.1007/s10439-015-1474-5.

Frits W Prinzen, Emile C Cheriex, Tammo Delhaas, Matthijs FM van Oosterhout, Theo Arts, Hein JJ Wellens, and Robert S Reneman. Asymmetric thickness of the left ventricular wall resulting from asynchronous electric activation: a study in dogs with ventricular pacing and in patients with left bundle branch block. *American Heart Journal*, 130(5):1045–1053, 1995.

Matthijs FM Van Oosterhout, Frits W Prinzen, Theo Arts, Jan J Schreuder, Ward YR Vanagt, Jack PM Cleutjens, and Robert S Reneman. Asynchronous electrical activation induces asymmetrical hypertrophy of the left ventricular wall. *Circulation*, 98(6):588–595, 1998.

Kevin Vernooy, Xander AAM Verbeek, Maaïke Peschar, Harry JGM Crijns, Theo Arts, Richard NM Cornelussen, and Frits W Prinzen. Left bundle branch block induces ventricular remodelling and functional septal hypoperfusion. *European Heart Journal*, 26(1):91–98, 2004.

Joventino Oliveira Campos, Rodrigo Weber dos Santos, Joakim Sundnes, and Bernardo Martins Rocha. Preconditioned augmented lagrangian formulation for nearly incompressible cardiac mechanics. *International Journal for Numerical Methods in Biomedical Engineering*, 34(4):e2948, 2018. doi: 10.1002/cnm.2948. e2948 cnm.2948.

Julius M. Guccione, Kevin D. Costa, and Andrew D. McCulloch. Finite element stress analysis of left ventricular mechanics in the beating dog heart. *Journal of Biomechanics*, 28(10):1167 – 1177, 1995. ISSN 0021-9290. doi: [http://dx.doi.org/10.1016/0021-9290\(94\)00174-3](http://dx.doi.org/10.1016/0021-9290(94)00174-3).

FC Yin, CC Chan, and Robert M Judd. Compressibility of perfused passive myocardium. *American Journal of Physiology-Heart and Circulatory Physiology*, 271(5):H1864–H1870, 1996.

- Joventino Olivera Campos, Joakim Sundnes, Rodrigo Weber dos Santos, and Bernardo Martins Rocha. Effects of left ventricle wall thickness uncertainties on cardiac mechanics. *Biomechanics and modeling in mechanobiology*, 2019.
- Hao Gao, Liuyang Feng, Nan Qi, Colin Berry, Boyce E Griffith, and Xiaoyu Luo. A coupled mitral valve—left ventricle model with fluid–structure interaction. *Medical Engineering & Physics*, 47:128–136, 2017.
- Otto A. Smiseth and John M. Aalen. Mechanism of harm from left bundle branch block. *Trends in Cardiovascular Medicine*, 29(6):335 – 342, 2019. ISSN 1050-1738. doi: <https://doi.org/10.1016/j.tcm.2018.10.012>.
- Jonas Biehler, Michael W. Gee, and Wolfgang A. Wall. Towards efficient uncertainty quantification in complex and large-scale biomechanical problems based on a bayesian multi-fidelity scheme. *Biomechanics and Modeling in Mechanobiology*, 14(3):489–513, Jun 2015. ISSN 1617-7940. doi: 10.1007/s10237-014-0618-0.
- Avan Suinesiaputra, David A Bluemke, Brett R Cowan, Matthias G Friedrich, Christopher M Kramer, Raymond Kwong, Sven Plein, Jeanette Schulz-Menger, Jos JM Westenberg, Alistair A Young, et al. Quantification of lv function and mass by cardiovascular magnetic resonance: multi-center variability and consensus contours. *Journal of Cardiovascular Magnetic Resonance*, 17(1):63, 2015.